

12. SITE 1241¹

Shipboard Scientific Party²

INTRODUCTION

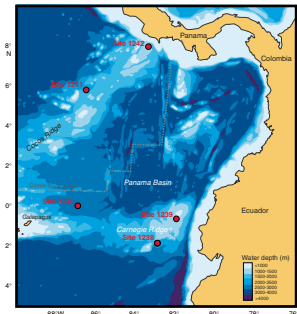
Site 1241 (proposed Site COC-2A) is located at 5°50.570'N, 86°26.676'W on a gently sloping sediment-covered ramp on the north flank of Cocos Ridge (Fig. F1) at 2027 m water depth in the Guatemala Basin. Some small bathymetric highs that rise a few hundred meters above the ramp probably represent volcanic outliers from the main edifice of Cocos Ridge (Fig. F2). The crust underlying the site was probably formed at the Galapagos hotspot, roughly coeval with the formation of seafloor crust ~11–13 m.y. ago at the Cocos-Nazca Rise (Hey et al., 1977) (Fig. F3).

A seismic profile at Site 1241 (Fig. F4) documents pelagic drape 400–500 m thick. To the south, the thinning of the sediment cover on Cocos Ridge along with bathymetric evidence for fossil channels indicates that some downslope transport of sediment has occurred. Dominant sediments in the region are foraminifer-bearing nannofossil ooze, lithifying to chalk at depth, and occasional ash layers that may record the history of volcanism in Central America (Ledbetter, 1985).

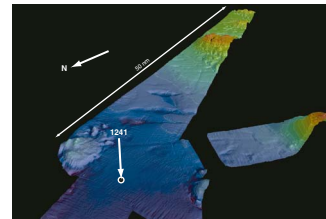
At its present location, Site 1241 (Fig. F5) is under the warm and relatively low salinity waters of the Panama Basin (Levitus and Boyer, 1994). Nutrients at the sea surface are low, and biological productivity is substantially lower than at the equator (Fig. F6) in spite of an anomalously shallow pycnocline (Ocean Climate Laboratory, 1999). In its recent history, the site is well positioned to monitor the location of the Intertropical Convergence Zone in the eastern Pacific.

A tectonic backtrack path on the Cocos plate (Pisias et al., 1995) moves Site 1241 southward and slightly to the west relative to South America (see Fig. F6, p. 80, in the “Leg 202 Summary” chapter). The site was probably located close to the equator and probably at shallower depths during the late Miocene. Site 1241 is expected to provide a record of surface water salinity reduction that occurred in response to

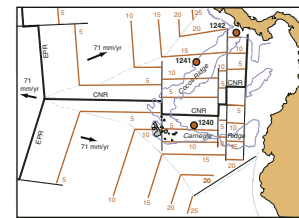
F1. Sites 1238–1242 and regional bathymetry, p. 22.



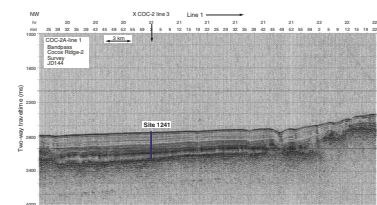
F2. High-resolution swath bathymetry, p. 23.



F3. Primary tectonic features of the Panama Basin, p. 24.



F4. Seismic profile at Site 1241, p. 25.



¹Examples of how to reference the whole or part of this volume.

²Shipboard Scientific Party addresses.

the closure of the Isthmus of Panama during late Miocene time (Haug et al., 2001), along with a record of volcanism in Central America based on the accumulation rates of ash (Sigurdsson et al., 2000).

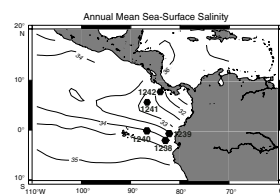
Plate tectonic backtrack locations can be used to predict general features of oceanographic change at Site 1241 under the assumptions that overall conditions in the region remain constant and that the only change in the system is drift of the site location relative to this fixed oceanographic background (Fig. F8). In this analysis we ignore changes in the position of the continental margin through time, which may be significant in the region of northern South America and the Central American Isthmus. Sampling of modern oceanographic atlas values at the paleosite locations suggest that from 10 to 11 m.y. ago, sea-surface temperatures at Site 1241 would have been significantly ($\sim 3^{\circ}\text{C}$) cooler and saltier (by one unit) than today because, at that time, the site was within the equatorial upwelling system and the South Equatorial Current. The pycnocline depth would have been much shallower in the past, as well, resulting in higher sea-surface nutrient concentrations and primary productivity prior to 6 Ma. In the absence of other regional changes in ocean circulation or tectonics, we would expect that biogenic sediment accumulation rates at Site 1241 would be relatively high prior to 6 Ma. Significant deviations from these general trends, if detected in the sediment cores, would imply changes in regional oceanographic or climatic conditions, or errors in the tectonic backtrack or age models.

On shorter timescales within the late Neogene, Site 1241 is likely to record oscillations of ice-age climate in changing sea-surface salinity and pycnocline depth, which are both associated with the heavy rainfall under the intertropical convergence. Here, glacial-interglacial sea-surface temperatures are thought to be relatively stable, with changes of just 1°–2°C inferred from species abundances of radiolarians (Pisias and Mix, 1997) and foraminifers (Mix et al., 1999).

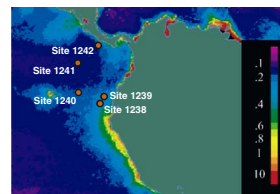
Deep waters of the Guatemala Basin (Fig. F7) currently derive from middepth waters of the North Pacific that enter through fracture zones in the East Pacific Rise (Tsuchiya and Talley, 1998). Waters of North Pacific origin are relatively depleted in oxygen and $\delta^{13}\text{C}$ and enriched in nutrients (Kroopnick, 1974). As a result of this oxygen-depleted source water, high amounts of organic rain on the Central American margin, and relatively little mixing with low-salinity surface waters, the region has one of the deepest and strongest oxygen minimum zones in the world and is thus an important site of denitrification and potential control of global nitrate budgets (Ganeshram et al., 1995). Carbonate dissolution is significant in deeper waters of the Guatemala Basin, and sites deeper than 3400 m (e.g., Ocean Drilling Program (ODP) Sites 844 and 845) have been below the carbonate compensation depth for the past 10 m.y. (Lyle et al., 1995). The relatively shallow depth of Site 1241 will facilitate study of changes in the upper reaches of the lysocline in Guatemala Basin and will complement our understanding of deepwater variability in the region. Based on the likely tectonic backtrack of the site to the south and to shallower water depths in the past, it is likely to monitor intermediate waters during late Miocene and early Pliocene time.

The primary objective at Site 1241 is to provide a continuous late Neogene sedimentary sequence to assess variability of upper-ocean processes, including the reorganization of equatorial Pacific surface circulation and the development of the Atlantic to Pacific salinity contrast,

F5. Upper-ocean salinity, p. 26.



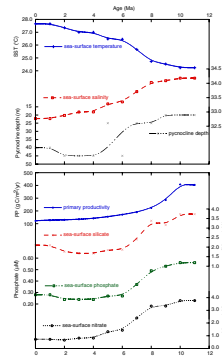
F6. Chlorophyll distributions in surface waters, p. 27.



F7. Meridional cross section of water masses, p. 28.



F8. Modern ocean properties at backtrack locations of Site 1241, p. 29.



both associated with the closure of the Isthmus of Panama and other late Neogene climate changes.

OPERATIONS

The 349-nmi transit to Site 1241 (proposed Site COC-2A) required 30.0 hr at an average speed of 11.6 kt. The 3.5-kHz precision depth recorder (PDR) was used as a final check of site characteristics by comparison to precruise survey data. The vessel was on site by 1545 hr on 20 May 2002.

Hole 1241A

The drill bit was deployed to a depth of 2033.4 meters below rig floor (mbrf), and Hole 1241A was initiated with the advanced piston corer (APC) at 2118 hr. The seafloor depth that was estimated by the amount of recovery of the first core was 2038.6 mbrf. This was 2.8 m shallower than the corrected PDR depth of 2041.4 mbrf. Piston coring penetrated to 314.2 meters below seafloor (mbsf) before it was necessary to switch to the extended core barrel (XCB) (Table T1). A total of 13 core barrels that could not be pulled with a force of 60 klb were drilled over starting with Core 22H. Piston coring in the hole was terminated when the last piston core (34H) did not achieve a full stroke of the corer.

The piston cores were oriented starting with Core 4H. Downhole temperature measurements were taken with the APC temperature (APCT) tool (Table T1). The nonmagnetic core barrel was deployed on even-numbered cores up to and including Core 22H. The APC cored 314.2 m and recovered 333.4 m (recovery = 106%).

XCB coring deepened the hole from 314.2 to 394.4 mbsf. The XCB cored 80.2 m and recovered 71.5 m, representing an average recovery of 89%. The APC/XCB cored interval was 394.4 m, and the average recovery in Hole 1241A was 103% (Table T1). The active heave compensator was online during XCB coring.

The bit was pulled free of the seafloor at 1920 hr on 22 May.

T1. Operations summary, Site 1241, p. 74.

Hole 1241B

The vessel was offset 20 m west of Hole 1241A. Prior to coring in Hole 1241B, a bottom water temperature measurement was obtained with the APCT tool with the bit positioned just above the seafloor. All APCT measurements combined indicated a low thermal gradient of ~2.7°C/100 m. To obtain a stratigraphic overlap with the first hole, the bit was placed at 2036.0 mbrf and Hole 1241B was initiated with the APC at 2115 hr. The seafloor depth derived from the recovery of the first core was 2037.1 mbrf. Piston coring and two 2-m drilled intervals (84.4–86.4 and 257.4–259.4 mbsf) deepened the hole to 259.4 mbsf. Seven fully stroked core barrels were drilled over in this hole (Cores 21H through 27H). The cores were not oriented because only one Tensor orientation tool remained operational, and it was preserved for use at the last site, where magnetic declination data were likely to be important. The nonmagnetic core barrel was deployed on odd-numbered cores up to and including Core 21H. The piston cored interval was 257.4 m with 258.43 m recovered (recovery = 101.2%).

Five XCB cores deepened the hole from 257.4 to 307.6 mbsf. The 87.4-m interval from 307.6 mbsf to the basement contact at 395.0 mbsf

was drilled in preparation for logging. The XCB cored 48.2 m and recovered 43.8 m (recovery = 91%). The total cored interval was 303.6 m with an average recovery of 100% (Table T1).

Logging

To prepare the hole for logging, it was flushed with 30 bbl of sepiolite mud. The hole was then displaced with 182 bbl of 8.9-lb/gal sepiolite mud, and the bit was placed at the logging depth of 97.45 mbsf. The triple combination (triple combo) tool string with the Lamont-Doherty Earth Observatory (LDEO) Multi-Sensor Spectral Gamma Ray Tool (MGT) on top was deployed first, followed by the Formation MicroScanner (FMS)-sonic tool string. One pass with the triple combo was conducted from total depth (395 mbsf) to the mudline, followed by one full pass from 395 mbsf to the bit with the MGT. Two subsequent passes with the FMS-sonic tool string also reached the bottom of the hole. The diameter of the hole ranged from 10.5 to 13.5 in, providing for good log quality.

Logging operations in Hole 1241B were completed by 1400 hr on 24 May. The bit was pulled free of the seafloor at 1510 hr on 24 May.

Hole 1241C

The vessel was offset 20 m west of Hole 1241B, and Hole 1241C was initiated with the APC at 1612 hr on 24 May with the bit positioned at 2039.0 mbrf. The seafloor depth calculated from the recovery of the mudline core was 2038.5 mbrf. Piston coring combined with drilling deepened the hole to 143.5 mbsf. Four intervals (6.0–26.0, 41–47.5, 104.5–112.0, and 131.0–134.0 mbsf), a total of 42.5 m, were drilled to maintain the proper overlap with the data from the previous two holes. No cores were oriented. The nonmagnetic core barrel was deployed on even-numbered cores. No core barrels were drilled over. The cored interval was 101.0 m, with 103.1 m recovered. Coring at Site 1241 yielded 810.1 m, representing an average recovery of 101% (Table T1).

Taking advantage of morning light, a supply vessel from Panama (VIVEROS) that had arrived on site during the early dark hours of 25 May came alongside the vessel. This vessel was contracted to bring out 150 boxes of D-tubes to replenish the nearly depleted stock. In addition to the much-needed D-tubes, the vessel also delivered 336 kg of fresh fruit, fresh vegetables, and cheese. The VIVEROS was secured to the port side of the *JOIDES Resolution* at 0630 hr and drifted in the lee of the larger vessel during unloading. One hr was needed to unload the supplies.

After the supply boat was released, the vessel was secured for transit and departed for the transit to the last site of the leg at 0800 hr on 25 May.

COMPOSITE SECTION

We built a meters composite depth (mcd) scale to Section 202-1241A-43X-2 (0.00–446.64 mcd) and a splice (as defined in “[Composite Section](#),” p. 4, in the “Explanatory Notes” chapter) that documents complete recovery for the upper 303.14 mcd. The splice ranges from the top of Core 202-1241B-1H to the bottom of Section 202-1241A-29H-7 (see Tables T2, T3). All APC cores except for 202-1241A-30H through 202-

[T2. Composite depth scale, p. 76.](#)

[T3. Splice tie points, p. 78.](#)

1241A-34H can be correlated to the splice at Site 1241. One XCB core, 202-1241B-28X, is also included in the splice. Cores 202-1241A-30H through 202-1241A-43X and 202-1241B-29X through 202-1241B-32X were appended to the mcd depth scale. The splice was not continued beyond the base of Core 202-1241A-29H, due to a lack of a representative signal from these cores.

Above about 70 mcd, the mcd scale and the splice are based on the stratigraphic correlation of Oregon State University Fast Track magnetic susceptibility (OSUS-MS) measurements and multisensor track magnetic susceptibility (MST-MS) measurements collected at 5-cm intervals (Fig. F9; Tables T4, T5, T6). Below 70 mcd, gamma ray attenuation (GRA) bulk density was used for correlation (Fig. F10). Tie points (Table T3) were then used to construct representative spliced records for MST-MS, GRA bulk density, and where available, natural gamma radiation (NGR) data, (Fig. F11) and for color reflectance (L^* , a^* , and b^*) data (Fig. F12).

We assumed that the uppermost sediment (the “mudline”) in Core 202-1241B-1H was the sediment/water interface. A mudline was also recovered in Cores 202-1241A-1H and 202-1241C-1H. Core 202-1241B-1H is the “anchor” in the composite depth scale. From this anchor we worked downhole, correlating records on a core-by-core basis.

A comparison of the mcd and mbsf depth scales (Fig. F13) shows that the mcd scale is on average 13% longer than the mbsf scale. Given that the growth factor of 1.13 in the splice was relatively constant and that the splice represents ~68% of the drilled section at Site 1241, we appended the XCB cores from Hole 1241A (Cores 202-1241A-35X through 43X) by assuming a 13% (1.25 m) offset from the core above.

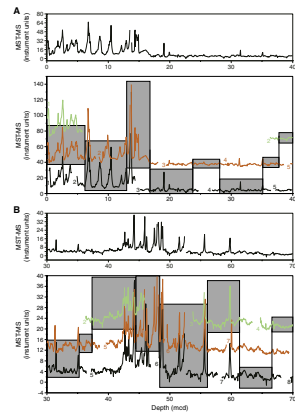
To facilitate the calculation of mass accumulation rates (MARs), we provide corrected meters composite depth (cmcd) in Table T2 and in Table T3 for depths within the splice.

LITHOSTRATIGRAPHY

A pelagic sediment sequence 447.06 mcd thick was recovered at Site 1241, spanning the interval from the late Miocene to the Holocene. The sediment at Site 1241 consists of various types of nannofossil ooze. A distinct interval of laminated diatom ooze is present near the base of the sequence between ~420 and 440 mcd. Biogenic constituents are predominantly nannofossils, but some intervals include significant amounts of diatoms, foraminifers, and/or siliciclastics, mainly clay. Interbedded minor lithologies include volcanic ash and lapilli layers. Physical properties reflect the mixture of a carbonate component, characterized by high bulk density, high reflectance, and low magnetic susceptibility and natural gamma radiation (NGR), with secondary constituents that dilute the carbonate signal. Organic pigment absorption features are detectable in reflectance spectra at 410 and 650 nm throughout the sediment.

Based on major lithologic components, textural characteristics, and physical properties, a single lithologic unit was defined and divided into three subunits. Subunit IA is composed primarily of clayey foraminifer-nannofossil ooze that exhibits cyclic variability in physical properties. Subunit IB contains nannofossil ooze with variable minor contributions from diatoms and foraminifers in a sequence whose overall homogeneity is clearly expressed in the physical properties. Subunit IC is composed primarily of clay diatom-bearing nannofossil ooze with

F9. MST-MS vs. mcd, p. 30.

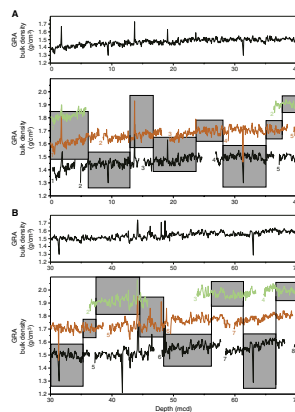


T4. OSUS-MS measurements, Hole 1241A, p. 79.

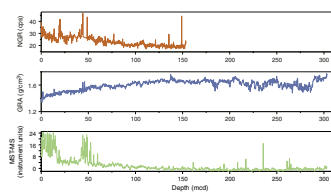
T5. OSUS-MS measurements, Hole 1241B, p. 80.

T6. OSUS-MS measurements, Hole 1241C, p. 81.

F10. GRA bulk density data vs. mcd, p. 37.



F11. Smoothed spliced records NGR, GRA density, and MST-MS, p. 44.



laminated diatom ooze near the base. Partially lithified nannofossil ooze underlies the laminated diatom ooze and sits atop basaltic sands and vesicular basalt fragments that are indicative of basement.

High diatom and total organic carbon (TOC) fluxes during the early part of the late Miocene are consistent with the tectonic path followed by Site 1241 on the Cocos plate, suggesting a decrease in biogenic production as the site gradually exited the active equatorial upwelling zone. Coeval low fluxes of nannofossils could be attributed to ecological variability and/or increased dissolution during the Miocene “carbonate crash” (Lyle et al., 1995). Subsequent increases in carbonate accumulation rates between ~7 and 5 Ma might be coincident with the “biogenic bloom” described in other regions of the tropical Indo-Pacific (Peterson et al., 1992; Farrell et al., 1995).

Seventy-two volcaniclastic horizons record both hotspot volcanic activity as well as volcanic eruptions in Central America. The decrease in brown volcanic glass and scoria toward recent times, paralleled by an increase in clear glass and pumice, is consistent with the eastward plate motion, which moves the site away from the Galapagos hotspot and toward the Central American volcanic arc. Increased volcanic activity between 0 and 2.5 Ma and 8 and 9 Ma agrees with high ash accumulation intervals previously described in the Caribbean.

Description of Lithologic Unit

Unit I

Intervals: Cores 202-1241A-1H through 43X; Cores 202-1241B-1H through 32X; and Cores 202-1241C-1H through 11H

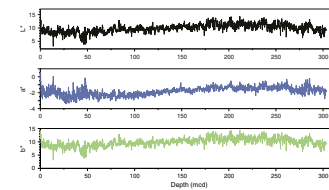
Depths: 0–447.06 mcd; Hole 1241A: 0–393.67 mbsf (0.30–447.06 mcd); Hole 1241B: 0–306.97 mbsf (0–345.26 mcd); and Hole 1241C: 0–143.90 mbsf (0.05–158.47 mcd)

Age: Pleistocene to late Miocene (0–11 Ma)

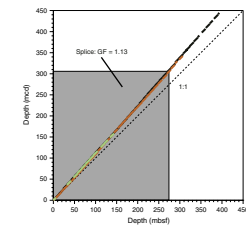
A single lithologic unit was defined and divided into three subunits on the basis of visual core description, smear slide analysis, color reflectance, magnetic susceptibility, NGR, moisture and density (MAD), and GRA bulk density measurements (Table T7; Fig. F14). Unit I is composed entirely of pelagic ooze dominated by nannofossils with variable enrichments of foraminifers, diatoms, and siliciclastics, primarily clay, whose relative distributions determine the presence of the three subunits (Fig. F15). Basaltic basement directly underlies the pelagic sequence.

Throughout Unit I at Site 1241, GRA bulk density and MAD bulk density are well correlated to each other ($r^2 = 0.89$) and porosity mirrors changes in bulk density ($r^2 = 0.9$) (Fig. F16). Grain density is controlled in part by carbonate content ($r^2 = 0.5$). Opaline silica content also affects the grain and bulk densities, as low values occurring between 350 and 440 mcd coincide with a distinct increase in diatom content (Fig. F16). The lightness parameter L^* is strongly controlled by carbonate content ($r^2 = 0.8$). A multiple regression between reflectance and carbonate improves this correlation only slightly ($r^2 = 0.9$). However, the relationship between reflectance and TOC is weak (i.e., $r^2 = \sim 0.4$ in a multiple linear regression). Reflectance measurements plot in the “yellow” domain of the a^*-b^* color plane (Fig. F17), although most of the data fall in the “green” quadrant (i.e., $a^* < 0$). Absorption features ascribed to chlorophyll-related pigments (i.e., chlorins) are detectable at

F12. Smoothed spliced records of L^* , a^* , and b^* , p. 45.

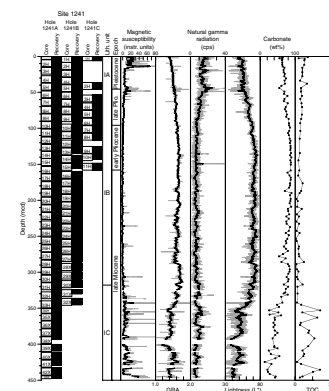


F13. A comparison of the mbsf and mcd scales, p. 46.

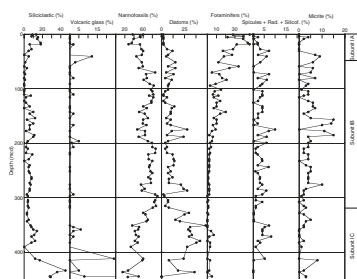


T7. Lithologic Unit I, p. 82.

F14. Lithostratigraphic summary, p. 47.



F15. Siliciclastic, biogenic, and authigenic components, Hole 1241A, p. 48.



650 and 410 nm in reflectance spectra measured in sediment at Site 1241 (Fig. F18). Unlike at previous sites where chlorins have been detected (i.e., Sites 1238–1240), at Site 1241 the normalized depth of the absorption feature at 650 nm is not correlated to the TOC content. However, both TOC and chlorin contents are highest in the lowermost subunit of the sedimentary sequence recovered at Site 1241.

Subunit IA

Intervals: Core 202-1241A-1H through Section 6H-3, 47 cm; Core 202-1241B-1H through Section 6H-2, 57 cm; and Core 202-1241C-1H through Section 2H-CC

Depths: 0–51.55 mcd; Hole 1241A: 0–45.38 mbsf (0.30–51.55 mcd); Hole 1241B: 0–48.47 mbsf (0–51.55 mcd); and Hole 1241C: 0–41.87 mbsf (0.05–46.14 mcd)

Age: Pleistocene to late Pliocene (0–2.1 Ma)

Subunit IA is primarily composed of clayey foraminifer-nannofossil ooze. The sediment is dominated by foraminifers (25%–45%) and nannofossils (30%–60%) with significant amounts of siliciclastics, mainly clays (10%–20%) (Fig. F15). Diatoms are a minor component (<12%) as are the other siliceous biogenic components (i.e., the sum of sponge spicules, radiolarians, and silicoflagellates is ≤7%). Micrite is nearly absent. The abundance of both siliciclastics and foraminifers decreases with depth, whereas nannofossils and diatoms become more significant.

Light–dark color cycles are present on decimeter scales throughout the subunit, with sediment color ranging from olive gray to light olive gray and pale olive (Fig. F19). Color mottling and discrete vertical burrows, including *Zoophycos* traces, are common to abundant throughout Subunit IA. Green and purple-gray color mottles and burrow halos are visible in the pale olive-colored intervals.

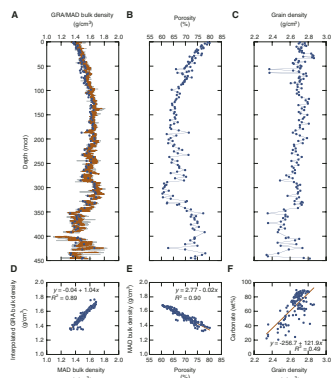
Fourteen of the nineteen volcaniclastic horizons observed in Subunit IA can be correlated between Holes 1241A and 1241B (Table T8). The volcaniclastic horizons include ash layers and lapilli layers or patches (Table T8; Fig. F20). The ashes contain primarily clear glass, with minor amounts of brown glass, plagioclase, biotite, pyroxenes, amphiboles, and quartz. A patch of ash at 27.66 mcd contains only brown glass with rare associated minerals. The lapilli layers and patches contain pumice fragments averaging 3–5 mm in diameter.

Magnetic susceptibility is relatively high in Subunit IA, where values range from 24 instrument units at the top of the subunit to ~3.5 instrument units at 48 mcd (Fig. F14). Natural gamma counts are also elevated (25–35 cps) and variable in this interval. Lightness (L^*) is relatively low, below ~60%. The high-amplitude variability in physical properties, high magnetic susceptibility and NGR values, and low lightness levels help to distinguish Subunit IA from the sediment below. The base of Subunit IA is defined by the base of the ash layer at 51.6 mcd. This layer is recognized in Holes 1241A and 1241B and lies immediately below the shifts in physical properties and the obvious color cycles typical of Subunit IA.

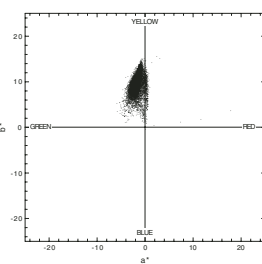
Lithologic Subunit IB

Intervals: 202-1241A-6H-3, 47 cm, through 31H-3, 74 cm; 202-1241B-6H-2, 57 cm, through 30X-5, 70 cm; and 202-1241C-3H-1, 0 cm, through 11H-CC, 23 cm

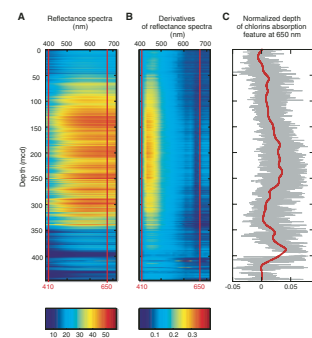
F16. Physical properties measurements, p. 49.



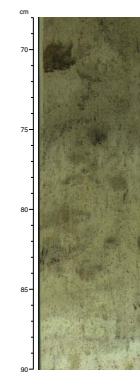
F17. Color measurements, p. 50.



F18. Sequential depth plots, p. 51.



F19. Dark and light color variability, p. 52.



Depths: 51.55–318.44 mcd; Hole 1241A: 45.38–279.41 mbsf (51.55–318.44 mcd); Hole 1241B: 48.47–285.41 mbsf (51.55–318.44 mcd); and Hole 1241C: 47.50–143.69 (53.69–158.46 mcd)

Age: late Pliocene–late Miocene (2.1–9 Ma)

Homogeneous nannofossil ooze dominates Subunit IB, with variable contributions from diatoms and foraminifers (foraminifer-bearing nannofossil ooze, diatom-bearing nannofossil ooze, and clay foraminifer-bearing nannofossil ooze). Overall, siliciclastics are minor, as are other siliceous biogenics and micrite. Sediment color varies slightly between light greenish gray, pale olive, and yellowish gray. Mottling and discrete burrows are less obvious in Subunit IB when compared to the sediment above. However, green and purple-gray color bands and burrow halos are pervasive.

Nannofossil abundance varies between 60% and 85%. Diatom abundance is lower, between 3% and 15%. Foraminifer abundance continues to steadily decline until ~200 mcd and then remains constant at ~3%. The siliceous microfossil abundance averages ~3% with little variability. Micrite presence, although minor, is more common than in Subunit IA, with average values of ~5% and a distinct maximum of ~15% between 160 and 185 mcd.

Subunit IB contains 23 volcaniclastic horizons; 13 of these can be correlated from Hole 1241A to 1241B. Although most of the ash layers contain mainly clear volcanic glass, ash layers that contain predominantly brown glass are more common with increasing depth. Furthermore, only the uppermost five coarse-grained horizons contain pumice, whereas the lowermost four horizons contain scoria grains ranging from sand sized to 3–5 mm in diameter. The clear glass ash also contains plagioclase and biotite, whereas associated minerals are rare within the ash horizons dominated by brown glass.

The lithologic homogeneity of Subunit IB results in less variable physical properties (Fig. F14). Magnetic susceptibility is constantly low, with values ranging between 2 and –2 instrument units. NGR is also low, averaging ~20 cps, with a cyclicity on the order of tens of meters. Lightness (L^*) increases near the top of Subunit IB and reaches a plateau at ~120 mcd, remaining at ~70% through the bottom of the subunit. MAD and GRA bulk densities exhibit trends similar to luminance; they continue to increase at the top of the Subunit IB boundary until ~120 mcd, reaching maximum values of ~1.6–1.7 g/cm³.

The base of Subunit IB is defined as the base of a correlatable ash layer at 318.4 mcd. This horizon approximates the transition from the homogeneous nannofossil ooze to more diatom-rich sediment and the associated shift in physical properties.

Lithologic Subunit IC

Intervals: 202-1241A-31H-3, 74 cm, through 43X-CC, 39 cm, and 202-1241B 30X-5, 70 cm, through 32X-CC, 31 cm

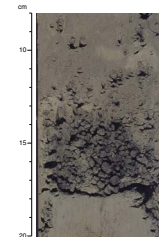
Depths: 318.44–447.06 mcd; Hole 1241A: 279.41–393.67 mbsf (318.44–447.06 mcd); and Hole 1241B: 285.41–306.97 mbsf (318.44–345.26 mcd)

Age: early late Miocene (9–11 Ma)

Subunit IC is composed primarily of clay and diatom-bearing nannofossil ooze with laminated diatom ooze near the base in Cores 202-

T18. List of ash layers, p. 83.

F20. Representative lapilli layer, p. 53.



1241A-40X through 42X. Sediment color ranges from light greenish gray, light olive gray, and pale olive, with olive brown and dark olive gray dominant below Core 202-1241A-38X. Mottles and burrows, including *Zoophycos* traces, are common throughout, except within the laminated diatom ooze intervals (Fig. F21). The laminae are millimeter scale and irregular across the core. Deformational features, including microfaults and soft-sediment folding, are common within the laminated interval. The basal nannofossil ooze underlying the laminated diatom ooze is partially lithified, close to chalk firmness. Mafic sand-sized grains appear at ~400 mcd and become increasingly more abundant downcore. The base of Subunit IC is defined by the presence of basaltic sands and vesicular basalt fragments that are indicative of the basement.

Nannofossil abundance in Subunit IC declines downcore from 80% to <50% (Fig. F15). A corresponding increase in diatom abundance, from ~12% to a maximum of 50%, is present between the top of the subunit and ~340 mcd. Minor contents of foraminifers, biogenic siliceous components, and micrite exhibit no noticeable systematic variations. The presence of disseminated volcanic glass increases below ~350 mcd.

Twenty-nine volcaniclastic horizons are present in Subunit IC, and four have been correlated between holes (Table T8). Brown glass ash continues to increase in importance relative to clear glass at greater depths, and all the coarse-grained layers are composed of scoria. The clear glass ash layers contain the same associated minerals that are present in the upper two subunits, dominated by plagioclase and biotite. The ashes that are dominated by brown glass contain increased amounts of associated minerals, including plagioclase, amphiboles, and pyroxenes, relative to their counterparts in Subunit IB. However, they still tend to have lower amounts of associated minerals than the clear glass ashes. The ash layer present in the interval 202-1241A-42X, 13–26 cm, overlies ~50 cm of coarse black grains. Visually, these two layers appear to constitute a single fining-upward sequence.

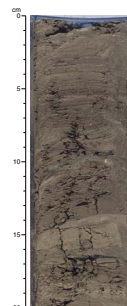
All physical properties display significant changes at the Subunit IB/IC boundary (Fig. F14). Magnetic susceptibility increases to higher average values with significantly greater amplitude variability. The variability in the natural gamma record increases as well, exhibiting slightly elevated levels relative to Subunit IB. A distinct shift in GRA bulk density and lightness (L^*) to lower values occurs at the Subunit IB/IC boundary.

Interpretation and Depositional History

Site 1241 is located at 2027 m water depth in the Panama Basin under relatively low salinity and nutrient-poor surface waters. During the last 11 m.y., the largest shift in sediment composition was a decrease in diatom abundance in the early late Miocene. This major compositional change is accompanied by a decrease in organic carbon content (see “[Geochemistry](#),” p. 15) and chlorins. Moreover, diatom and TOC fluxes were elevated for the entire late Miocene but declined toward less variable, low flux values in the Pliocene–Pleistocene (see “[Age Model and Mass Accumulation Rates](#),” p. 18). These changes are consistent with the tectonic path followed by Site 1241 on the Cocos plate, where the site gradually exited the active equatorial upwelling zone (Pisias et al., 1995).

Nannofossil abundance and fluxes were low for the early part of the late Miocene, increasing significantly after ~7 Ma toward the Pliocene boundary. This pattern could be the result of a change from a diatom-

F21. Laminated diatom ooze, p. 54.



dominated to nannoplankton-dominated ecosystem during the early part of the late Miocene. Alternatively or complementarily, the low carbonate flux between ~11.2 and 7 Ma could be a result of tectonic-related restriction of deepwater exchange between the Atlantic and the Pacific during the Miocene “carbonate crash” (e.g., Lyle et al., 1995), which is known to have affected most of the tropical eastern Pacific. Site 1241 may have been located above the lysocline, at least in the beginning of the “carbonate crash.” The subsequent increase in carbonate accumulation rates after ~7 until ~5 Ma (see “**Age Model and Mass Accumulation Rates,**” p. 18) is possibly related to the “biogenic bloom” observed throughout the tropical Indo-Pacific (e.g., Farrell et al., 1995).

Distinctly high foraminifer contents and correspondingly low diatom and nannofossil abundance characterize the sediment in Subunit IA. The increase in foraminifer abundance continues a rising trend that started around 6 Ma (~200 mcd). Siliciclastics exhibit a consistently high level over the last ~1 m.y. Changes in physical properties reflect these compositional changes. The variability displayed by most of these properties (i.e., magnetic susceptibility, bulk density, and reflectance) is suggestive of orbital cyclicity.

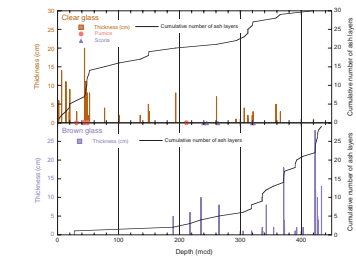
Seventy-two horizons yielding volcaniclastic materials, including patches and layers of ash, pumice, and scoria of lapilli size and an andesite rock fragment were found at Site 1241 (Table T8; Fig. F22). The presence of separate horizons dominated by clear and brown glass suggests that the volcaniclastic material at Site 1241 originated from multiple sources or types of volcanism. Ash layers and patches with clear glass are frequent between sediments dated between 0 and 2.5 Ma (0–55 mcd) and 8 and 9 Ma (300–320 mcd), whereas those with brown glass are increasingly frequent in an interval older than 10 Ma (>320 mcd) (Fig. F23). In addition, pumice and andesite are present above 210 mcd, whereas scoria is present below 240 mcd. The presence of brown glass ash and scoria suggests a more important role for hotspot volcanism during the earlier part of the depositional history of Site 1241, decreasing in significance as the Cocos plate moved the site away from the Galapagos hotspot (see “**Introduction,**” p. 1). The early part of the sedimentary sequence is also characterized by elevated levels of siliciclastics, mainly clays, and mafic sand grains that could be the result of physical and chemical weathering of hotspot volcanic rocks.

The presence of pumice and ash with dominant clear glass and minor brown glass suggests increasing influence of a Central American volcanic source as the site drifted to the northwest. The color of volcanic glass described at DSDP Leg 67 sites provides additional support for a Central American source of volcanics to Site 1241 (Cadet et al., 1982). Frequent ash layers between 0 and 2.5 Ma and 8 and 9 Ma (Fig. F23) correspond to high ash accumulation intervals described at ODP sites in the Caribbean Sea (Sigurdsson et al., 2000), supporting interpretations of intense volcanic activity in Central America during these age intervals.

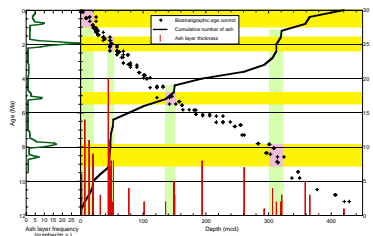
BIOSTRATIGRAPHY

The sedimentary sequence recovered at Site 1241 consists of a 447.06-m-thick interval of Quaternary-lower upper Miocene sediments containing calcareous microfossils throughout and well-preserved diatoms in the Miocene interval (Figs. F24, F40; Table T9). Calcareous nannofossils are abundant and generally well to moderately

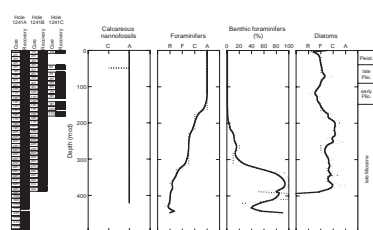
F22. Downhole distribution of volcaniclastic horizons, p. 55.



F23. Volcaniclastic horizons, age vs. depth, p. 56.



F24. Calcareous nannofossils and planktonic and benthic foraminifers, p. 57.



T9. Distribution of calcareous nannofossils, p. 85.

well preserved throughout the sequence. Planktonic foraminifers are abundant to common in the 0- to 217-mcd interval and generally rare below ~217 mcd. The percentage of benthic foraminifers relative to total foraminifers is low (as low as ~1%) in the upper interval and reaches as high as ~99% in the lower interval. Diatoms are rare to few and poorly preserved at depths above 184 mcd. Diatom abundance increases and preservation improves below ~195 mcd.

The index calcareous nannofossil species, *Emiliania huxleyi*, was not observed at this site, suggesting that the 0- to 0.26-Ma interval may be missing. However, planktonic foraminifers suggest that the 0- to 0.12-Ma interval has been recovered. Except for this discrepancy, which should be resolved in postcruise research, the biostratigraphies of the three planktonic microfossil groups document a relatively continuous sequence of early late Miocene–late Pleistocene age (Table T10). The biostratigraphies also show an increase in sedimentation rate (~60 m/m.y.) for the 5- to 7-Ma interval, which may be considered a biogenic bloom interval. Calcareous nannofossils and planktonic foraminifers constrain the basal age of the site at ~11.2–11.6 Ma.

T10. Age-depth control points, p. 87.

Calcareous Nannofossils

Calcareous nannofossils are abundant, and their preservation is generally good to moderate in all the samples examined from Hole 1241A (Table T9). Overgrowth of nannofossils was not apparent in any of the samples, but strong dissolution was noted in a number of samples below ~365 mcd. Reworking of nannofossils is minimal at the site. Most of the well-known nannofossil datums for the Pleistocene–late Miocene have been determined within a sample spacing of ~1.5 m. Nannofossil biostratigraphy suggests that the basal sediment age is 10.8–11.6 Ma. Of taxonomic interest is the new observation of a transitional form between *Discoaster bellus* and *Discoaster berggrenii* at the site. This fills in the missing link between the two species and has implications for biostratigraphy and evolutionary studies.

Samples 202-1241A-1H-1, 0 cm, and 1H-1, 10 cm (0–0.1 mcd), contain abundant and well-preserved late Pleistocene nannofossils, including abundant medium-sized *Gephyrocapsa* spp. and common to abundant *Florisphaera profunda*. *E. huxleyi* and *Pseudoemiliania lacunosa* were not found. This indicates an age between 0.26 and 0.46 Ma for these samples. If this interpretation is correct, it means that the record of the most recent 0.26 m.y. or more is missing from Hole 1241A. Alternatively, if one assumes that the sediment section is complete, it means that *E. huxleyi* has been largely excluded from the site as a result of some unknown anomalous environmental conditions, even though the species has been present in the world's oceans almost universally for the last 0.26 m.y. and abundant for the last 0.08 m.y. Detailed shore-based studies of additional samples from this site and nearby sites should help clarify the problem.

The placements of all the nannofossil datums are listed in Table T10. All the Pleistocene–late Miocene nannofossil datums were well determined without any apparent complications, thanks in part to the virtual absence of reworked nannofossils at the site. The deepest sediment sample (Sample 202-1241A-43X-CC; 446.7 mcd) just above the basement contains abundant nannofossils, including *Reticulofenestra pseudoumbilicus* and *Coccolithus miopelagicus*. The presence of these species in the absence of *Cyclicargolithus floridanus* and *Calcidiscus premacintyrei* indicates an age of 10.8–11.6 Ma.

Planktonic Foraminifers

Planktonic foraminifers are abundant to common in the upper part of Hole 1241A (mudline to Sample 202-1241A-21H-CC; 0–216.69 mcd). Abundance decreases markedly downhole, and the proportion of radiolarians in the >63- μ m coarse fraction increases significantly. Planktonic foraminifers are rare in the lower part of Hole 1241A (Samples 202-1241A-33H-CC to 43X-CC; 349.56–446.67 mcd). Preservation is initially poor at the top of Hole 1241A (mudline to Sample 202-1241A-1H-CC; 0–4.10 mcd), and planktonic tests appear strongly dissolved within this interval. Between Samples 202-1241A-2H-CC and 32H-CC (14.48–337.16 mcd), planktonic tests show minor or moderate evidence of dissolution (etching and fragmentation in 5%–30% of tests). Preservation deteriorates again in the lower part of Hole 1241A (Samples 202-1241A-33H-CC to 43X-CC; 349.56–446.67 mcd).

The Pleistocene–latest Miocene assemblage is a diverse tropical assemblage characterized by *Globigerinoides fistulosus*, *Globorotalia exilis*, *Globorotalia limbata*, *Globorotalia menardii*, *Globorotalia tumida*, *Globigerinoides sacculifer*, *Globigerinoides ruber*, *Globigerinoides trilobus*, *Neogloboquadrina acostaensis*, *Neogloboquadrina dutertrei*, *Orbulina universa*, and *Sphaeroidinella dehiscens*. Standard marker species are present throughout the succession (Tables T10, T11) and can be used to establish a relatively detailed preliminary biostratigraphy for the Pleistocene–uppermost Miocene interval recovered at this site. Thus, Site 1241 offers an excellent opportunity for a well-constrained biostratigraphy and has potential to provide an orbitally tuned low-latitude timescale that will serve as a much-needed reference for the East Pacific.

The preliminary shipboard planktonic foraminifer biostratigraphy is based on core catcher samples from Hole 1241A and some additional samples from Hole 1241C in order to constrain the upper part of the sedimentary sequence. The Pleistocene–latest Miocene biostratigraphy is relatively straightforward. However, the early late Miocene biostratigraphy (Samples 202-1241A-33H-CC to 43X-CC; 349.56–446.67 mcd) is not so well constrained because of poorer preservation and scarcity of planktonic foraminifers (Table T11).

The last occurrence (LO) of *G. ruber* (pink) between the mudline and Sample 202-1241A-1H-CC (0–4.10 mcd) indicates an age younger than 0.12 Ma for the overlying interval. The LO of *G. ruber* (pink) was constrained further at Hole 1241C, between Samples 202-1241C-1H-2, 80–81 cm, and 1H-3, 80–81 cm (2.35–3.86 mcd). The standard marker *Globorotalia tosaensis* is extremely rare at Site 1241 and could not be used to define the boundary between Subzones Pt1a and Pt1b of Berggren et al. (1995). The LO of representatives of the benthic genus *Stilostomella* (~0.65 Ma), between Samples 202-1241A-2H-CC and 3H-CC, provides an alternative datum to approximate this boundary. However, this extinction event was probably diachronous at low and high latitudes (Hayward, 2001), and detailed shore-based studies from Site 1241 and from the southern Leg 202 sites are needed to clarify the timing of this event in the eastern Pacific.

Benthic Foraminifers

The percentage of benthic foraminifers relative to total foraminifers is initially low (typically ~1%) in the upper part of Hole 1241A (mudline to Sample 202-1241A-21H-CC; 0–216.69 mcd). The proportion of benthic foraminifers increases markedly below this depth, reaching

T11. Distribution of planktonic foraminifers, p. 89.

~99% between Samples 202-1241A-33H-CC and 39X-CC (349.56–409.21 mcd). Benthic foraminifers, overall, exhibit better preservation than planktonic foraminifers but start to show dissolution damage in sediments from the lowermost part of Hole 1241A (Samples 202-1241A-33H-CC to 43X-CC; 349.56–446.67 mcd) (Fig. F24).

The relatively diverse, but sparse, Pleistocene–latest Miocene assemblage in Samples 202-1241A-1H-CC to 21H-CC characterizes a mesotrophic middle bathyal environment. It typically contains *Eggerella bradyi*, *Eubulimina exilis*, *Globocassidulina subglobosa*, *Globobulimina affinis*, *Globobulimina pyrula*, *Gyroidinoides soldanii*, *Gyroidinoides orbicularis*, *Karreriella bradyi*, *Laticarinina pauperata*, *Melonis affinis*, *Melonis pom-pilioides*, *Neugeborina longiscata*, *Oridorsalis umbonatus*, *Pleurostomella brevis*, *Pullenia bulloides*, *Pullenia quinqueloba*, *Pyrgo murrhina*, *Pyrgo serrata*, *Stilostomella subspinosa*, *Uvigerina peregrina*, and *Uvigerina proboscidea*. The late Miocene assemblage in Samples 202-1241A-22H-CC through 43X-CC generally shows much higher abundance, and assemblage composition overall reflects shallower upper bathyal water depths or increased carbon fluxes at the seafloor. Marked variations in composition (particularly in the proportions of *Bolivina*, *Bulimina*, *Globobulimina*, and *Uvigerina*) may relate to changes in productivity or circulation. However, it was not possible to evaluate from shipboard study to what extent these changes indicate fluctuations in productivity and/or circulation or stem from a preservation bias.

Diatoms

All core catcher samples from Hole 1241A, as well as smear slides from some additional layers of the split cores, were analyzed. Diatoms are rare to few, and preservation is poor from the mudline down to Sample 202-1241A-18H-CC (184 mcd), but abundance increases and preservation improves below Sample 19H-CC (195 mcd) (Table T12; Fig. F24). Between Samples 202-1241A-32H-CC and 37X-6, 38 cm (337–386 mcd), diatom abundance increases significantly. In this interval, diatom oozes dominated by highly fragmented *Thalassiothrix* spp. are present, interbedded with the nannofossil ooze.

Diatoms recovered from Site 1241 indicate a continuous stratigraphic interval from the Holocene *Fragilariopsis doliolus* Zone to the *Actinocyclus moronensis* Zone. The diatom flora present provides 20 stratigraphic events for the 447 mcd recovered from this site. However, accurate placement of some of these events was difficult in intervals with lower abundance and poorer preservation of diatoms, such as the top 18 cores (0–184 mcd). Diatom events recognized are presented in Table T10.

[T12. Distribution of diatoms, p. 93.](#)

PALEOMAGNETISM

Natural Remanent Magnetization

The natural remanent magnetization (NRM) of archive-half sections from Holes 1241A, 1241B, and 1241C was measured then remeasured after alternating-field (AF) demagnetization at selected levels. Sections within Cores 202-1241A-1H through 5H were then AF demagnetized at peak alternating fields of 10, 15, and 20 mT and measured. All other cores from Holes 1241A, 1241B, and 1241C were demagnetized at 20 mT and then measured. A few sections from Cores 202-1241A-9H through 11H were also demagnetized at 30 or 40 mT to further evaluate

the strength of the drilling overprint. Sections obviously affected by drilling disturbance were not measured.

The NRM intensity before and after demagnetization shows the same general downhole trend with ~1 to 1.5 orders of magnitude less intensity after 20-mT AF demagnetization than before (Fig. F25). NRM intensities after AF demagnetization are ~0.004 A/m at the top and decrease to <10⁻⁴ A/m by ~100 mcd (Fig. F25). NRM intensities remain low until ~275 mcd, but at greater depths they rise to values similar to those observed at the surface (~310 mcd), before decreasing again by a factor of five. Throughout the section, intensities vary by a factor of five on a meter scale with many ~10-cm order-of-magnitude spikes in intensity resulting from ash layers or turbidites (see “**Lithostratigraphy**,” p. 5).

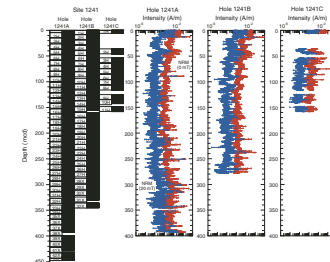
The NRM intensities before and after AF demagnetization at 20 mT decrease by one and two orders of magnitude, respectively, over the uppermost 15 m (Fig. F26). The first order of magnitude loss in NRM (20 mT) occurs in the uppermost 5 m and may be associated with magnetic mineral dissolution resulting from reducing conditions. All three parameters display quasi-cyclic variations of ~2-m scale from 0 to 13 mcd, which is consistent with the dominant ~100-k.y. climate cycle of the late Pleistocene based on sedimentation rates of 21 m/m.y. (see “**Age Model and Mass Accumulation Rates**,” p. 18). The NRM (20 mT) also displays an order of magnitude intensity decrease between 13 and 15 mcd. The NRM (0 mT) and magnetic susceptibility also decrease by a factor of five at this depth. This change may be partially related to changes in sediment flux, as the dramatic intensity cyclicity of the uppermost 15 m also disappears at this depth.

Directional Variability

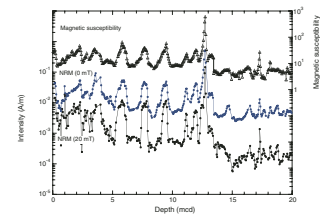
Inclinations before AF demagnetization are steeply positive, characteristic of a drill string-induced magnetic overprint (Fig. F27). For the uppermost 15 mcd, inclination values after 25-mT AF demagnetization are closer but still more positive than expected for the Site 1241 latitude (~12° for an axial geocentric dipole) (Fig. F27). Below 20 mcd, sediments are more strongly overprinted, with steep positive inclinations present throughout after 20-mT AF demagnetization and even after selective demagnetization at 30 or 40 mT.

Declinations within individual cores from the upper 20 mcd are generally quite similar in value. In Core 202-1241A-3H, declinations change significantly in direction, suggesting the presence of polarity transitions (Fig. F28). Such polarity transitions are seen in Cores 202-1241A-3H (~15, 20, and 22 mcd), 202-1241B-2H (~15 mcd), and 202-1241B-3H (~20 mcd). The interpretation of these declination changes of ~180° that occur within single cores as polarity transitions is unambiguous, despite the lack of the Tensor orientation tool corroboration (the tool is not used in the uppermost three cores for operational reasons). The ages of these interpreted transitions are consistent with biostratigraphic age estimates (Table T10; see “**Biostratigraphy**,” p. 10). The Brunhes/Matuyama (0.78 Ma) boundary is present between 14.7 and 15.0 mcd, the upper Jaramillo transition (0.99 Ma) is present at 19.7–20.0 mcd, and the lower Jaramillo transition (1.07 Ma) is present at 21.5–21.9 mcd. No other polarity boundaries below this interval could be discerned.

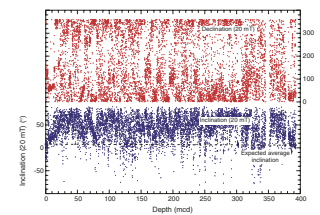
F25. Initial and AF demagnetized NRM intensities, p. 58.



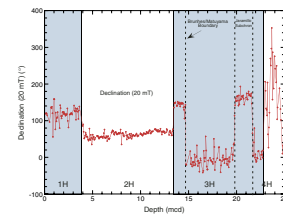
F26. Initial and AF demagnetized NRM magnetic susceptibilities and intensities, 0–20 mcd, p. 59.



F27. NRM inclinations and declinations, p. 60.



F28. Declinations showing possible polarity transitions, p. 61.



GEOCHEMISTRY

Sediment Gases

Concentrations of headspace gases were routinely monitored in Hole 1241A sediments according to shipboard safety and pollution prevention considerations. Methane concentrations in headspace samples were low, always <15 ppmv and as low as ambient levels in the shallowest and deepest samples (Fig. F29; Table T13). Methane concentrations were generally >8 ppmv from 62.9 to 287.9 mcd. Low methane concentrations indicate that methanogenesis is limited at this site because of low organic matter concentrations in the sediments (see “[Sedimentary Inorganic Carbon, Organic Carbon, and Nitrogen Concentrations](#),” p. 16). No higher molecular weight hydrocarbons were observed.

Interstitial Water Geochemistry

We collected 36 interstitial water samples from Hole 1241A for shipboard analyses. Chemical gradients at this site (Table T14; Fig. F30) reflect the limited influence of organic matter oxidation, the dissolution of biogenic silica driven by the relatively low thermal gradient, and biogenic calcite recrystallization. Many of the profiles are consistent with a flow of relatively unaltered seawater in the underlying oceanic crust, but the lack of major change in composition makes this more difficult to assess than at Site 1240.

Chlorinity averages 559 mM with little variation with depth or lithologic subunit (Fig. F30). Salinity, measured refractively as total dissolved solids, is 35 throughout (Table T14). Sodium concentrations measured by inductively coupled plasma–atomic emission spectrometry averaged 2.4% higher than those estimated by charge balance reported here (Table T14). Sodium concentrations parallel the limited variations in chlorinity, with a total range from 477 to 489 mM.

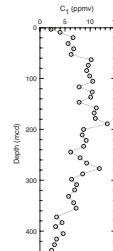
Organic matter diagenesis, driven by microbially mediated oxidation reactions, has a limited influence on the interstitial water chemistry. Sulfate shows depletion relative to seawater values by no more than 4–5 mM, with the smell of hydrogen sulfide noted in some of the interstitial water samples with lower sulfate concentrations. The limited degree of sulfate reduction is a consequence of the relatively organic carbon-poor sediments, and the presence of sulfate limits methanogenesis. Alkalinity increases from 3.6 mM at 3.3 mcd to >5 mM from 62.9 to 95.1 mcd then decreases to <3 mM in Subunit IC.

Dissolved manganese concentrations are >12 µM from 3.3 to 9.3 mcd, decrease to low values throughout Subunit IB, then increase from 0.6 µM at 298.1 mcd to 19.3 µM at 437.5 mcd. The shallow manganese peak represents suboxic diagenesis of organic matter, whereas the deeper one results from basalt alteration. Dissolved iron is present at relatively low concentrations, presumably reflecting a limited supply of reducible iron minerals.

Phosphate concentrations decrease from 4.9 µM at 3.3 mcd to 2.2 µM at 52.5 mcd near the base of Subunit IA then decline further in Subunits IB and IC to below the detection limit (0.2 µM) at 445.4 mcd. Ammonium concentrations increase from 93 µM at 3.3 mcd to >400 µM from 52.5 to 105.7 mcd then decline steadily to 31 µM at 445.4 mcd.

Dissolved silicate concentrations increase from 551 µM at 3.3 mcd to >1000 µM in most of Subunit IC then decline in the deepest two samples. Site 1241 has a significantly lower thermal gradient (~2.7°C/100

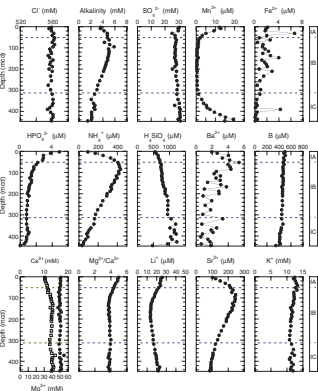
F29. Headspace methane vs. depth, p. 62.



T13. Headspace gas concentrations, p. 97.

T14. Interstitial water geochemical data, p. 98.

F30. Interstitial water geochemical data, p. 63.



m) than Site 1238 (~12.7°C/100 m) or Site 1239 (~9.4°C/100 m) (see “[Operations](#),” p. 3). The silicate increase with depth for Site 1241 is also much less steep than those observed at Sites 1238 and 1239, and Site 1241 never reaches high enough temperatures to reach the high silicate concentrations (>1800 µM) seen at depth in Sites 1238 and 1239.

Barium concentrations are low (<6 µM) throughout, indicating that sulfate concentrations are sufficient to prevent significant dissolution of barite. Boron concentrations decrease from 502 µM at 3.3 mcd to 349 µM at 445.4 mcd.

Calcium concentrations increase in Subunit IA and the top of Sub-unit IB from 10.3 mM at 3.3 mcd to >12 mM by 84.5 mcd. Limited organic carbon oxidation drives only a small increase in alkalinity, which is too low to result in authigenic carbonate precipitation sufficient to lower calcium concentrations. Smear slide observations indicated only minor amounts of micrite throughout Site 1241 (see “[Lithostratigraphy](#),” p. 5). Magnesium concentrations average ~50 mM, with little variation with depth. Magnesium/calcium ratios decrease from 5.0 at 3.3 mcd to <4 by 84.5 mcd and remain low throughout (Fig. [F30](#)).

Lithium concentrations decrease from 26 µM at 3.3 mcd to <14 µM from 146.6 to 200.3 mcd then increase to >20 µM from 404.8 mcd and deeper. Strontium concentrations increase from 101 µM at 3.3 mcd to >240 µM from 84.5 to 116.6 mcd and decrease to 85 µM at 445.4 mcd. The middepth maximum is characteristic of the influence of biogenic calcite recrystallization, whereas the decrease with increasing depth must represent either a sink at depth via basalt alteration or a return to seawater values from the influence of fluid flow in the underlying oceanic crust as observed at Site 1240. Potassium concentrations have little variation with depth.

Sedimentary Inorganic Carbon, Organic Carbon, and Nitrogen Concentrations

Inorganic carbon (IC), total carbon (TC), and total nitrogen (TN) concentrations were determined on sediment samples from Hole 1241A (Table [T15](#)). Organic matter carbon/nitrogen ratios were employed to characterize the organic matter.

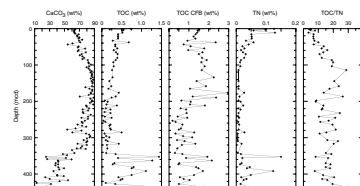
Calcium carbonate concentrations range between 12.8 and 89.3 wt% (average = 67.8 wt%) (Table [T15](#); Fig. [F31](#)). Concentrations increase gradually from ~63 to generally >80 wt% to 208.8 mcd, with a minimum of 54% at 43.9 mcd. Calcium carbonate concentrations decrease to ~54 wt% at 277.7 mcd then increase to values >80 wt% from 291.6 to 309.5 mcd. Calcium carbonate concentrations then generally decline with depth, with values ranging from 13 to 60 wt% at depths >350 mcd.

Total organic carbon (TOC) concentrations range between 0.05 and 1.4 wt% (average = 0.4 wt%) (Table [T15](#); Fig. [F31](#)). In the uppermost ~342 mcd, the TOC concentrations reach their highest values in the depth interval from 345.0 to 446.0 mcd, with peak values as high as 1.4 wt%. The interval of maximum TOC values >350 mcd corresponds to the interval of minimum calcium carbonate concentrations. Calculating TOC on a carbonate-free basis indicate that TOC variations are not caused solely by variable calcium carbonate dilution (Fig. [F31](#)).

TN concentrations vary similarly to TOC (Fig. [F31](#)). The TOC/TN ratios increase from 5 to 30 in the uppermost ~100 mcd and remain high at greater depth. Low TOC/TN ratios in the uppermost 40 mcd indicate a marine origin of the organic matter (Bordovskiy, 1965; Emerson and

T15. IC, CaCO_3 , TC, TOC, TN, TOC CFB, and concentrations, and TOC/TN ratios, p. 99.

F31. Calcium carbonate, TOC, TOC CFB, TN, and TOC/TN vs. depth, p. 64.



Hedges, 1988; Meyers, 1997). Higher TOC/TN ratios can reflect a preferential loss of nitrogen relative to carbon during burial diagenesis of organic matter (Meyers, 1997). In sediments with low TOC concentrations, inorganic nitrogen from ammonium sorbed in the lattice of clay minerals may contribute significantly to the total nitrogen content (Müller, 1977) and TOC/TN ratios may not accurately reflect organic matter composition.

DOWNHOLE MEASUREMENTS

Logging Operations

Downhole logging was performed in Hole 1241B after it had been drilled to a depth of 395 mbsf with an 11.438-in APC/XCB drill bit (see “[Operations](#),” p. 3) and displaced with sepiolite mud and the pipe was set at 82 mbsf. Two tool string configurations were run, the triple combo-MGT and the FMS-sonic (see “[Downhole Measurements](#),” p. 36, in the “Explanatory Notes” chapter). No problems were encountered while logging, and all passes reached the base of the hole. Details of the intervals logged with each configuration, together with the position of the drill bit, are shown in Figure F32. The Dipole Sonic Imager (DSI) on the FMS-sonic was run in P&S (middle frequency), lower dipole (low frequency), and first motion detection (FMD) modes. Weather was excellent, and the sea state was calm with peak heave <2 m. The wireline heave compensator was used throughout the logging operation.

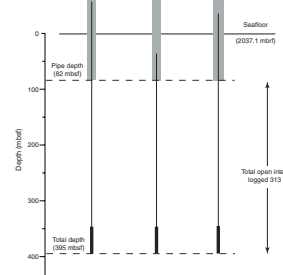
Data Quality

The caliper log (Fig. F33) shows that the borehole was relatively smooth and that the diameter varied between 10.5 and 14.3 in (mean = 12.0 in; standard deviation = 1.1 in), resulting in excellent data from the density, porosity, and FMS tools that require good borehole contact. Hole deviation increased slightly with depth, reaching a maximum of 2.6°. Downhole log-derived densities mirror the downhole porosities and closely match with core measurements (Figs. F34, F35). NGR measurements are highly reproducible between tools and passes and are similar to the core-derived natural gamma record from Hole 1241A (Figs. F33, F36). Sonic velocities were low but generally reliable from 180 mbsf to the bottom of the hole (Fig. F34).

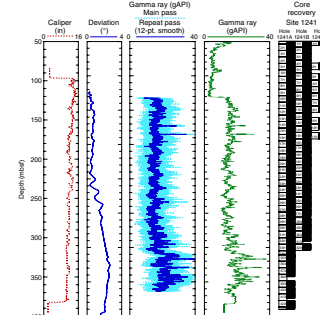
Results

Overall, the physical properties at the site are homogeneous, suggesting a fairly uniform lithology throughout the sequence. No clear compaction-related trends are indicated with depth. Instead, sonic velocity, density, and resistivity show broad maxima from 260 to 280 mbsf associated with a minimum in porosity. One short and two long intervals marked by particularly low density, resistivity, and sonic velocity are present at 165–168, 192–258, and 305–365 mbsf, respectively, and correspond to intervals with relatively high diatom abundances in the cores (see “[Biostratigraphy](#),” p. 10). Superimposed upon these broad-scale changes in physical properties, meter-scale covariations in density and resistivity, similar to those observed at Sites 1238 and 1239, occur throughout the sequence (Figs. F34, F37). As at the earlier sites, these

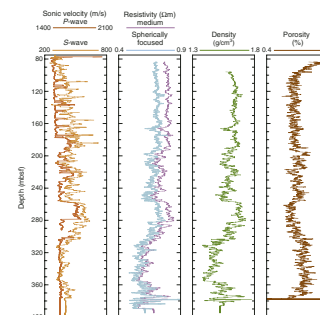
F32. Logging tool string deployments, p. 65.



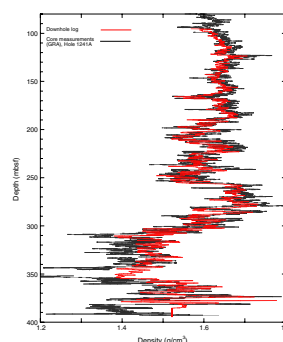
F33. Caliper, deviation, and gamma ray records, p. 66.



F34. Sonic velocity, resistivity, density, and porosity data, p. 67.



F35. Log and core density, p. 68.



meter-scale density and resistivity fluctuations are most likely related to the silica to carbonate oscillations observed in the cores (see “[Lithostratigraphy](#),” p. 5). Banding on the FMS images occurs on the same scale as the density and resistivity changes associated with the nannofossil to diatom oscillations (Fig. [F38](#)).

Natural Gamma Radiation

The NGR activity in Hole 1241A shows significant meter- and dekameter-scale variability superimposed upon a general increase with depth (Figs. [F33](#), [F36](#)). The spectral gamma results from the Hostile Environment Gamma Ray Sonde (HNGS) tool (Fig. [F36](#)) show very low Th activity throughout the sequence and K activity at or below the tool detection limit. In contrast, the U activity and variability is much greater, reaching its highest values below 310 mbsf. The high overall U activity dominates the total gamma ray activity of the sediments. As at Sites 1238 and 1239, the dominance of the U activity over Th and K activity indicates that changes in sedimentary redox conditions related to organic matter, rather than terrigenous input, control sediment gamma ray activity at Site 1241. However both the U and total counts are significantly lower at Site 1241 than at Sites 1238 and 1239, suggesting both organic and terrigenous components are relatively lower at Site 1241.

Core-Log Comparisons

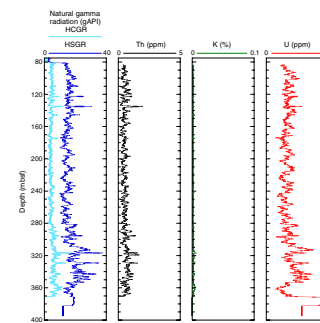
Log-derived density records show close agreement with core measurements down to the meter scale (Fig. [F35](#)). Using the downhole log density and natural gamma records as a depth reference, core measurements were mapped to an equivalent log depth (eld) using the software program Sagan in order to identify more precisely the size and position of core breaks within the XCB section (see “[Composite Section](#),” p. 4).

Despite the close relationship between core and log densities, the lower resolution of the downhole log prevents core-log comparisons to the decimeter and centimeter scale. However, the relationship between resistivity and density in the downhole logs is strongly linear ($r = 0.96$) throughout the logged sequence, suggesting a common lithologic control on both properties (Fig. [F37](#)). This circumstance provides an opportunity for much higher resolution core-log comparison based on the FMS log, which uses 64 microelectrodes to generate an electrical conductivity image of the borehole with resolution of ~1 cm. A comparison between the spherically focused resistivity log, with a resolution similar to that of the downhole density log, and the conductivity curve derived by averaging the 64 channels of FMS data, suggests that a significant amount of higher-frequency variability is missed by the conventional resistivity log at this site (Fig. [F39](#)). This higher-frequency microconductivity variability is comparable with the GRA density records to the centimeter scale (Fig. [F38](#)), suggesting that the FMS data may allow centimeter-scale core-log comparisons for much of the sequence.

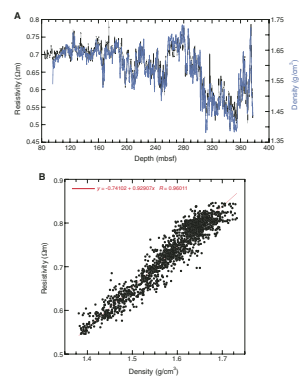
AGE MODEL AND MASS ACCUMULATION RATES

A 447.8-mcd thick (394.2 mbsf) upper Miocene (~12 Ma) to Holocene pelagic sediment sequence was recovered at Site 1241. Biostratigraphic datums (see Table [T10](#)) were used to construct an age-depth

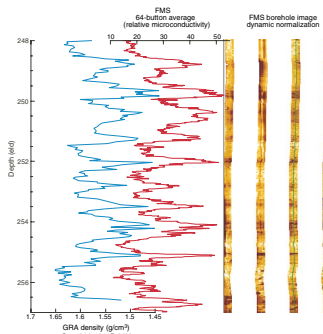
F36. Total and spectral gamma ray records, p. 69.



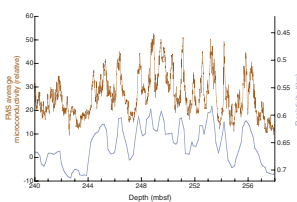
F37. Density and resistivity logs and scatter plot, p. 70.



F38. FMS image illustrating the meter-scale banding, p. 71.



F39. DIT vs. FMS resistivity, p. 72.



model for this site (Table T16; Fig. F40). Linear sedimentation rates (LSRs), total MARs, and carbonate MARs were calculated at 1-m.y. intervals (see “**Age Models and Mass Accumulation Rates**,” p. 41, in the “Explanatory Notes” chapter).

Age-Depth Model

Relatively good agreement exists among microfossil datums from the top ~100 mcd of the section recovered at Site 1241 (Fig. F40). We relied primarily, although not exclusively, upon available calcareous nannofossil datums to define the age-depth model. The increasing scatter in biostratigraphic data downhole results partly from decreasing calcareous microfossil abundance and from increased carbonate dissolution below 365 mcd (see “**Biostratigraphy**,” p. 10). The age model trend below 250 mcd (~7 Ma) is not very reliable. Had we chosen to emphasize the planktonic foraminifer datums, a significantly different model would have resulted in that interval.

Linear Sedimentation and Mass Accumulation Rates

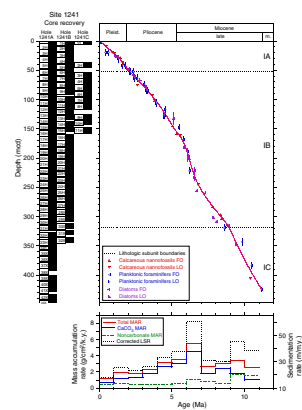
LSRs range between 18 and 60 m/m.y., and total MARs range from ~1 to 5.6 g/cm²/ky. All rates have a minor peak at 10–9 Ma and a rather well constrained main peak at 7–6 Ma. After 6 Ma, the LSRs and MARs decline gradually. Diverging trends between LSR and MAR are obvious in the intervals from 11 to 9 Ma (below 340 mcd) and from 7 to 6 Ma (~185–250 mcd) as a result of higher porosity and biogenic opal concentrations. No divergence is seen for the top of the sequence although porosity is characteristically high. This trend can be explained by a relatively high average grain density that results from the increased siliciclastic content in the top 30 mcd of the sediment sequence.

The oldest interval (11–9 Ma) with relatively high concentrations of biogenic opal and organic carbon corresponds to the “Miocene carbonate crash,” an interval of poor carbonate preservation recognized in equatorial East Pacific sediments below 3000 m water depth (Lyle et al., 1995). Even though Site 1241 was at a paleowater depth above the lysocline at that time (see “**Introduction**,” p. 1), benthic and planktonic foraminiferal tests also appear strongly affected by carbonate dissolution over this interval (see “**Biostratigraphy**,” p. 10). The apparent high biogenic opal deposition from 11 to 9 Ma has no equivalent at the other Leg 202 sites but is consistent with a paleolocation near the equator at that time, driven by drift of the Cocos plate (see “**Introduction**,” p. 1). Given the high concentrations in diatoms and organic carbon and the suffered carbonate losses, the resulting total biogenic accumulation rate would clearly suggest an interval of enhanced productivity. Carbonate dissolution was likely enhanced by an increase in the rain ratio of organic carbon to carbonate to the seafloor (Archer, 1991).

High carbonate MARs returned by 7 Ma, when carbonate MARs also increased at other sites. However, at this site the carbonate MARs declined after 6 Ma, when the rates still increased at Southern Hemisphere Sites 1236 through 1239, indicating that this site experienced different regional oceanographic conditions during that time. A similar early decrease in LSRs at Sites 852–854 (Shackleton et al., 1995) suggest a significant difference in the timing of peak production in the Northern and Southern Hemispheres.

T16. Age-depth model, LSRs, and MARs, p. 101.

F40. Biostratigraphic and magnetostratigraphic datums and age-depth model, p. 73.



REFERENCES

- Archer, D., 1991. Modeling the calcite lysocline. *J. Geophys. Res.*, 96:17037–17050.
- Behrenfeld, M.J., Randerson, J.T., McClain, C.R., Feldman, G.C., Los, S.O., Tucker, C.J., Falkowski, P.G., Field, C.B., Frouin, R., Esaias, W.E., Kolber, D.D., and Pollack, N.H., 2001. Biospheric primary production during and ENSO transition. *Science*, 291:2594–2597.
- Berggren, W.A., Kent, D.V., Swisher, C.C., III, and Aubry, M.-P., 1995. A revised Cenozoic geochronology and chronostratigraphy. In Berggren, W.A., Kent, D.V., Aubry, M.-P., and Hardenbol, J. (Eds.), *Geochronology, Time Scales and Global Stratigraphic Correlation*. Spec. Publ.—SEPM, 54:129–212.
- Bordovskiy, O.K., 1965. Accumulation and transformation of organic substances in marine sediment, 2. Sources of organic matter in marine basins. *Mar. Geol.*, 3:5–31.
- Cadet, J.-P., Pouclet, A., Thisse, Y., Bardintzeff, J.M., and Azéma, J., 1982. Middle America Neogene explosive volcanism and ash layers: evidence from the Middle America Trench transect, Deep Sea Drilling Project Leg 67. In Aubouin, J., von Huene, R., et al., *Init. Repts. DSDP*, 67: Washington (U.S. Govt. Printing Office), 475–491.
- Emerson, S., and Hedges, J.I., 1988. Processes controlling the organic carbon content of open ocean sediments. *Paleoceanography*, 3:621–634.
- Farrell, J.W., Raffi, I., Janecek, T.C., Murray, D.W., Levitan, M., Dadey, K.A., Emeis, K.-C., Lyle, M., Flores, J.-A., and Hovan, S., 1995. Late Neogene sedimentation patterns in the eastern equatorial Pacific. In Pisias, N.G., Mayer, L.A., Janecek, T.R., Palmer-Julson, A., and van Andel, T.H. (Eds.), *Proc. ODP, Sci. Results*, 138: College Station, TX (Ocean Drilling Program), 717–756.
- Ganeshram, R.S., Pedersen, T.F., Calvert, S.E., and Murray, J.W., 1995. Large changes in oceanic nutrient inventories from glacial to interglacial periods. *Nature*, 376:755–758.
- Haug, G.H., Tiedemann, R., Zahn, R., and Ravelo, A.C., 2001. Role of Panama uplift on oceanic freshwater balance. *Geology*, 29:207–210.
- Hayward, B.W., 2001. Global deep-sea extinctions during the Pleistocene ice-ages. *Geology*, 29:599–602.
- Hey, R., Johnson, G.L., and Lowrie, A., 1977. Recent plate motions in the Galapagos area. *Geol. Soc. Am. Bull.*, 88:1385–1403.
- Kroopnick, P., 1974. The dissolved O₂-CO₂-¹³C system in the eastern equatorial Pacific. *Deep-Sea Res. Part A*, 21:211–227.
- Leckie, R.M., Sigurdsson, H., Acton, G.D., and Draper, G. (Eds.), 2000. *Proc. ODP, Sci. Results*, 165: College Station, TX (Ocean Drilling Program).
- Ledbetter, M.T., 1985. Tephrochronology of marine tephra adjacent to Central America. *Geol. Soc. Am. Bull.*, 96:77–82.
- Lyle, M., Dadey, K.A., and Farrell, J.W., 1995. The late Miocene (11–8 Ma) eastern Pacific carbonate crash: evidence for reorganization of deep-water circulation by the closure of the Panama Gateway. In Pisias, N.G., Mayer, L.A., Janecek, T.R., Palmer-Julson, A., and van Andel, T.H. (Eds.), *Proc. ODP, Sci. Results*, 138: College Station, TX (Ocean Drilling Program), 821–838.
- Lyle, M., Liberty, L., Mix, A., Pisias, N., Goldfinger, C., Hulett, D., Janik, A., 2000. *Site Survey Data Package 5: Site Surveys for ODP Leg 201 from the NEMO-3 Cruise, in Support of Proposal 465: Southeast Pacific Paleoceanographic Transects*. CGISS Tech. Rpt. 2000-06, Boise State University.
- Meyers, P.A., 1997. Organic geochemical proxies of paleoceanographic, paleolimnologic, and paleoclimatic processes. *Org. Geochem.*, 27:213–250.
- Mix, A.C., Morey, A.E., Pisias, N.G., and Hostetler, S., 1999. Foraminiferal faunal estimates of paleotemperatures: circumventing the no-analog problems yields cool ice-age tropics. *Paleoceanography*, 14:350–359.

- Mix, A.C., Pisias, N.G., Goldfinger, C., Lyle, M., Liberty, L., Janik, A., Hebbeln, D., Wefer, G., and Lamy, F., 2000. *Southeast Pacific Paleceanographic Transects, Site Survey Data Package 4: NEMO Expedition, Leg III, R/V Melville, May–June 2000*: Corvallis (Oregon State Univ.).
- Müller, P.J., 1977. C/N ratios in Pacific deep sea sediments: effect of inorganic ammonium and organic nitrogen compounds sorbed by clays. *Geochim. Cosmochim. Acta*, 41:765–776.
- Ocean Climate Laboratory, 1999. *World Ocean Atlas 1998 (WOA98)* [CD-ROM]. Available from: National Climatic Data Center, Asheville NC 28801-5001, USA.
- Peterson, L.C., Murray, D.W., Ehrmann, W.U., and Hempel, P., 1992. Cenozoic carbonate accumulation and compensation depth changes in the Indian Ocean. In Duncan, R.A., Rea, D.K., Kidd, R.B., von Rad, U., and Weissel, J.K. (Eds.), *Synthesis of Results from Scientific Drilling in the Indian Ocean*. Geophys. Monogr., Am. Geophys. Union, 70:311–333.
- Pisias, N.G., Mayer, L.A., and Mix, A.C., 1995. Paleoceanography of the eastern equatorial Pacific during the Neogene: synthesis of Leg 138 drilling results. In Pisias, N.G., Mayer, L.A., Janecek, T.R., Palmer-Julson, A., and van Andel, T.H. (Eds.), *Proc. ODP, Sci. Results*, 138: College Station, TX (Ocean Drilling Program), 5–21.
- Pisias, N.G., and Mix, A.C., 1997. Spatial and temporal oceanographic variability of the eastern equatorial Pacific during the late Pleistocene: evidence from radiolaria microfossils. *Paleoceanography*, 12:381–393.
- Shackleton, N.J., Crowhurst, S., Hagelberg, T., Pisias, N.G., and Schneider, D.A., 1995. A new late Neogene time scale: application to Leg 138 sites. In Pisias, N.G., Mayer, L.A., Janecek, T.R., Palmer-Julson, A., and van Andel, T.H. (Eds.), *Proc. ODP, Sci. Results*, 138: College Station, TX (Ocean Drilling Program), 73–101.
- Sigurdsson, H., Kelley, S., Leckie, R.M., Carey, S., Bralower, T., and King, J., 2000. History of circum-Caribbean explosive volcanism: $^{40}\text{Ar}/^{39}\text{Ar}$ dating of tephra layers. In Leckie, R.M., Sigurdsson, H., Acton, G.D., and Draper, G. (Eds.), *Proc. ODP, Sci. Results*, 165: College Station, TX (Ocean Drilling Program), 299–314.
- Tsuchiya, M., and Talley, L.D., 1998. A Pacific hydrographic section at 88°W: water-property distribution. *J. Geophys. Res.*, 103:12899–12918.

Figure F1. Locations of Sites 1238–1242 and regional bathymetry of the Panama and Guatemala Basins, which are separated by Cocos Ridge. To the south is Carnegie Ridge. The Panama Basin is split by the Cocos-Nazca spreading center.

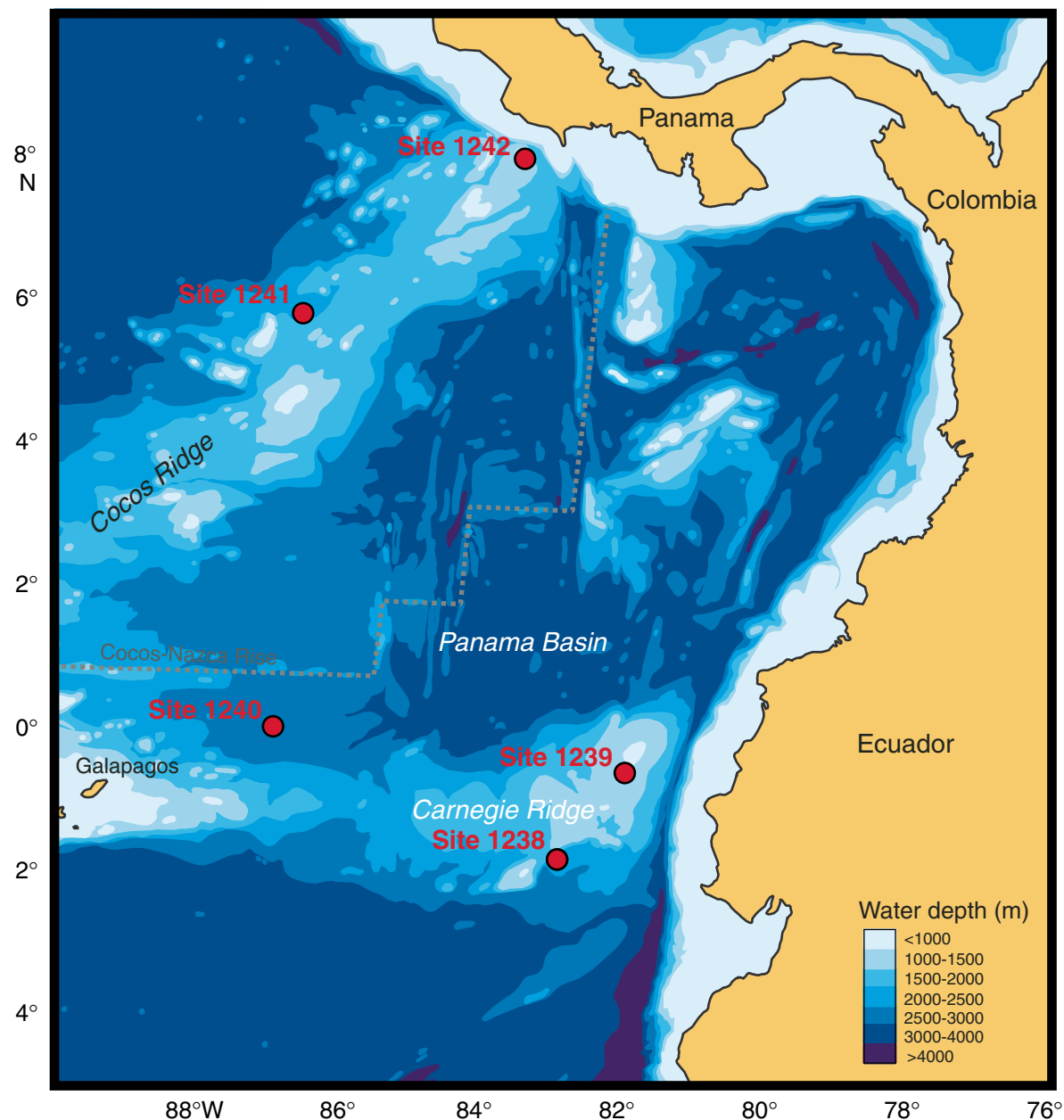


Figure F2. High-resolution swath bathymetry, illustrated in an oblique view (Mix et al., 2000). The abyssal hill topography illustrated here covers an area of ~50 km (northwest-southeast) \times 20 km (northeast-southwest).

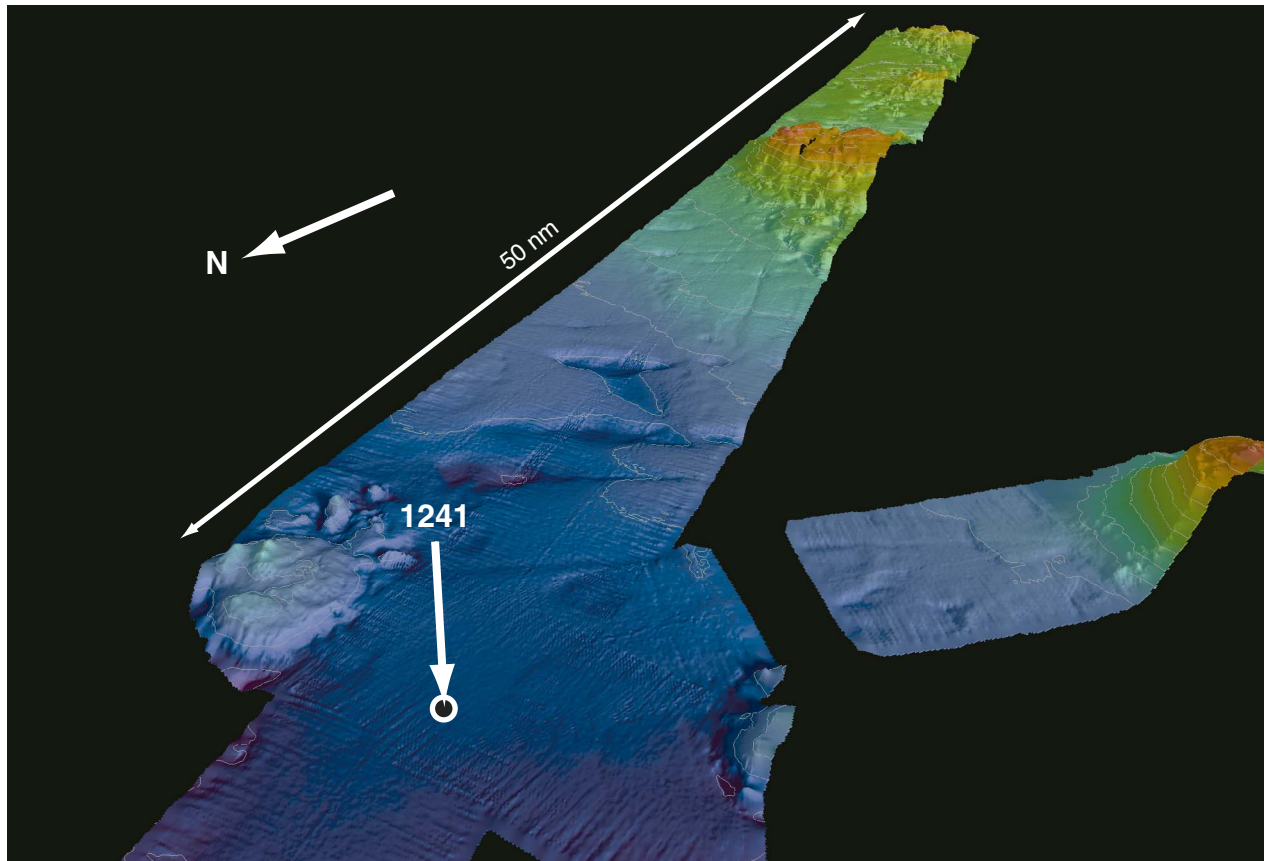


Figure F3. Primary tectonic features of the Panama Basin and surroundings (after Hey et al., 1977). Bold black lines = active oceanic spreading centers, red lines = age (in millions of years) of oceanic crust. EPR = East Pacific Rise, CNR = Cocos-Nazca Rift.

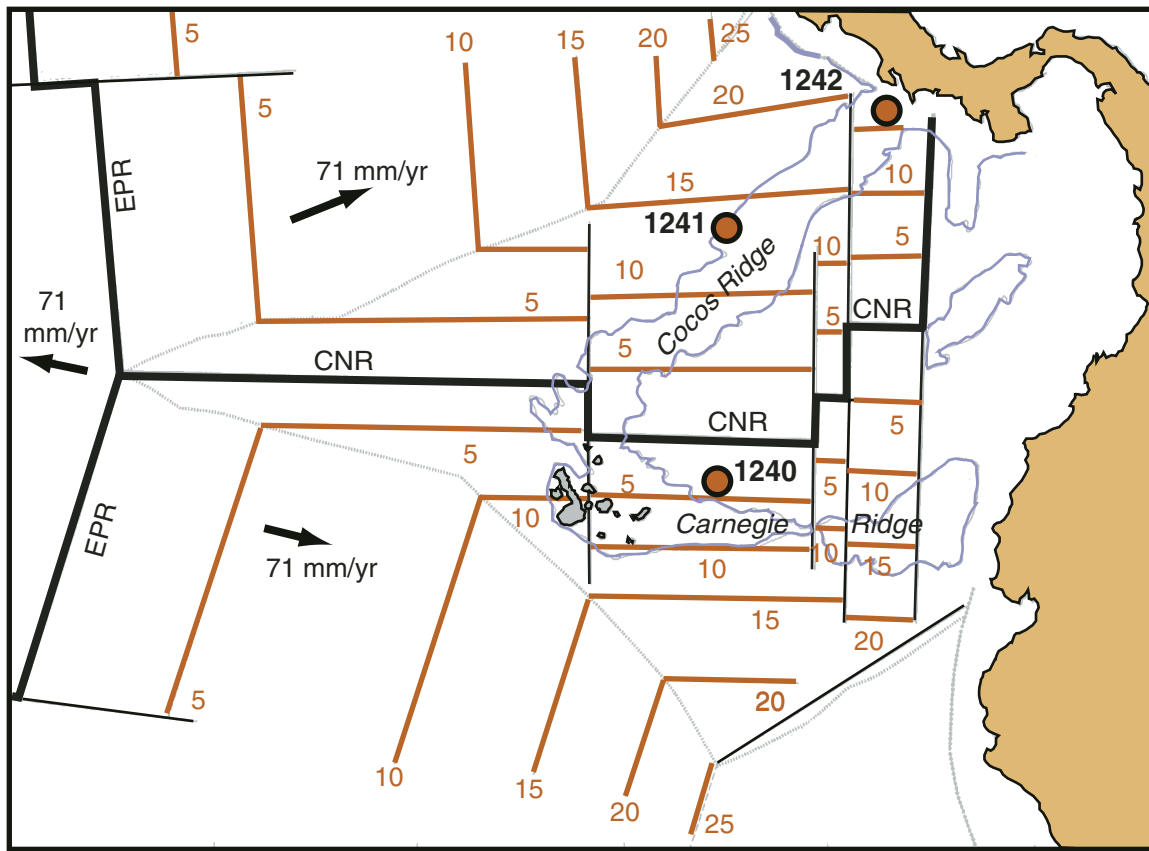


Figure F4. Seismic profile at Site 1241 (*Melville*, NEMO-3, COC-2, line 1, JD144, 23 May 2000; two 150-in³ gas injection guns; Lyle et al., 2000).

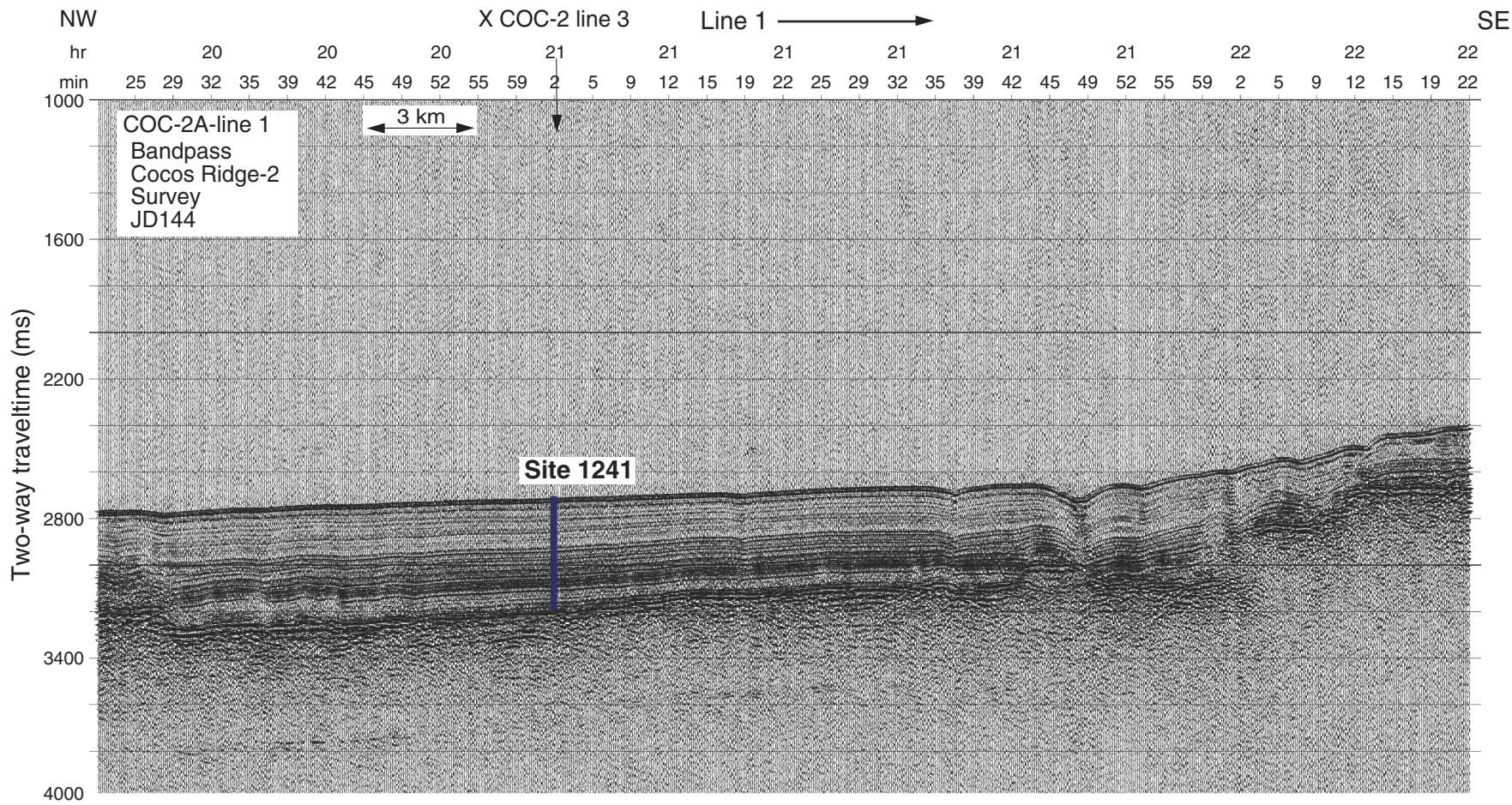


Figure F5. Upper-ocean salinity of the eastern tropical Pacific (annual average) (data from Ocean Climate Laboratory, 1999).

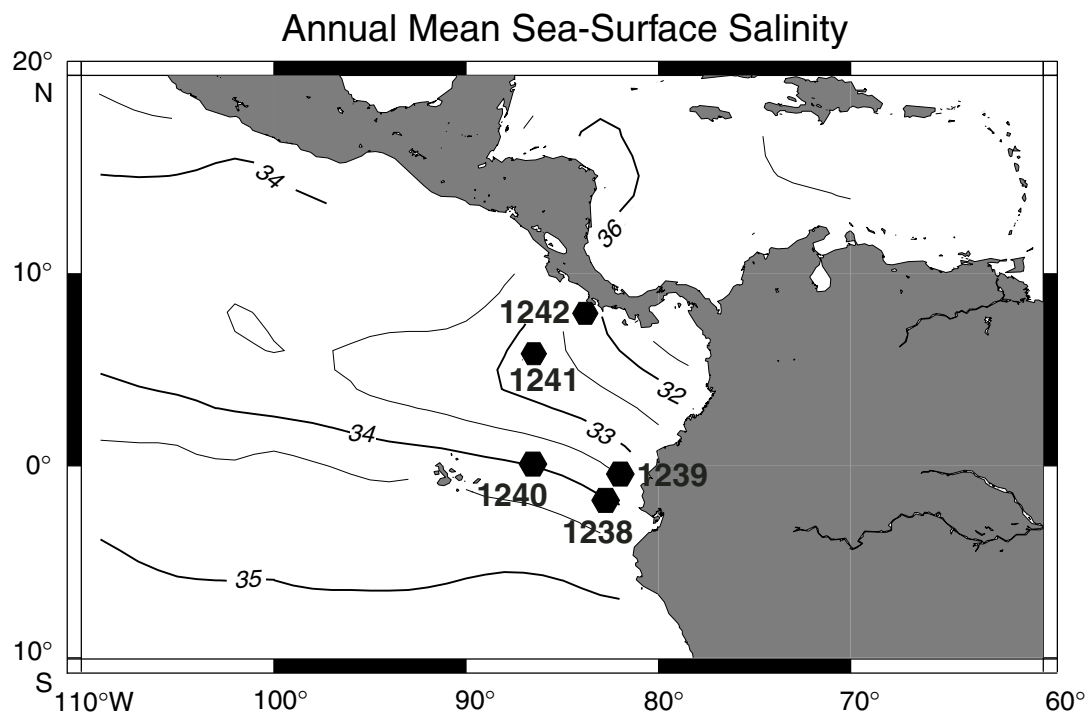


Figure F6. Chlorophyll distributions in surface waters of the equatorial Pacific, based on satellite color data, reveal that Site 1241 is now within the relatively low production regime associated with the North Equatorial Counter Current.

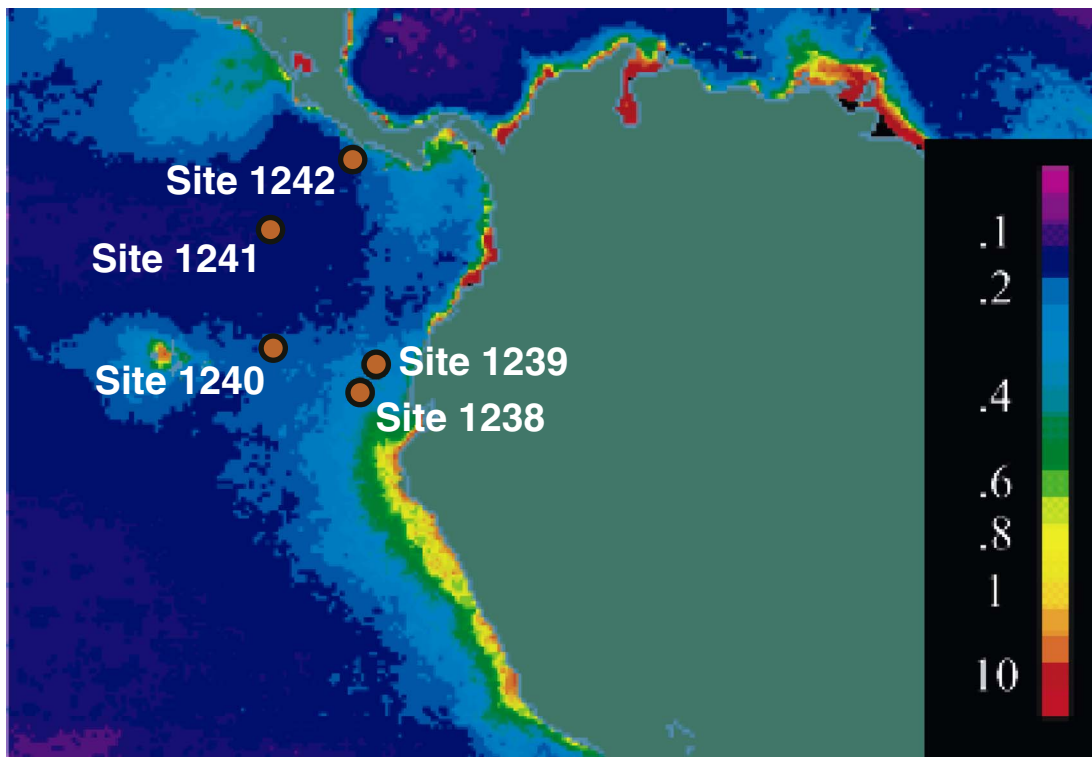


Figure F7. Meridional cross section of water masses, characterized by dissolved oxygen concentrations in the tropical East Pacific (Ocean Climate Laboratory, 1999) and Leg 202 site locations. GUC = Gunther Undercurrent, EUC = Equatorial Undercurrent, NPIW = North Pacific Intermediate Water, PCW = Pacific Central Water, PBW = Peru Basin Water. The relatively low oxygen content of water in the Guatemala Basin reflects the water's sources in PCW, relative isolation of water masses within the deep Guatemala Basin, and high organic rain on the Central American margin.

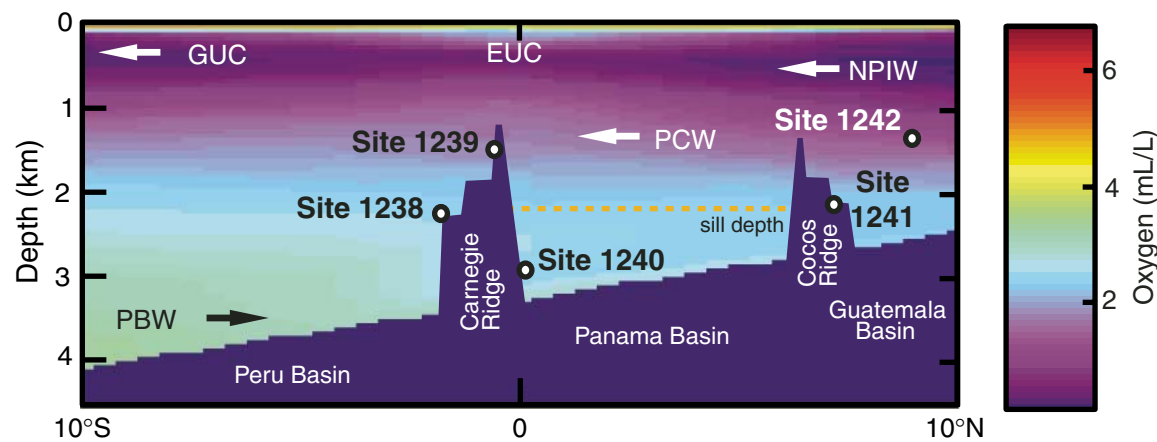


Figure F8. Modern annual-average properties of the upper ocean at paleolocations of Site 1241, based on plate tectonic backtracking and an assumption of no temporal changes in regional oceanic properties. Atlas data on physical and chemical properties are from WOA98 (Ocean Climate Laboratory, 1999). Primary productivity (PP) is from satellite measurements of sea-surface color (Behrenfeld et al., 2001). Pycnocline depth is calculated to the nearest 5 m, based on the shallowest maximum in the vertical density gradient. Symbols are average values extracted from the nearest 1° latitude-longitude box in each atlas. Lines = smoothed trends of each property along the backtrack path. SST = sea-surface temperature, SSS = sea-surface salinity.

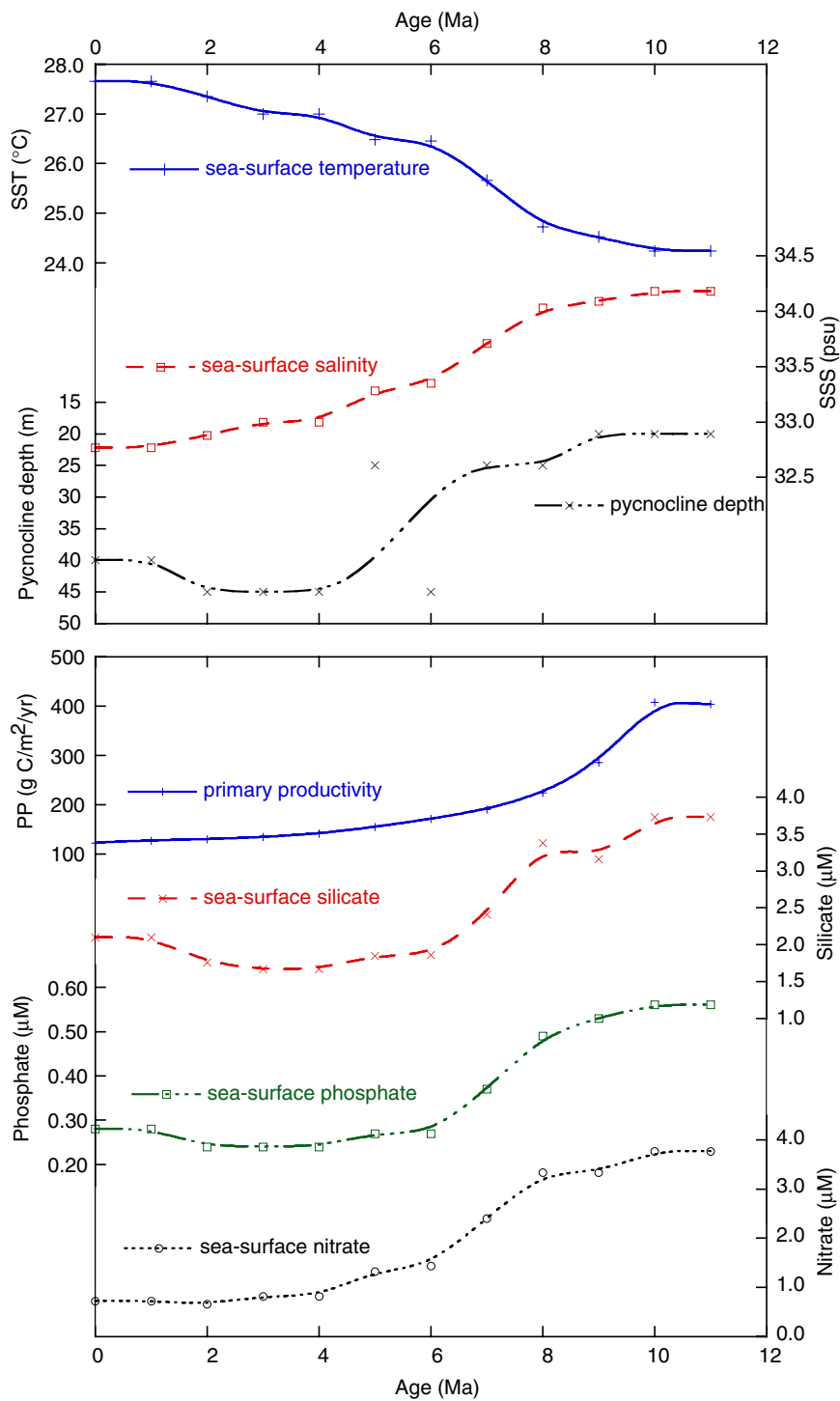


Figure F9. Magnetic susceptibility data (MST-MS) vs. mcd for the spliced record and Holes 1241A (black), 1241B (red), and 1241C (green). Gray boxes indicate the portions of cores that are in the splice. A. 0–40 mcd. B. 30–70 mcd. (Continued on next six pages.)

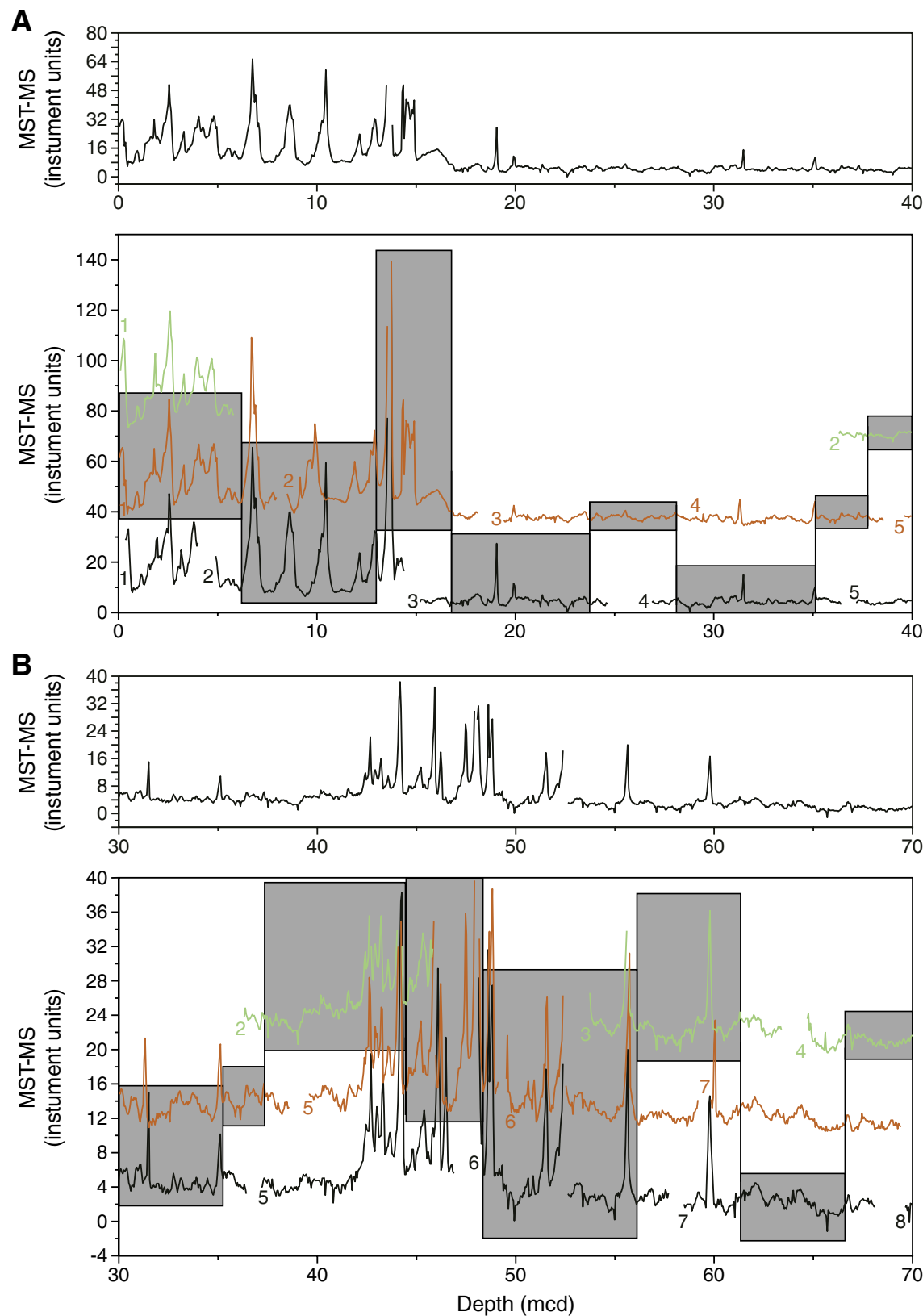


Figure F9 (continued). C. 60–100 mcd. D. 90–130 mcd.

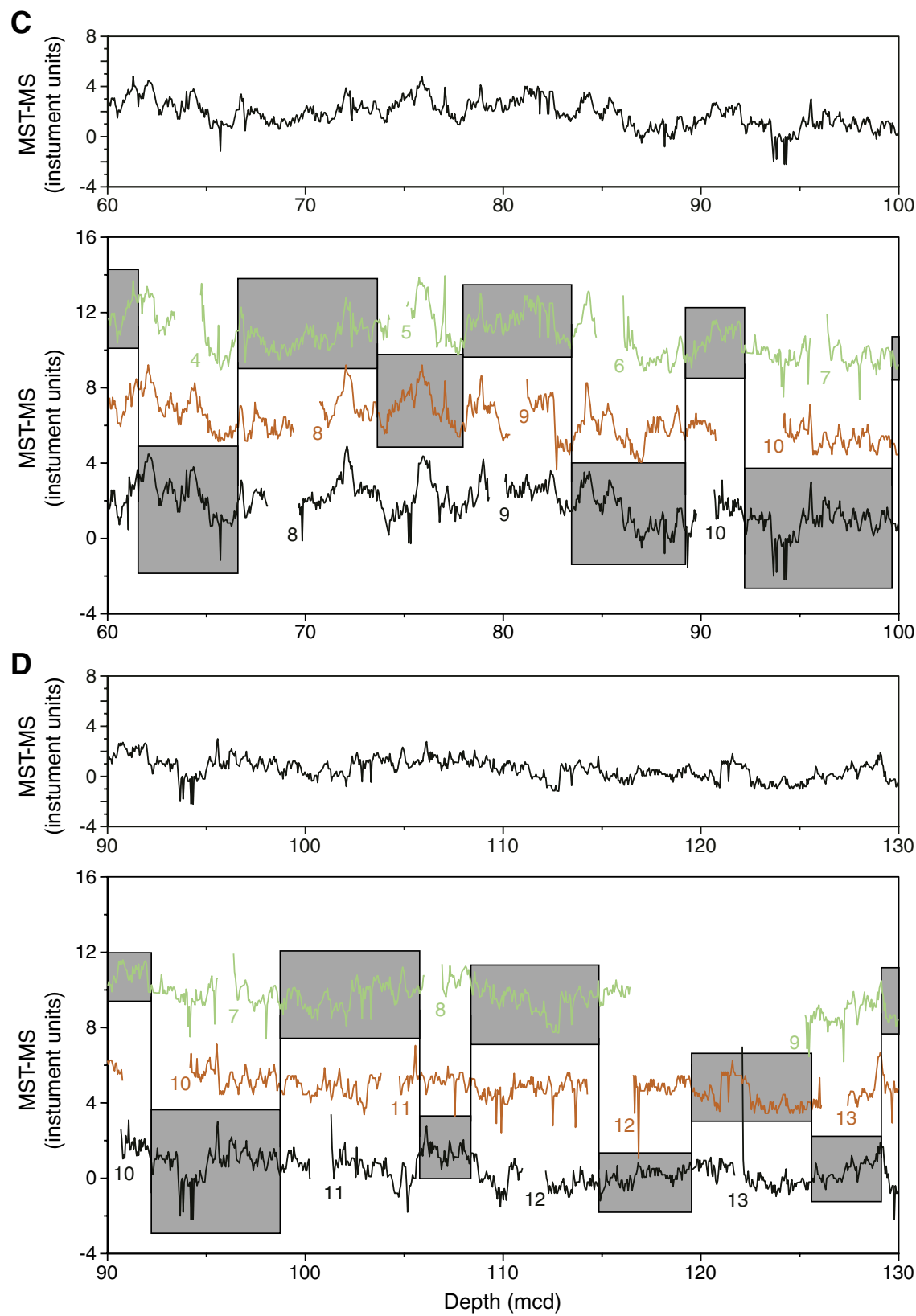


Figure F9 (continued). E. 120–160 mcd. F. 150–190 mcd.

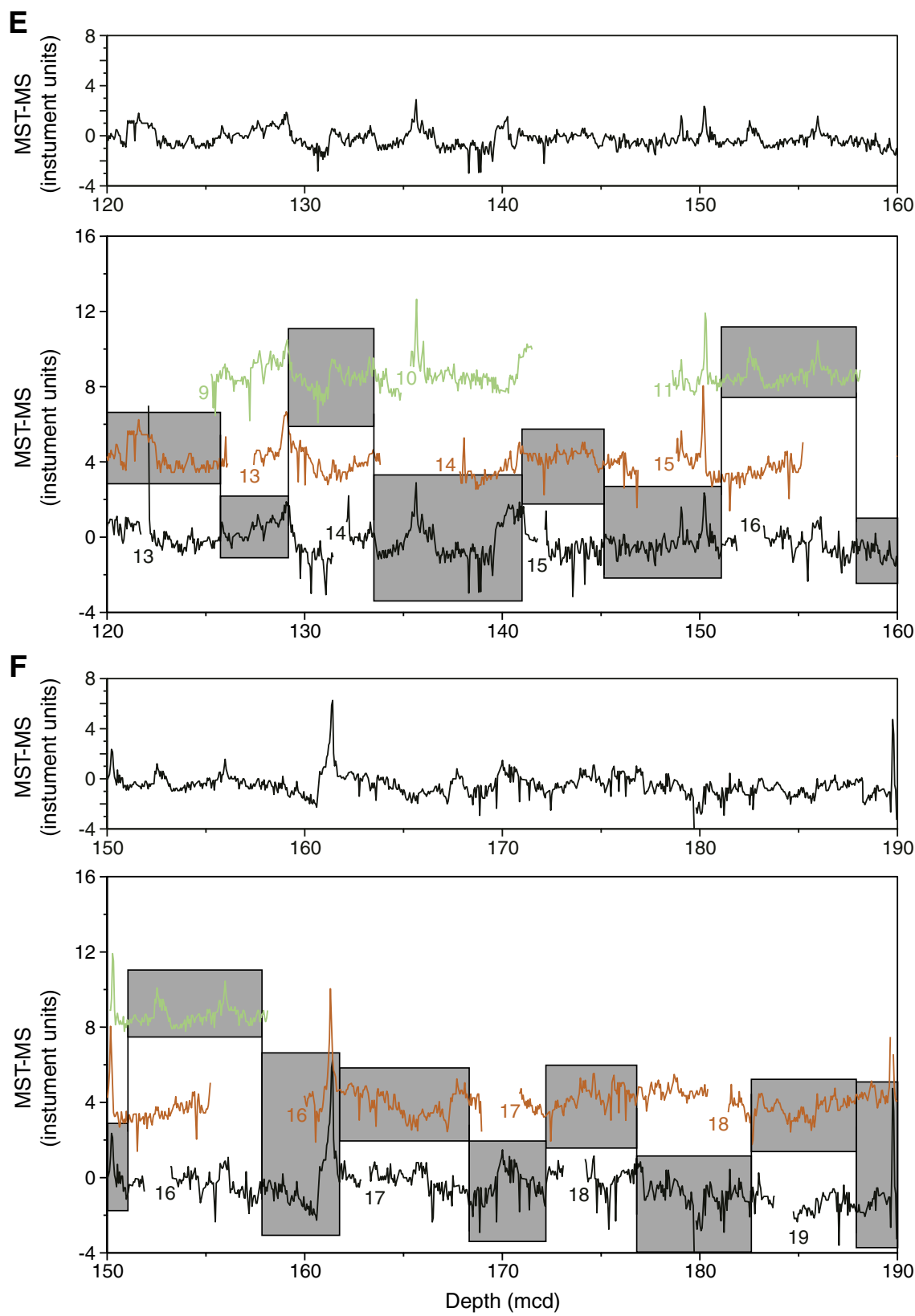


Figure F9 (continued). G. 180–220 mcd. H. 210–250 mcd.

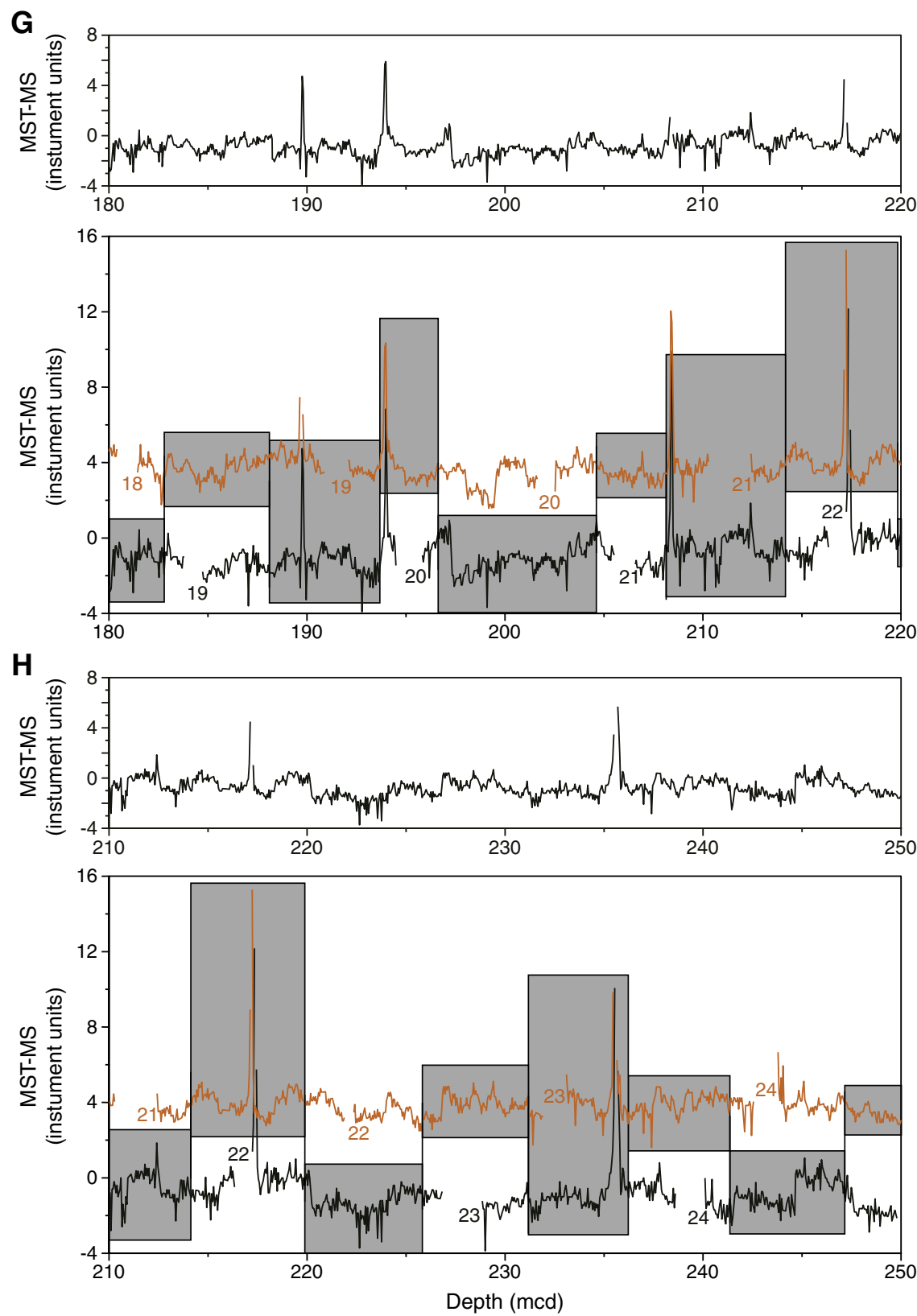


Figure F9 (continued). I. 240–280 mcd. J. 270–310 mcd.

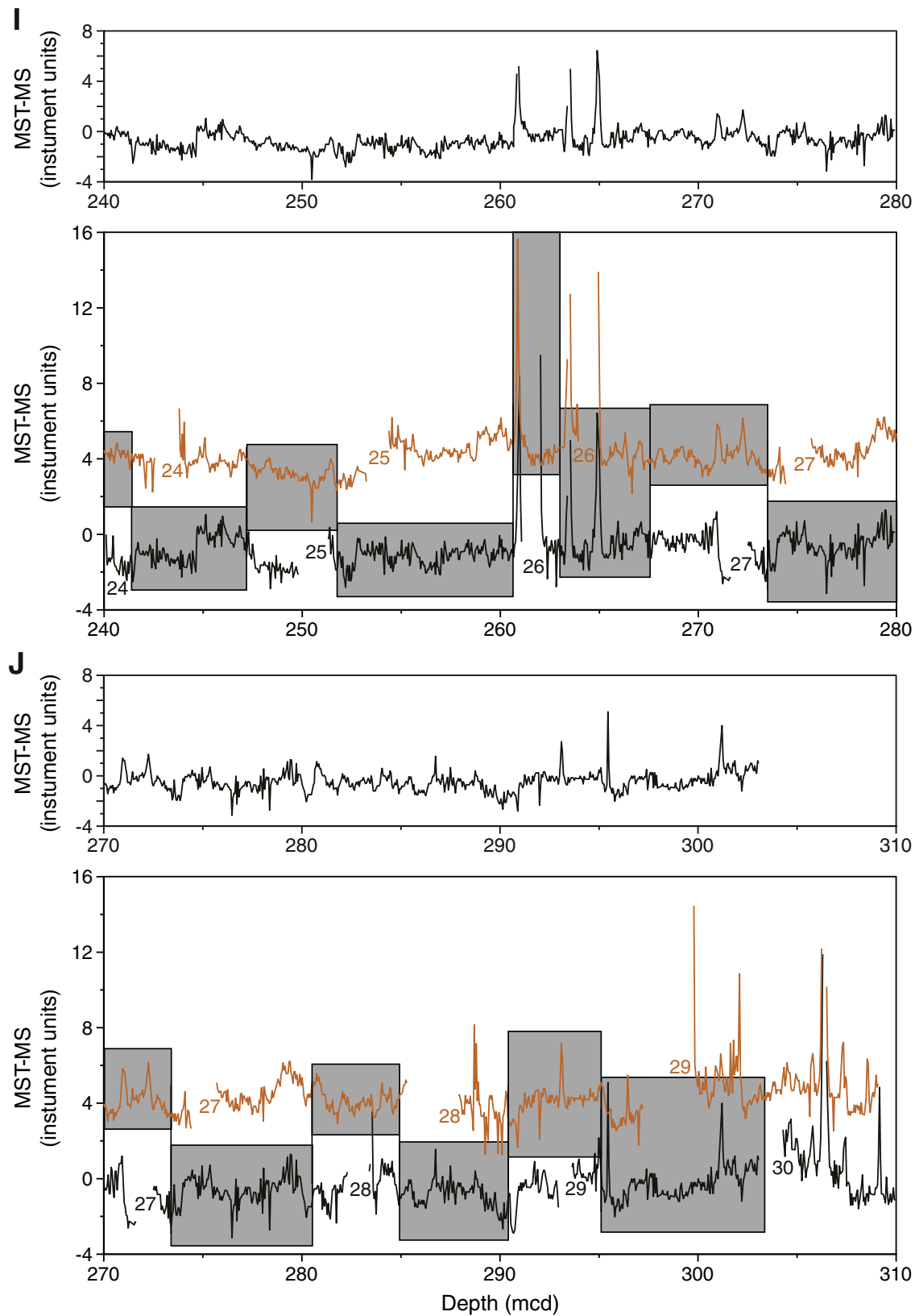


Figure F9 (continued). K. 300–340 mcd. L. 330–370 mcd.

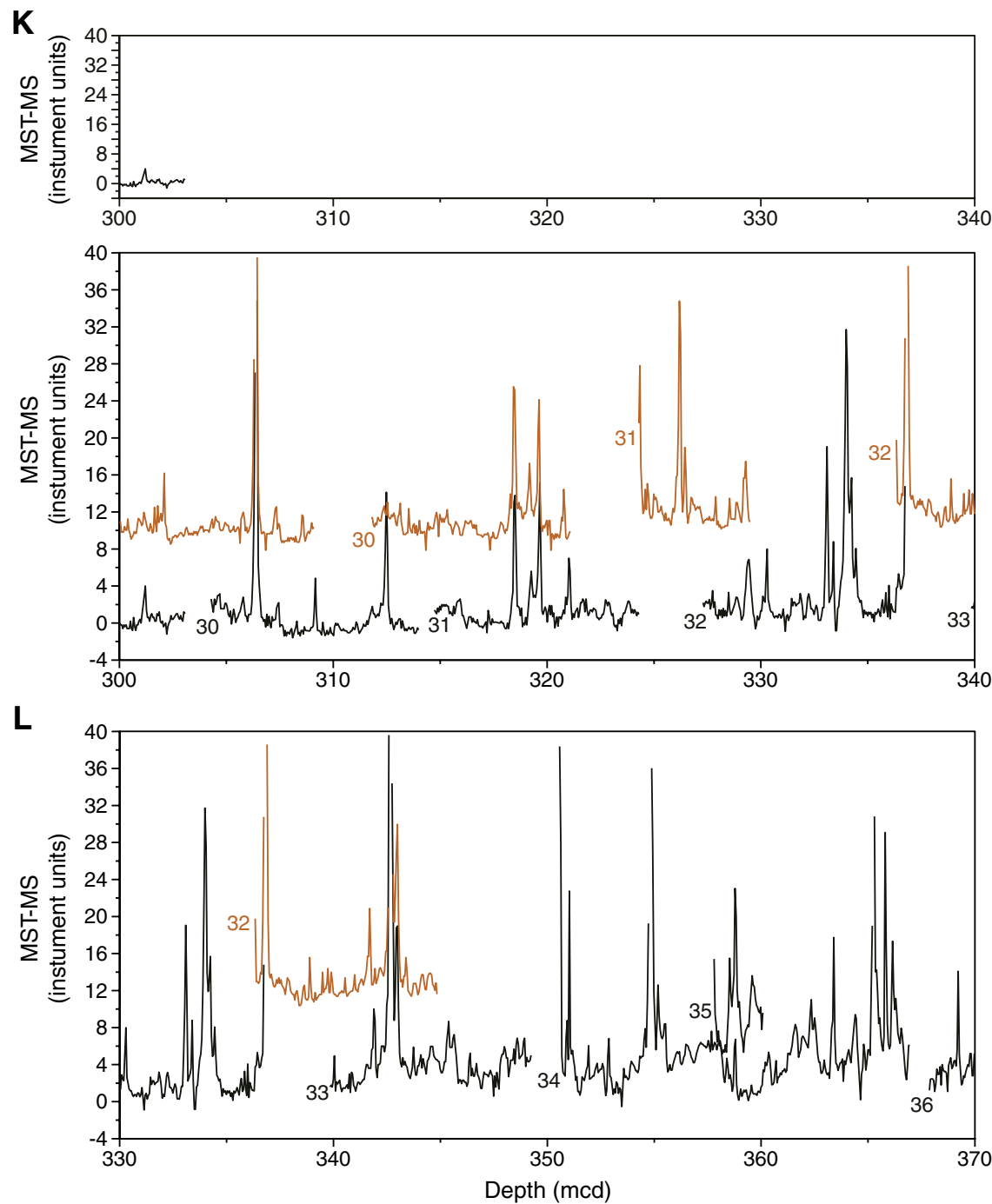


Figure F9 (continued). M. 360–400 mcd. N. 390–430 mcd. O. 420–460 mcd.

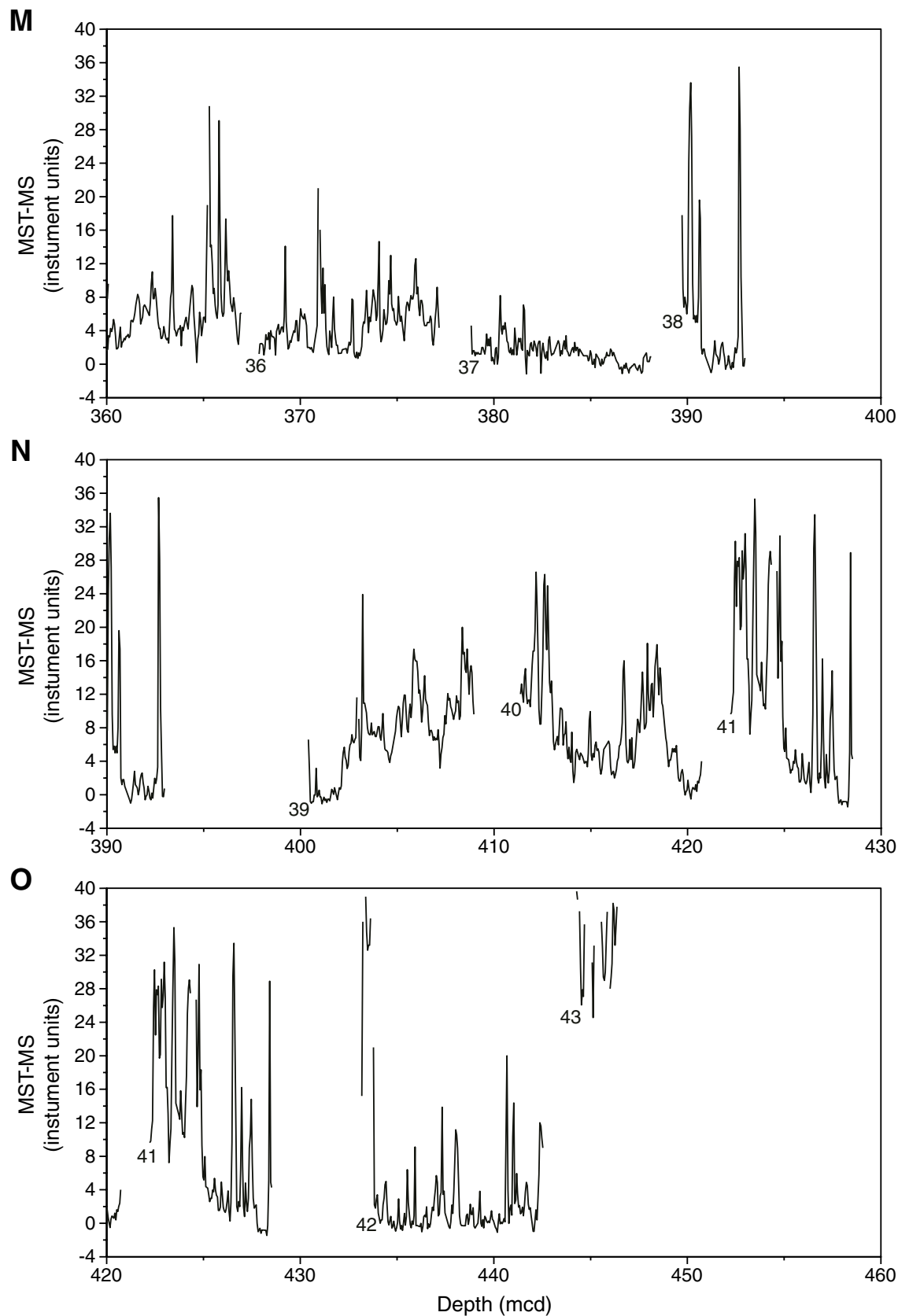


Figure F10. Gamma ray attenuation (GRA) bulk density data vs. mcd for the spliced record and Holes 1241A (black), 1241B (red), and 1241C (green). Gray boxes indicate the portions of cores that are in the splice. A. 0–40 mcd. B. 30–70 mcd. (Continued on next six pages).

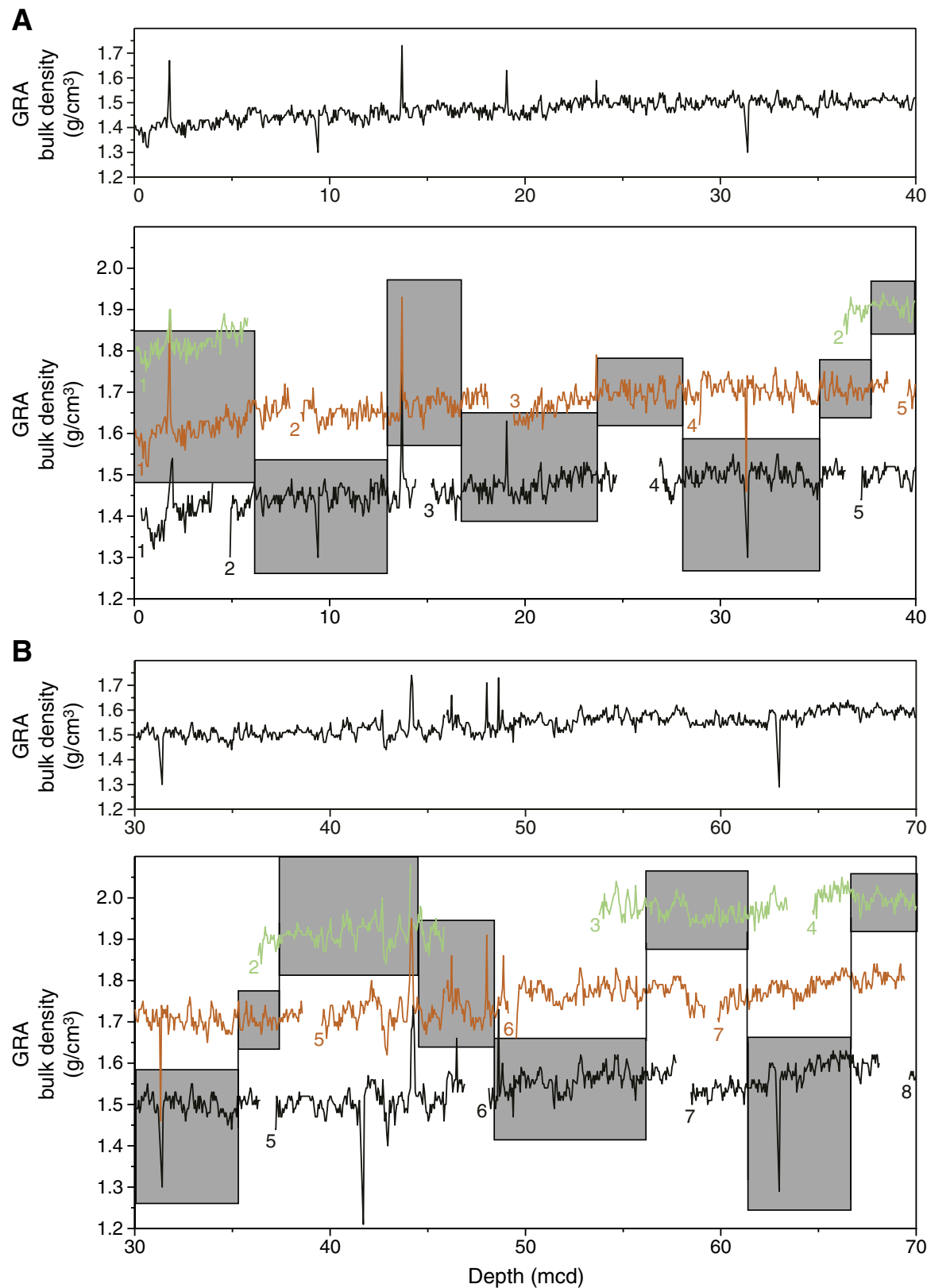
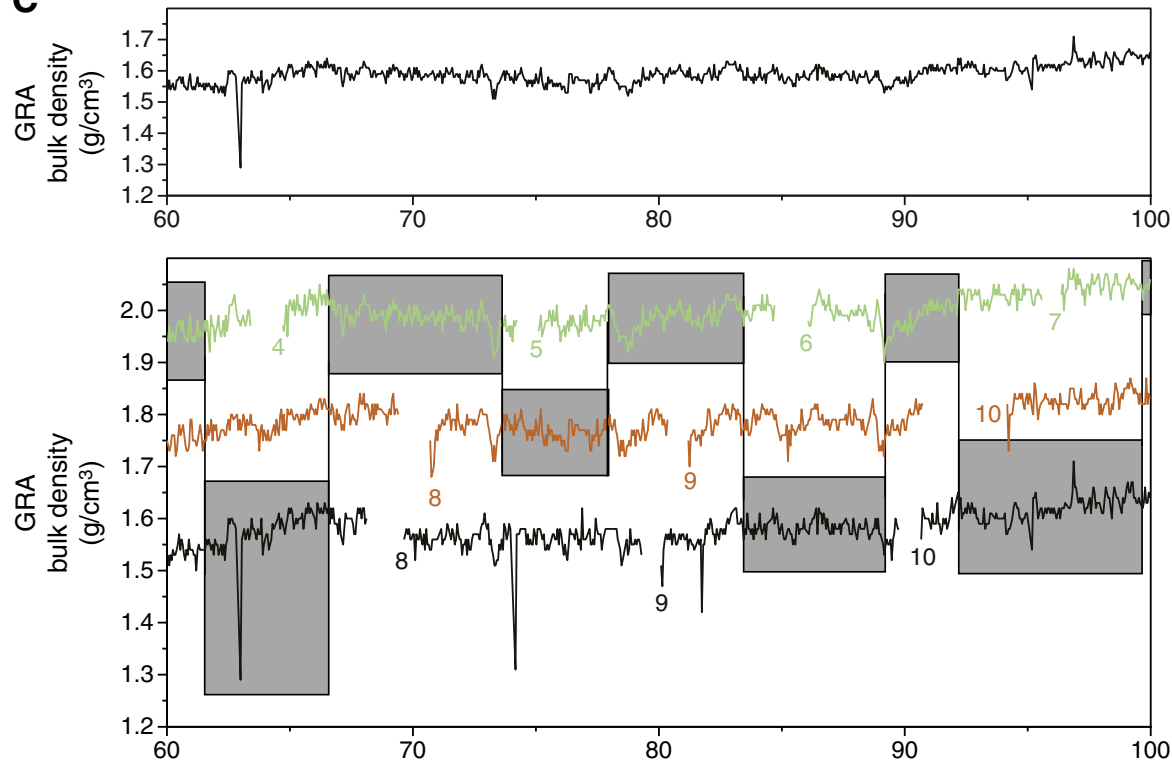


Figure F10 (continued). C. 60–100 mcd. D. 90–130 mcd.

C



D

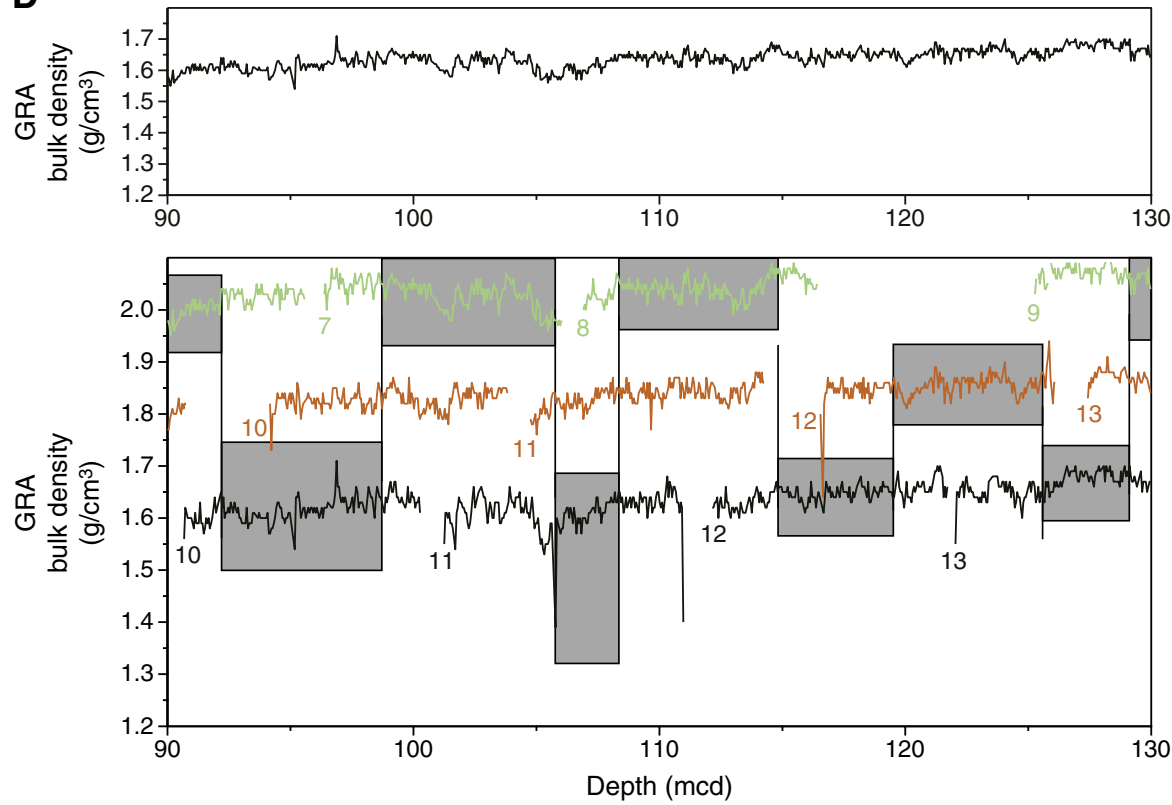
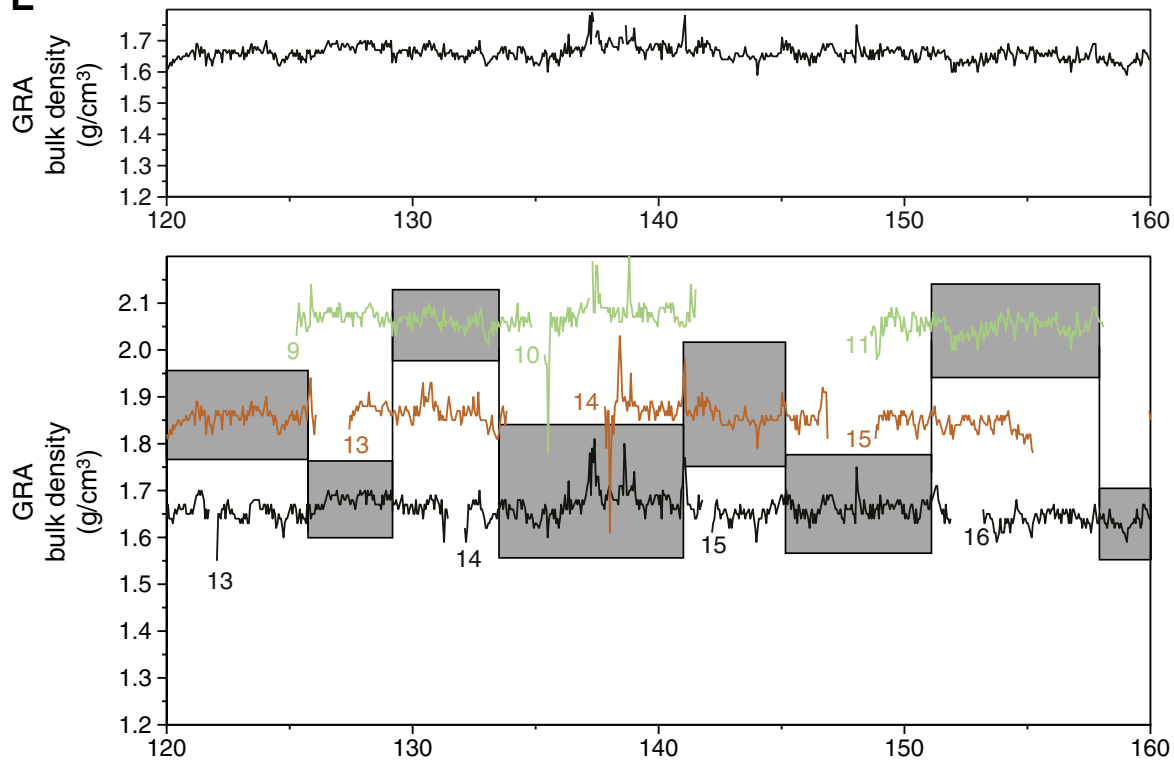


Figure F10 (continued). E. 120–160 mcd. F. 150–190 mcd.

E



F

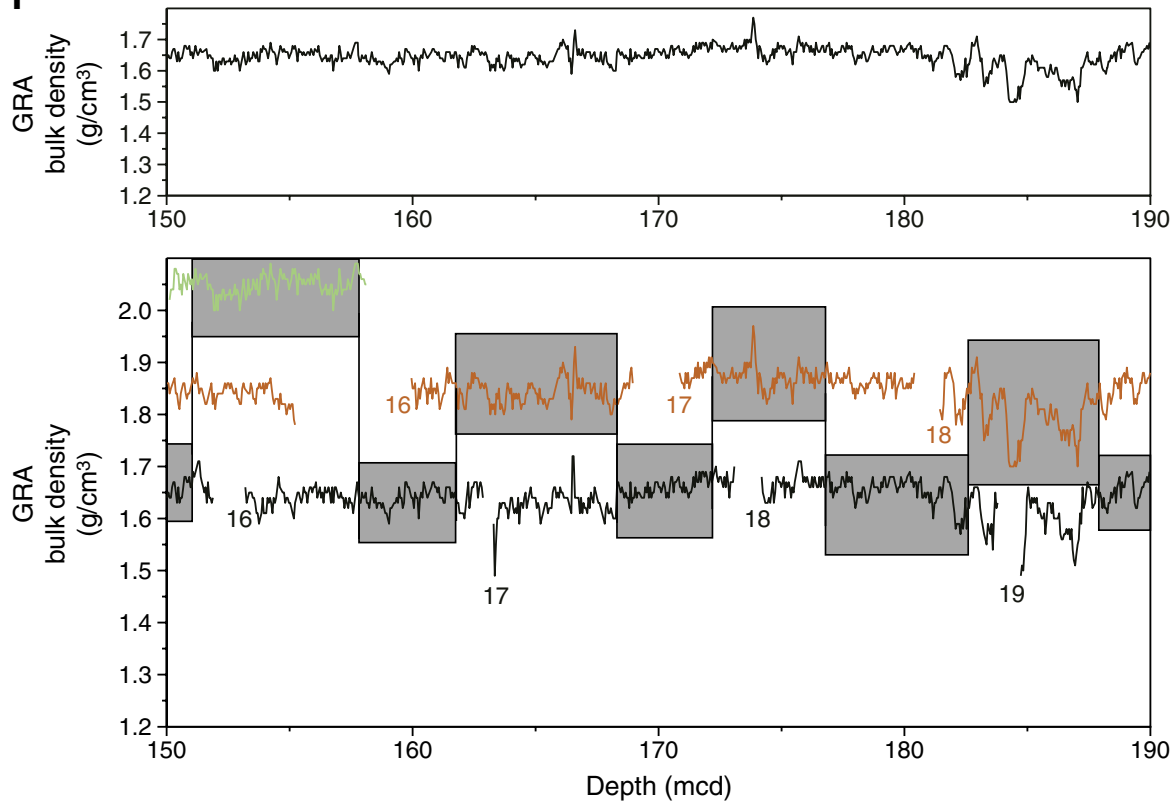


Figure F10 (continued). G. 180–220 mcd. H. 210–250 mcd.

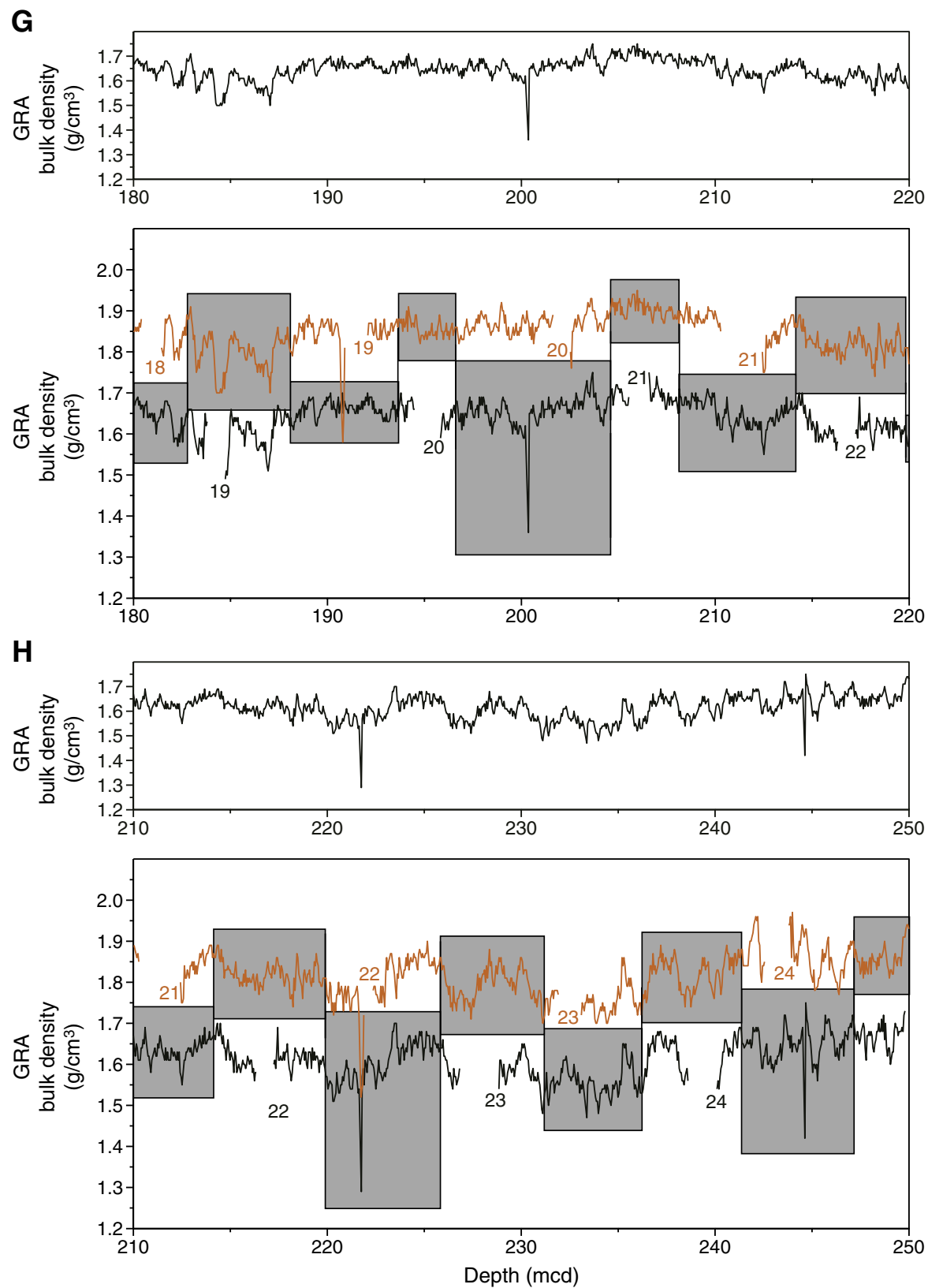


Figure F10 (continued). I. 240–280 mcd. J. 270–310 mcd.

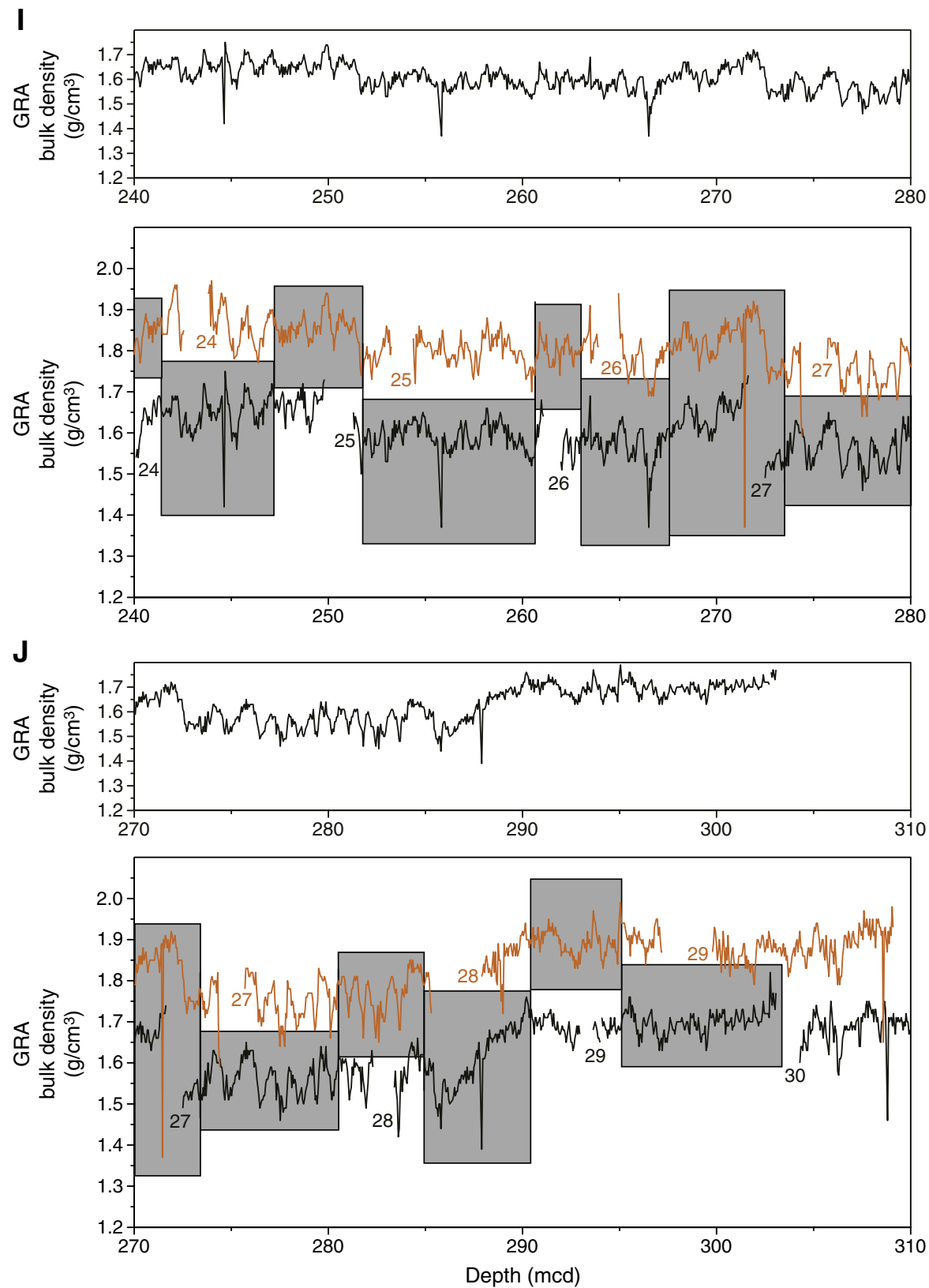


Figure F10 (continued). K. 300–340 mcd. L. 330–370 mcd.

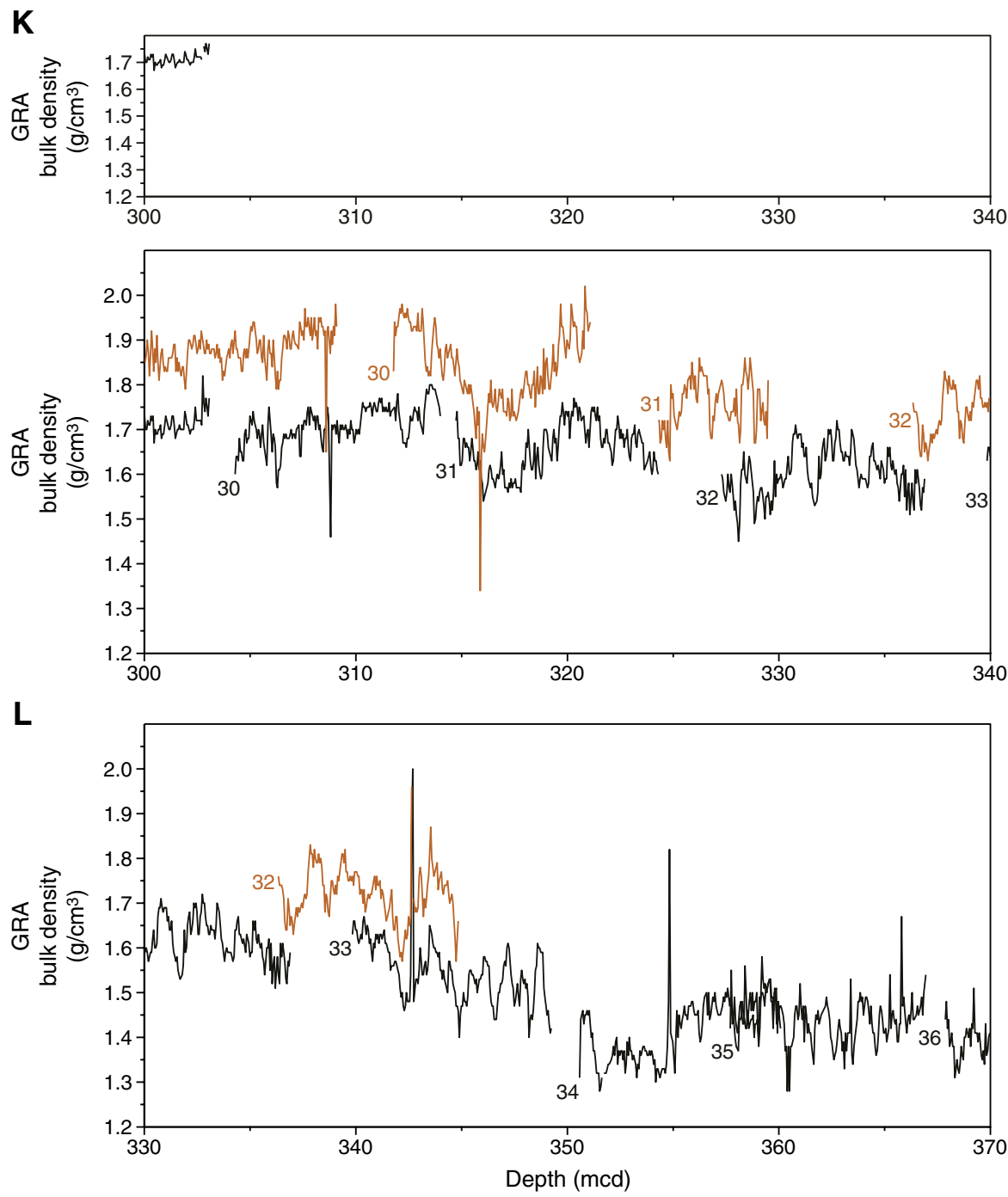


Figure F10 (continued). M. 360–400 mcd. N. 390–430 mcd. O. 420–460 mcd.

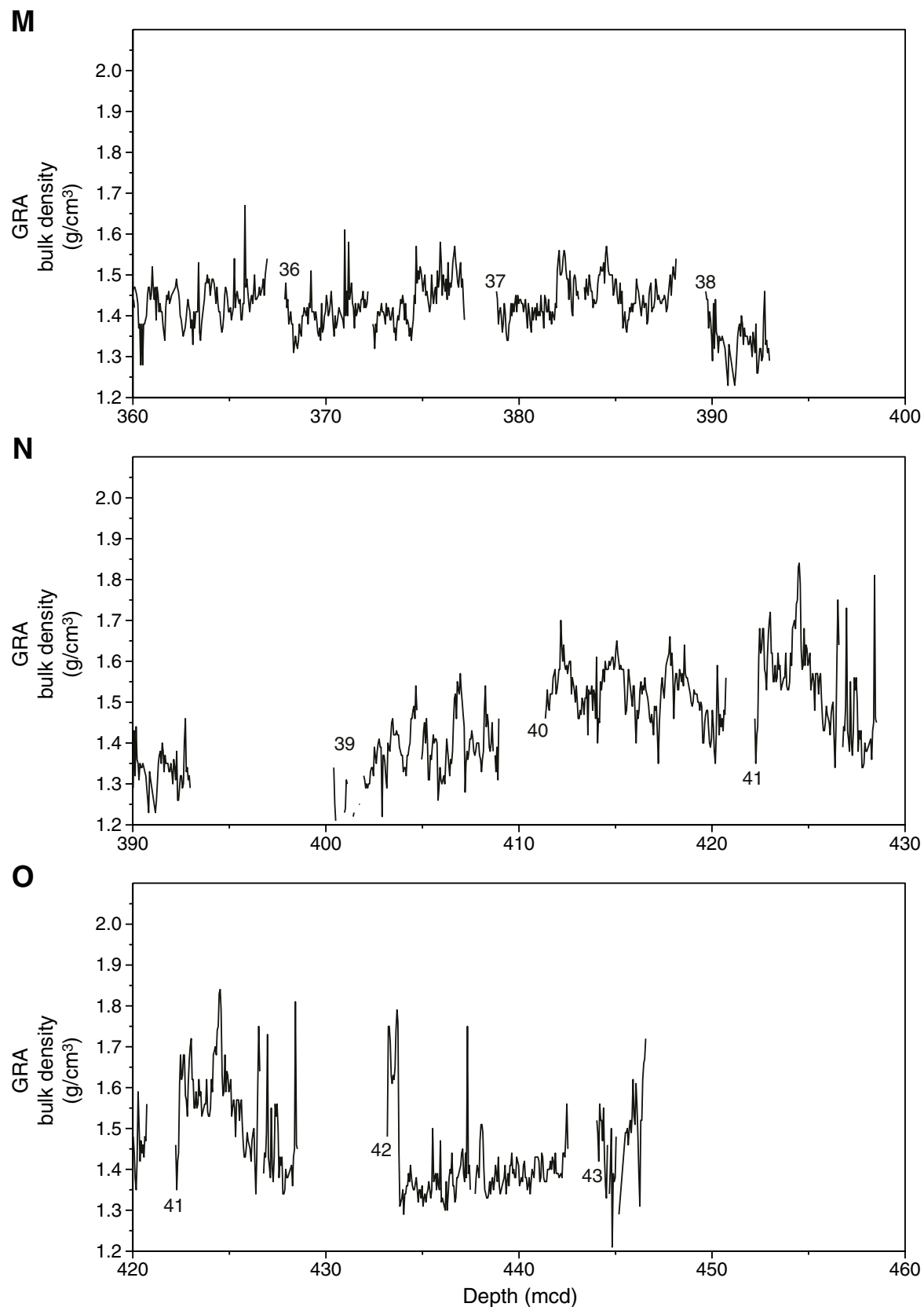


Figure F11. Smoothed (9-point Gaussian) spliced records of natural gamma radiation (NGR), gamma ray attenuation (GRA) bulk density, and magnetic susceptibility (MST-MS) from Site 1241. Below ~155 mcd, NGR data in Hole 1241A were near ambient background levels. NGR was not measured in Holes 1241B and 1241C at depths >155 mcd.

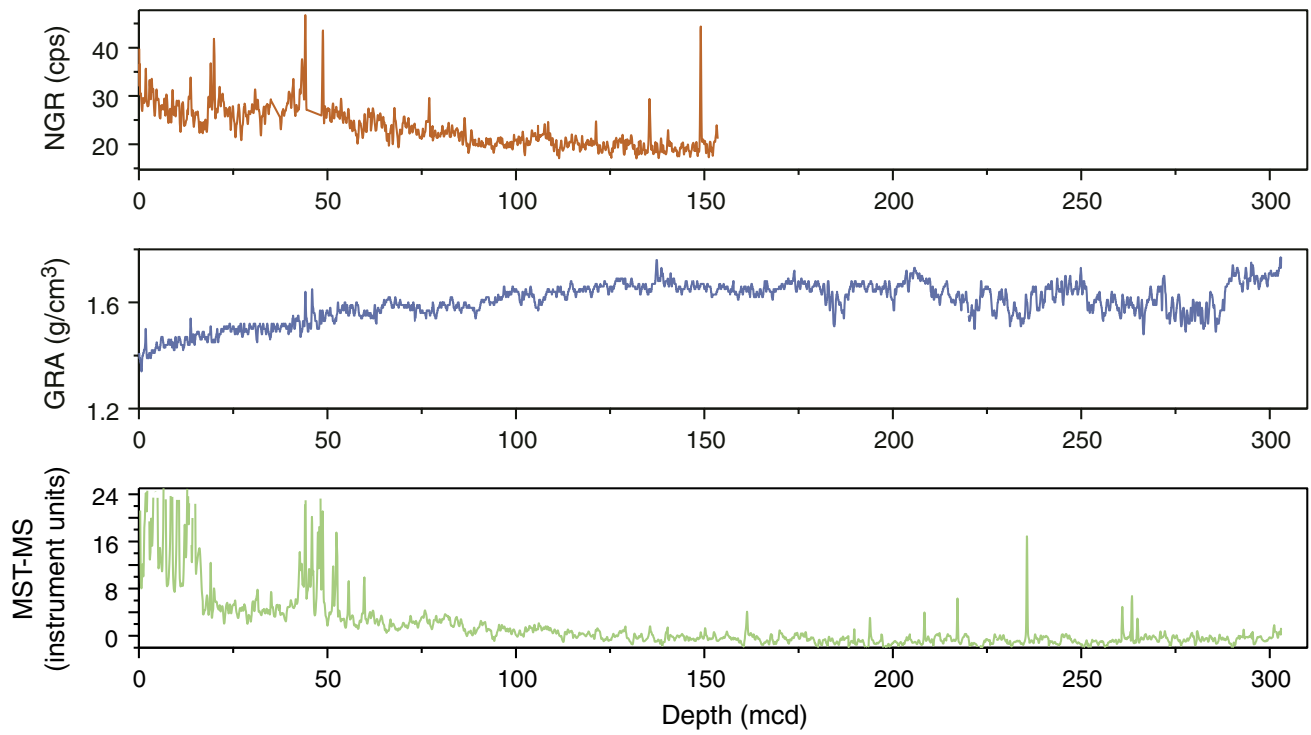


Figure F12. Smoothed (9-point Gaussian) spliced records of color reflectance from Site 1241: L*, a*, and b*.

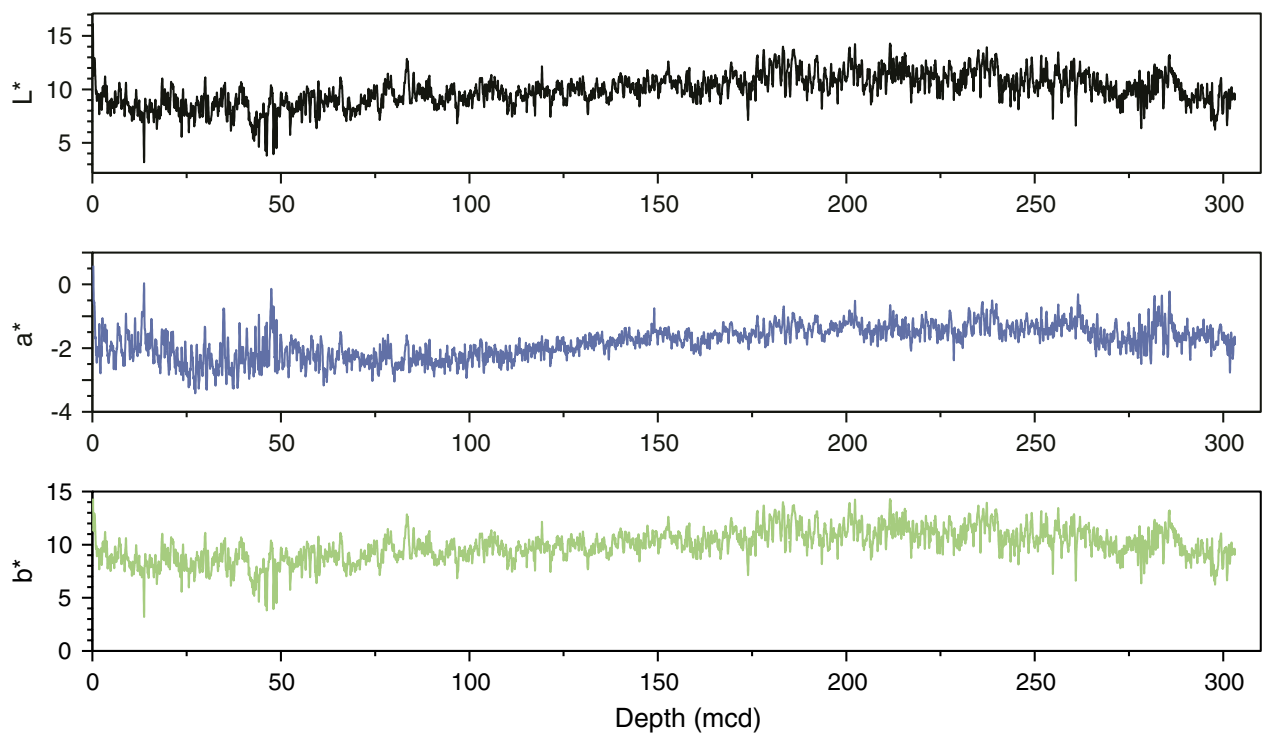


Figure F13. A comparison of the drillers depth (mbsf) and meters composite depth (mcd) scales in Holes 1241A through 1241C. On average, mcd is 13% greater than mbsf. The 1:1 (mbsf:mcd) line is also shown for comparison. GF = growth factor. The gray box shows the range of the splice.

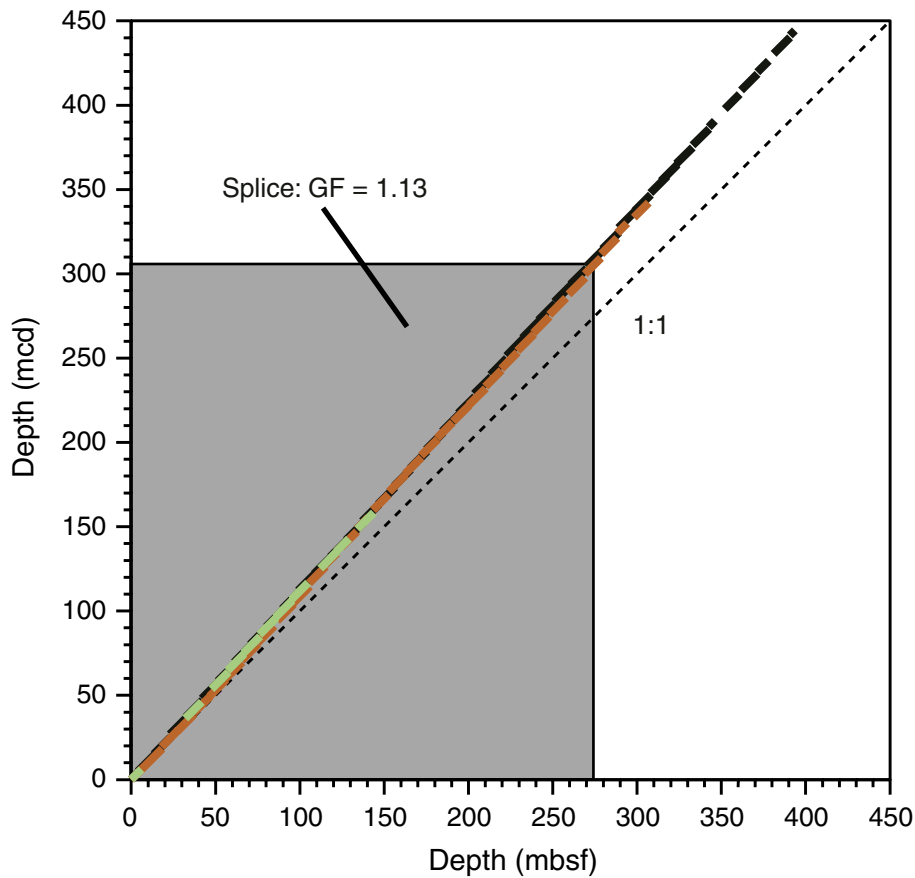


Figure F14. Core recovery, lithostratigraphic subunit, age, magnetic susceptibility, gamma ray attenuation (GRA) bulk density, natural gamma radiation (NGR), lightness (L^*), carbonate, and total organic carbon (TOC) of sediments recovered from Site 1241. Gray lines = original data, black lines = 50-point smoothing averages of the original data.

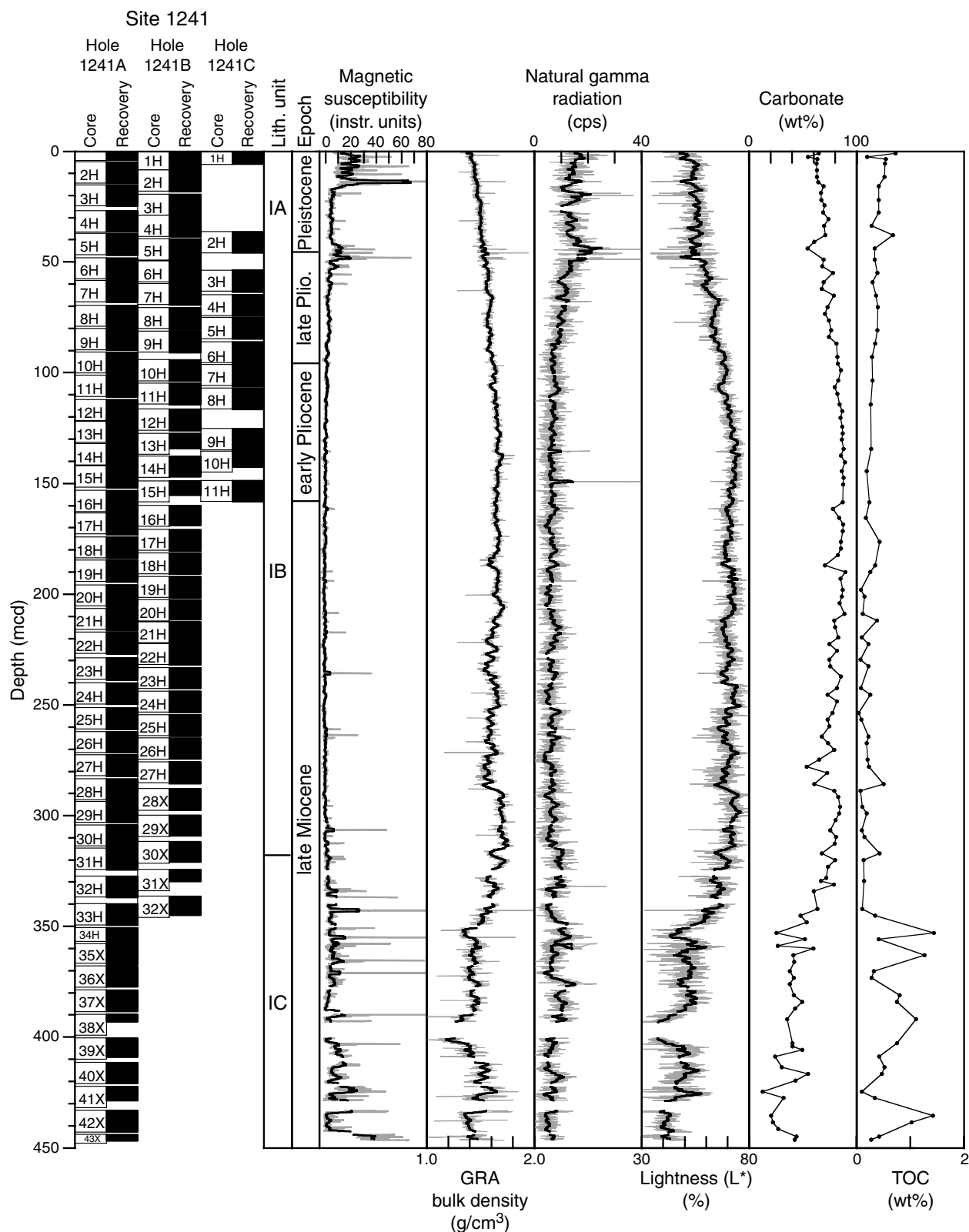


Figure F15. Major siliciclastic, biogenic, and authigenic components observed in Hole 1241A smear slides. Rad. = radiolarians, Silicof. = silicoflagellates.

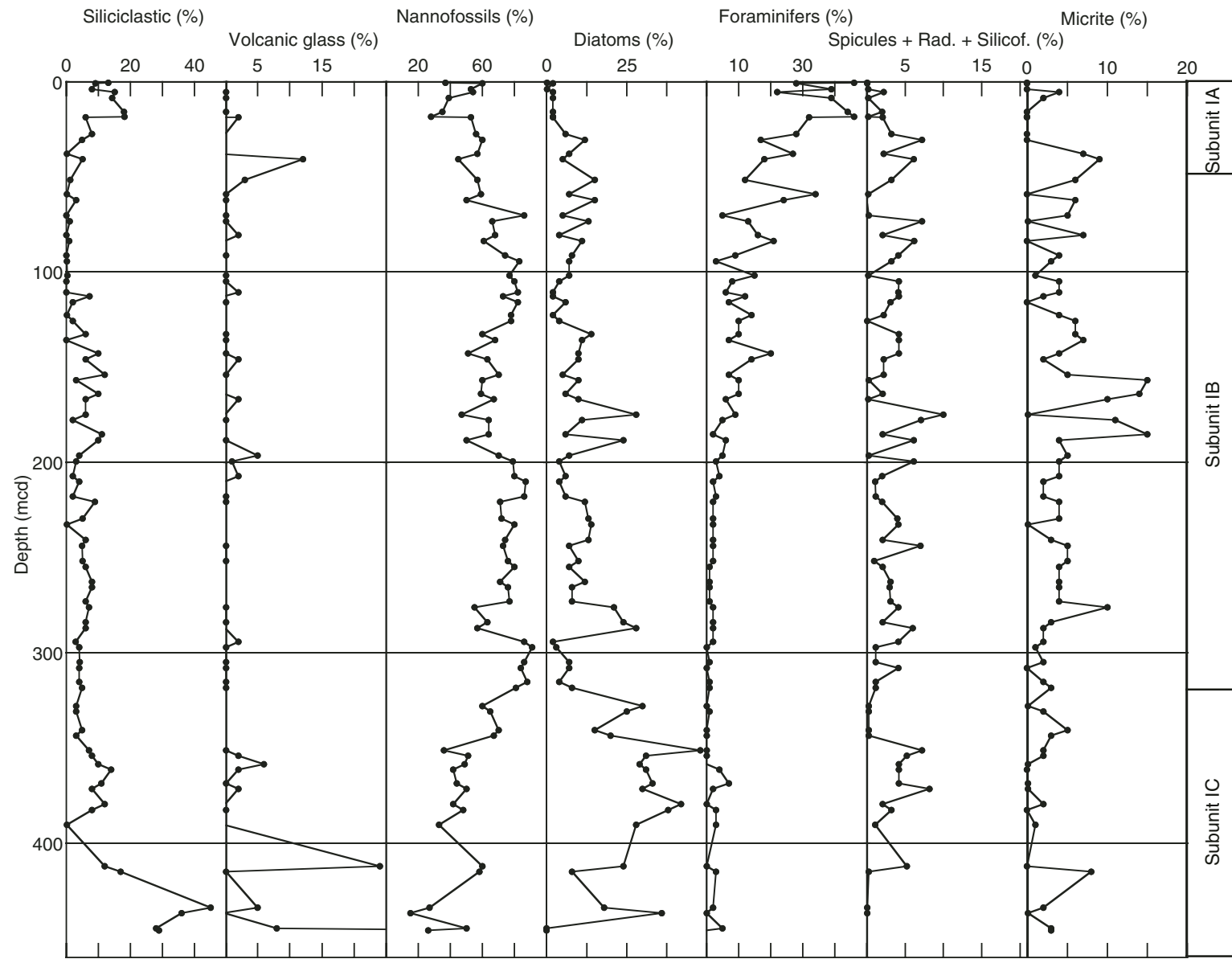


Figure F16. Physical properties measurements for Site 1241. A. Gamma ray attenuation (GRA) bulk density and moisture and density (MAD) bulk density. B. Porosity. C. Grain density. D. Correlation between interpolated GRA and discrete MAD bulk density measurements. E. Correlation between MAD bulk density and porosity. F. Correlation between carbonate and grain density.

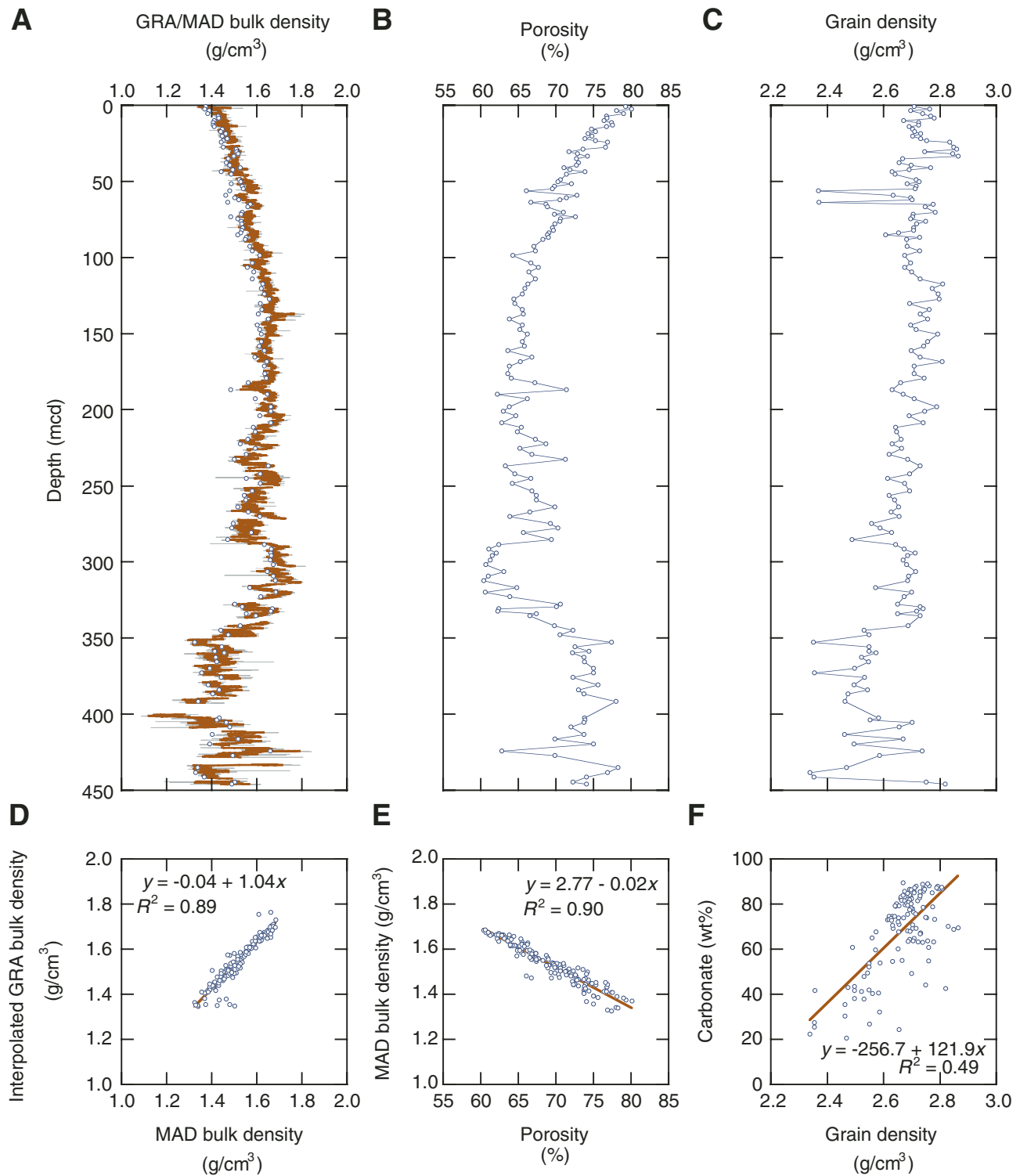


Figure F17. Color measurements at Site 1241 plotted in the a^*-b^* color plane.

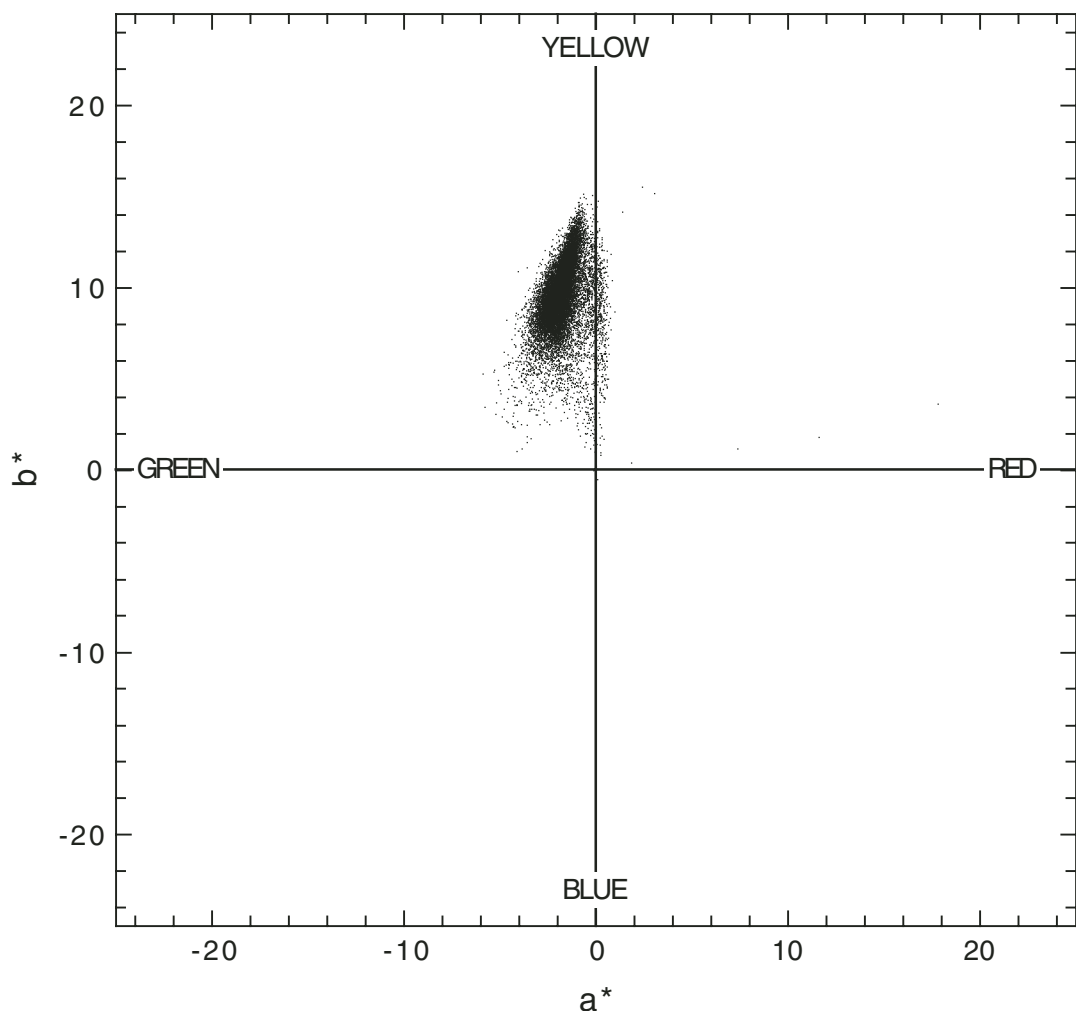


Figure F18. A. Sequential depth plots of raw reflectance data for Site 1241. B. First derivatives for Site 1240. Red lines = absorption features typical of organic pigments (i.e., 410 and 650 nm). C. The depth of the absorption feature at 650 nm, estimated relative to 630 and 700 nm and normalized to a measure of the general slope of the spectrum, is plotted with depth as a proxy for chlorin abundance.

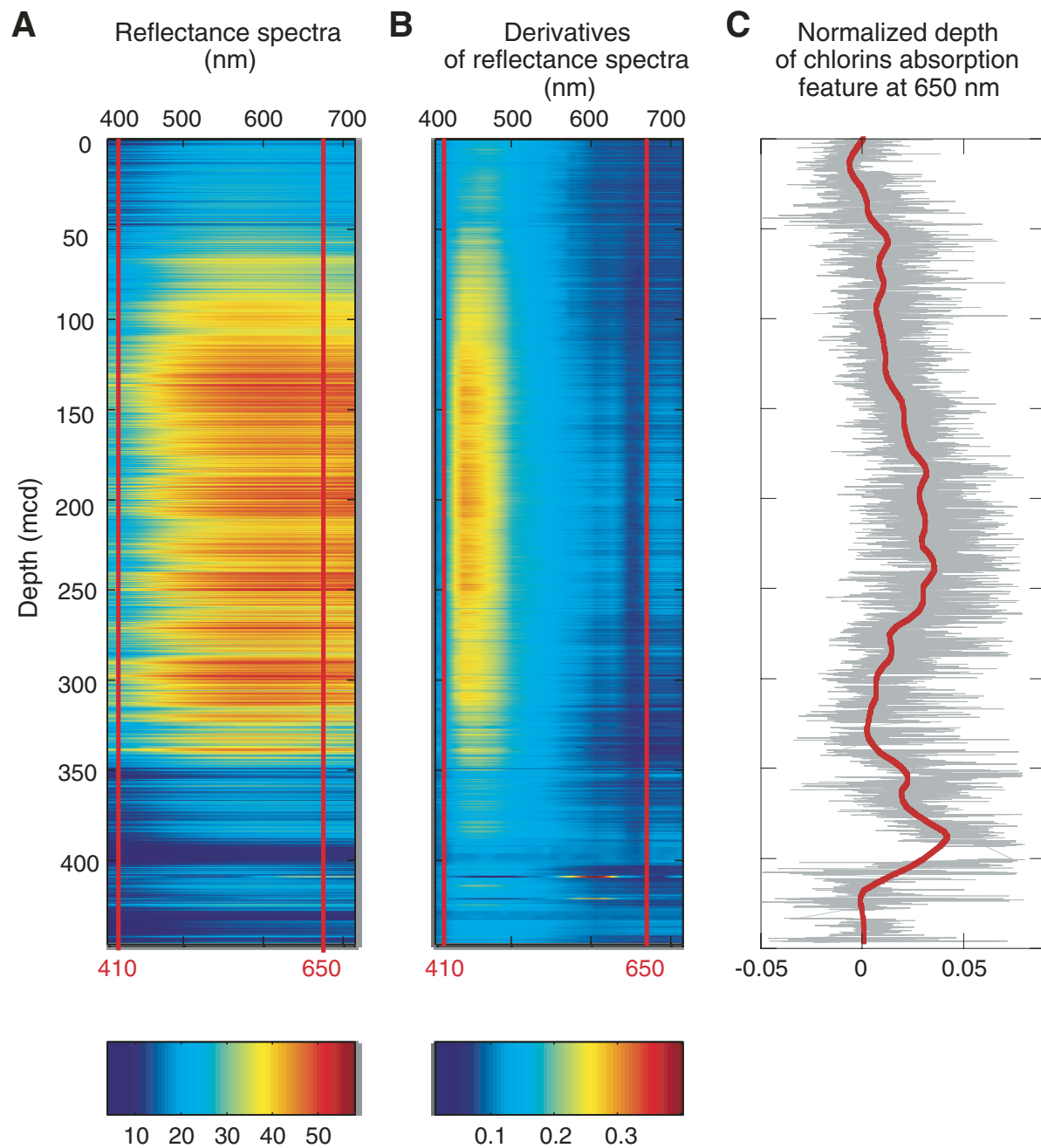


Figure F19. Close-up photograph of dark and light color variability in Subunit IA (interval 202-1241A-4H-6, 68–90 cm).

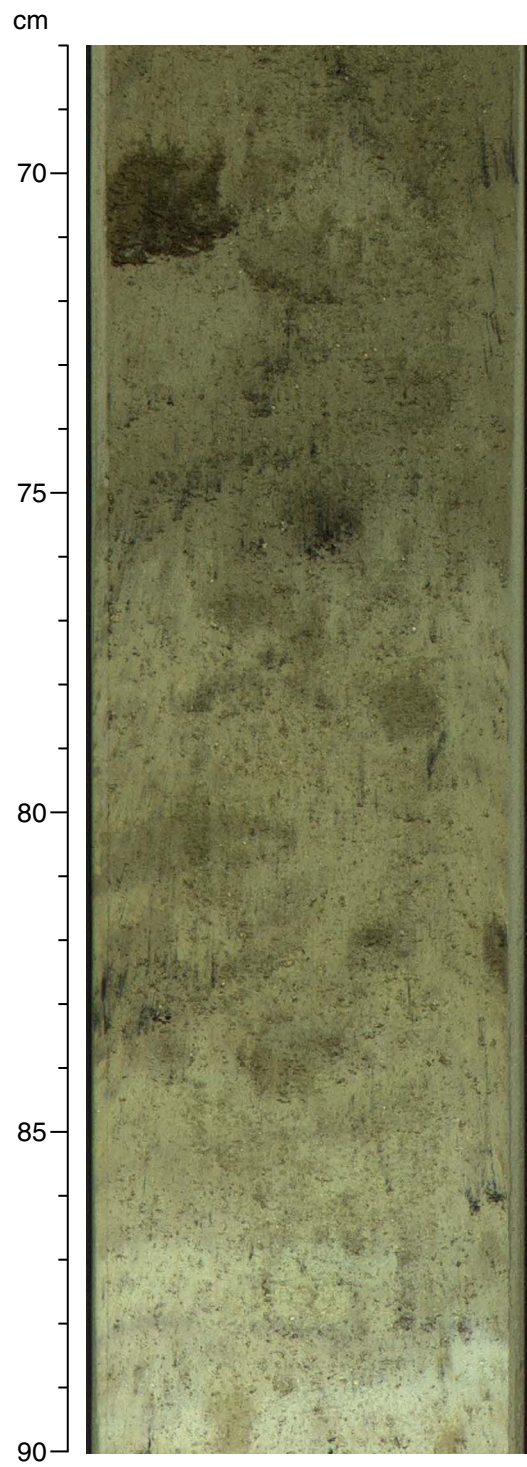


Figure F20. Close-up photograph of a representative lapilli layer found at Site 1241 (interval 202-1241A-5H-5, 8-20 cm).

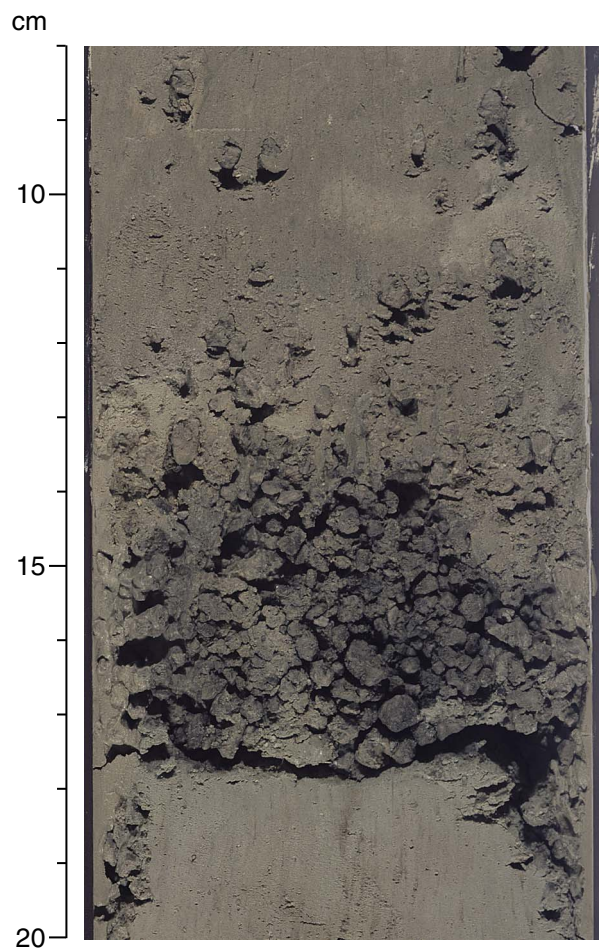


Figure F21. Close-up photograph of laminated diatom ooze (interval 202-1241-40X-7, 0–20 cm).

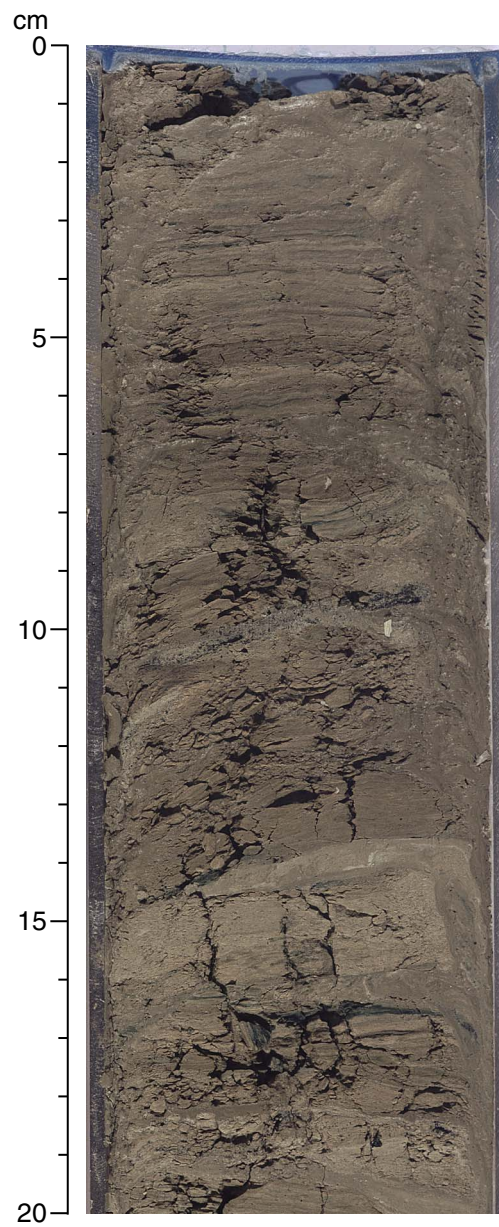


Figure F22. Downhole distribution of volcaniclastic horizons at Site 1241. **A.** Horizons with predominantly clear glass. **B.** Horizons with predominantly brown glass.

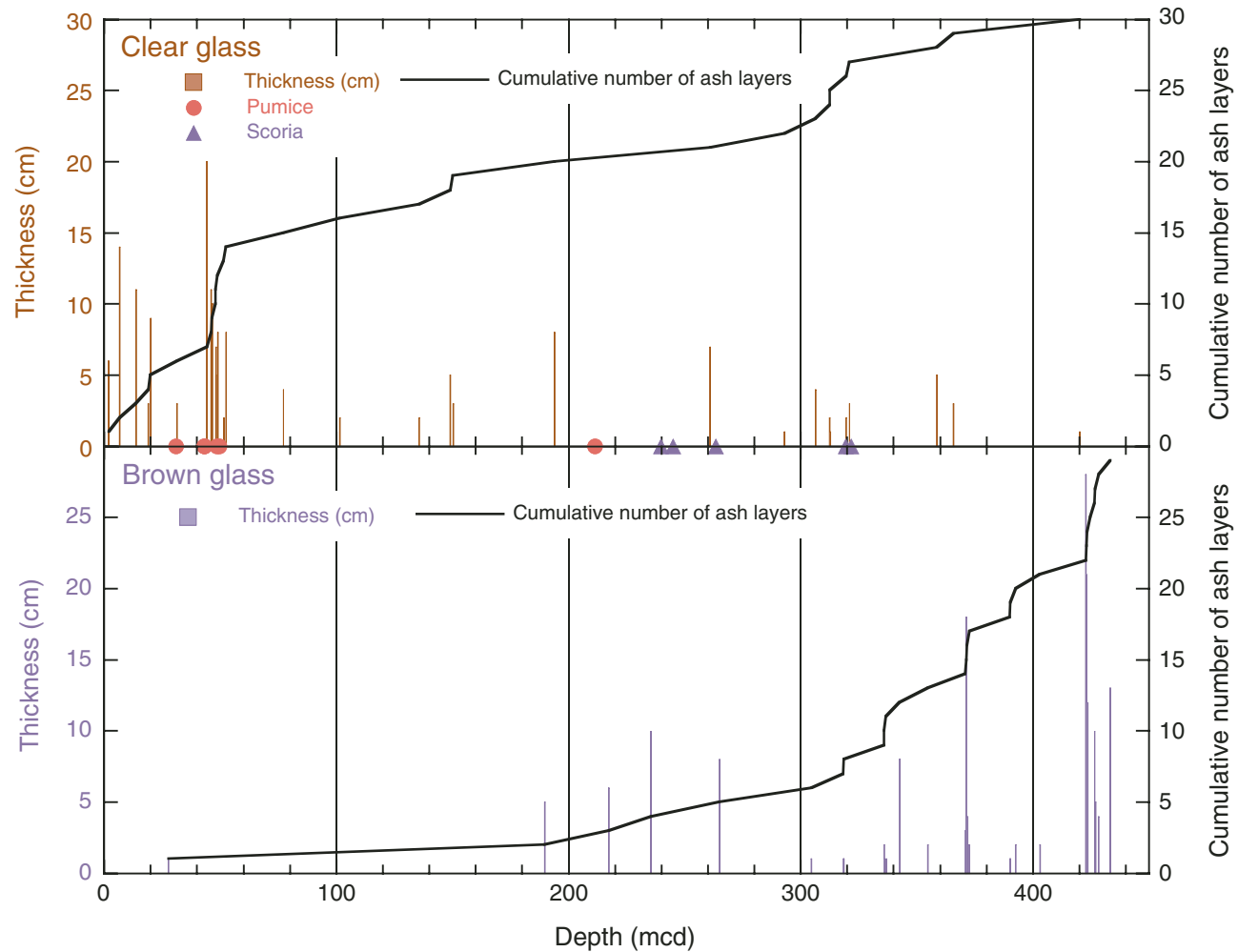


Figure F23. Volcaniclastic horizons at Site 1241 with predominantly clear glass plotted on the age vs. depth profile based on biostratigraphic datums. Length of bars = ash layer thickness. Ash layer frequency (left panel), calculated by linear interpolation of the cumulative curve (right panel), is plotted vs. age.

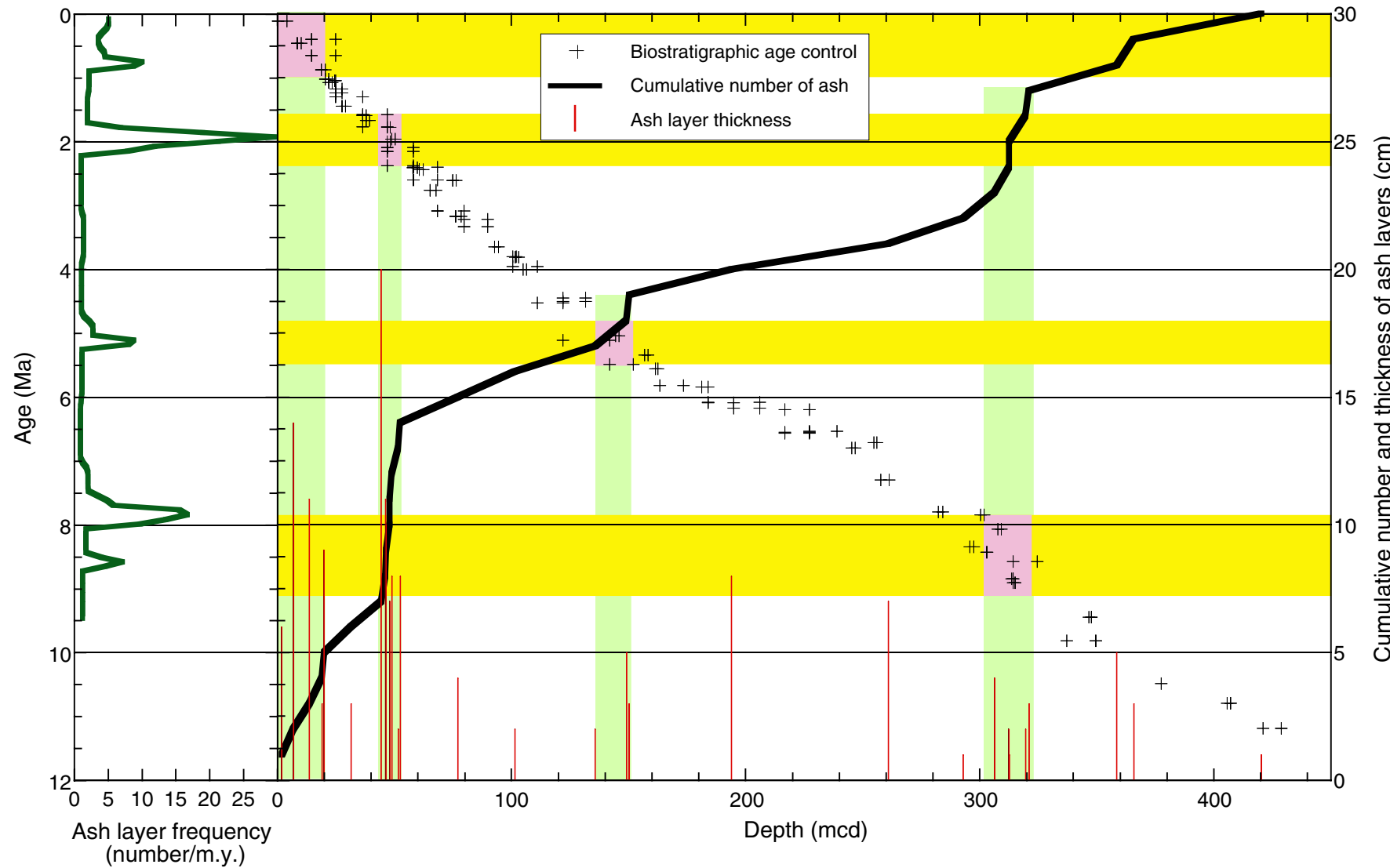


Figure F24. Core recovery, calcareous nannofossil and planktonic foraminifer abundance, benthic foraminifer percentage of total foraminifers, and diatom abundance at Site 1241. R = rare, F = few, C = common, A = abundant.

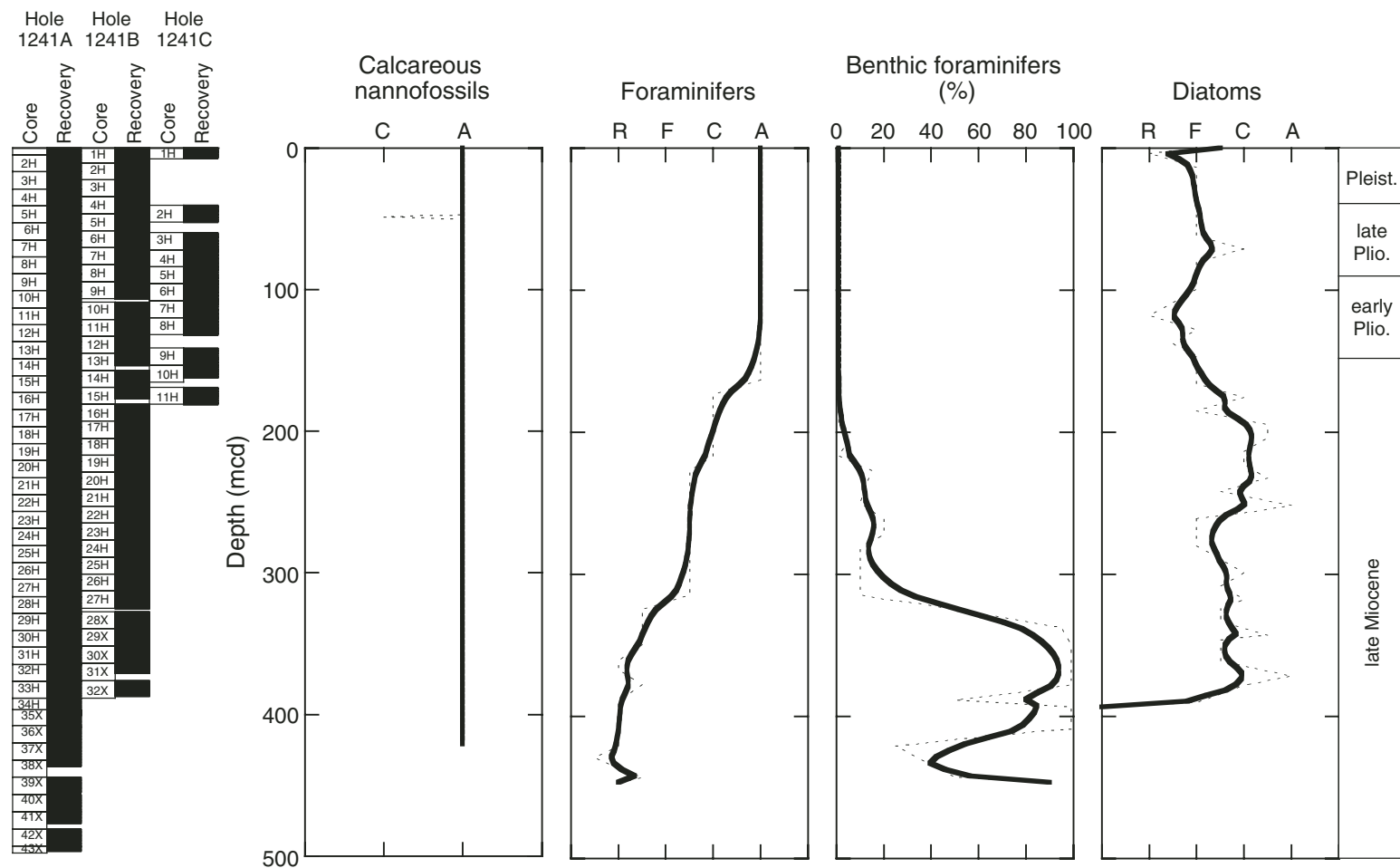


Figure F25. Site 1241 natural remanent magnetization (NRM) intensity before (red) and after (blue) AF demagnetization at 20 mT.

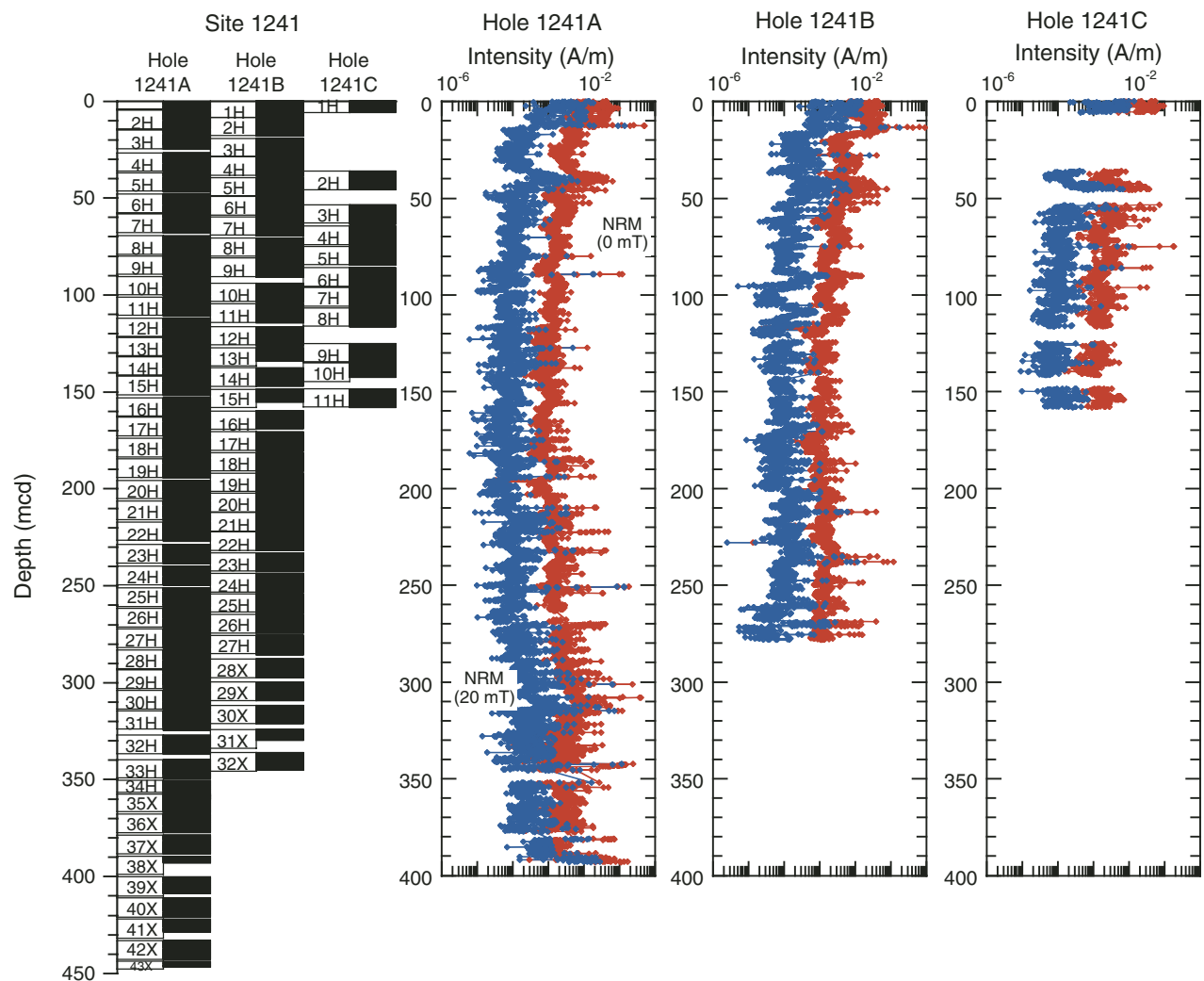


Figure F26. Natural remanent magnetization (NRM) magnetic susceptibility and intensity before and after AF demagnetization at 20 mT for the upper 20 mcd of Hole 1241A.

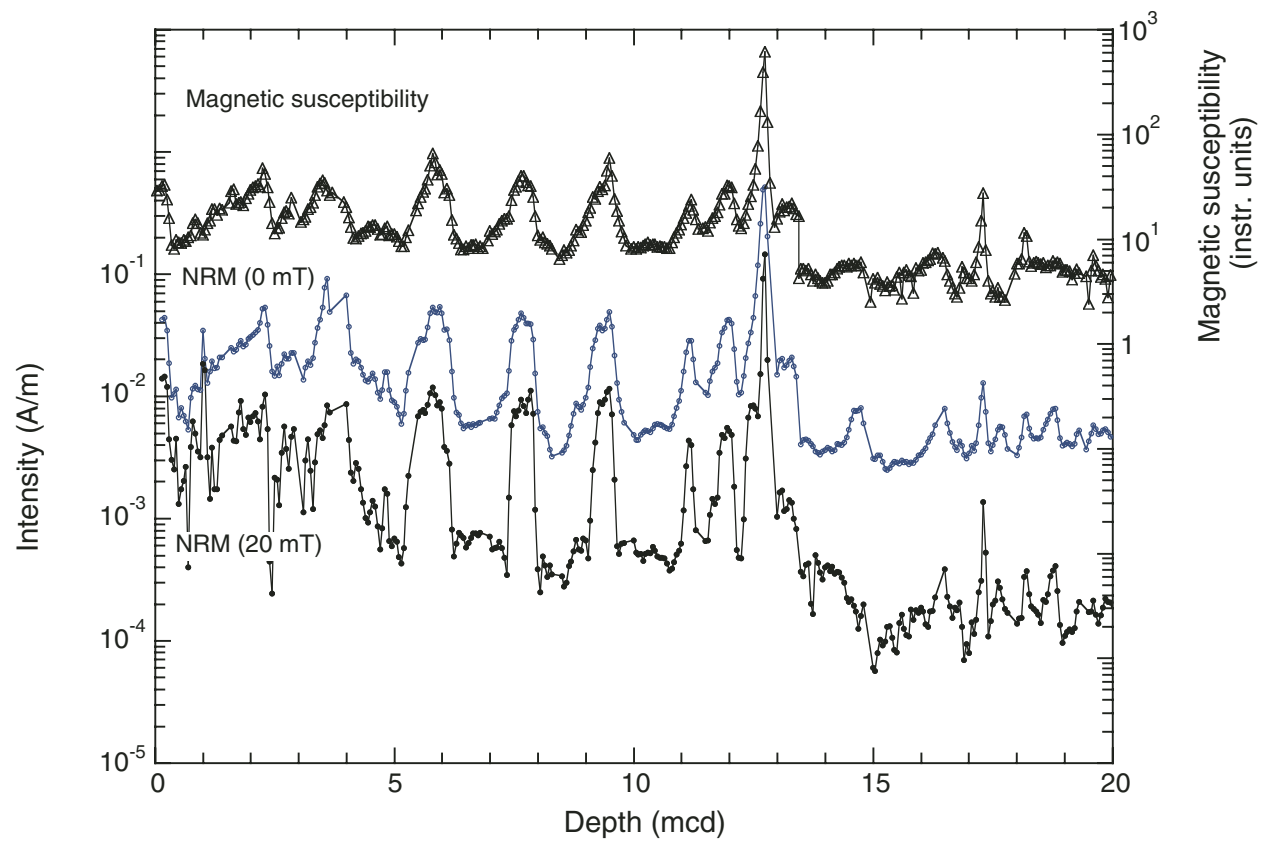


Figure F27. Hole 1241A inclinations and declinations after AF demagnetization at 20 mT. Inclinations are near the expected axial dipole values (7°) in the uppermost 20 mcd.

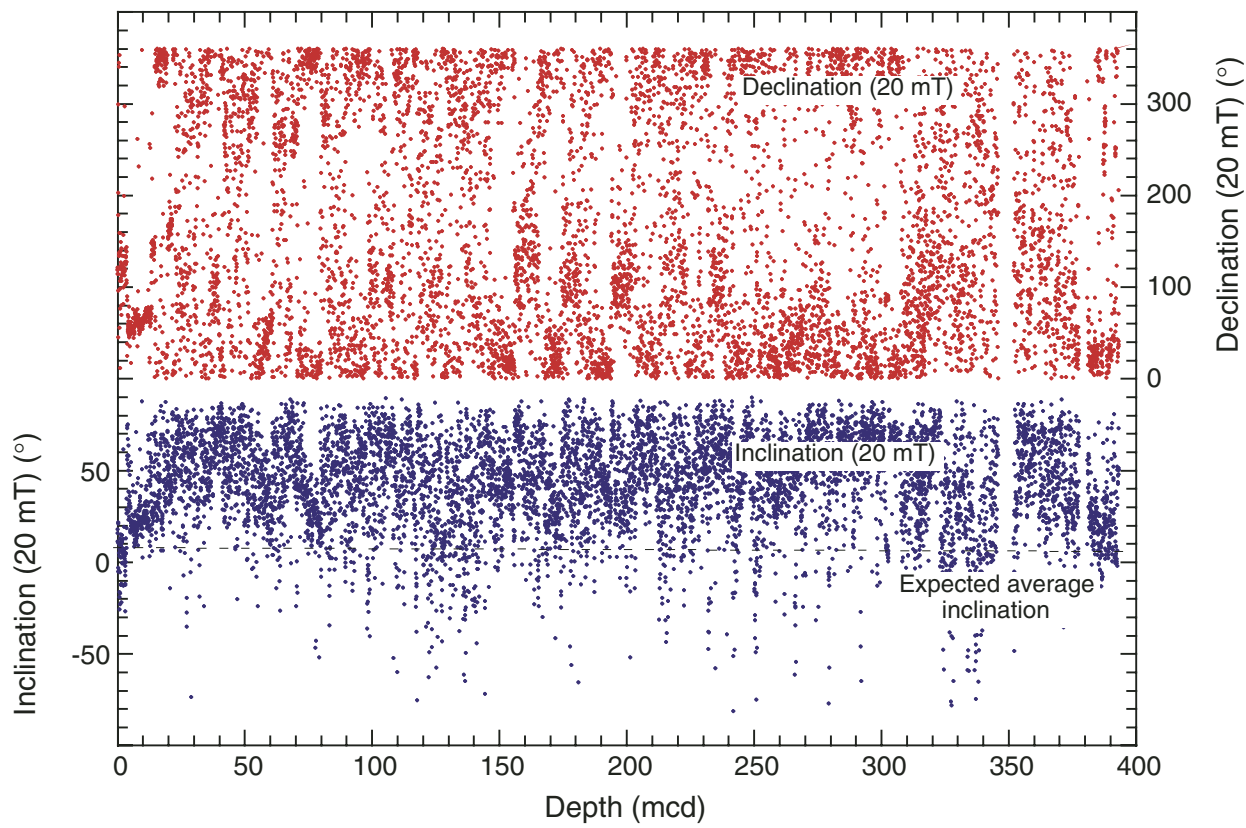


Figure F28. Declinations (20 mT) from Cores 202-1241A-1H through 3H, showing three shifts of $\sim 180^\circ$ that may represent polarity transitions.

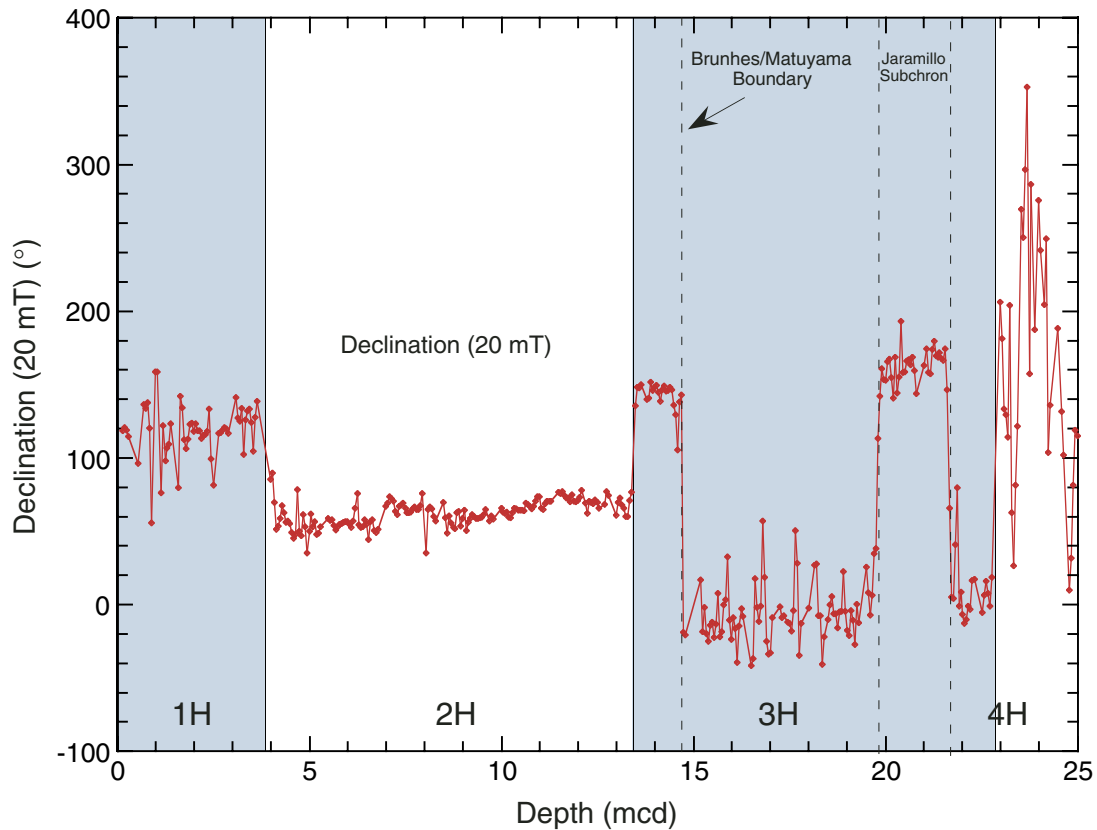


Figure F29. Headspace methane (C_1) concentrations in sediments vs. depth for Hole 1241A.

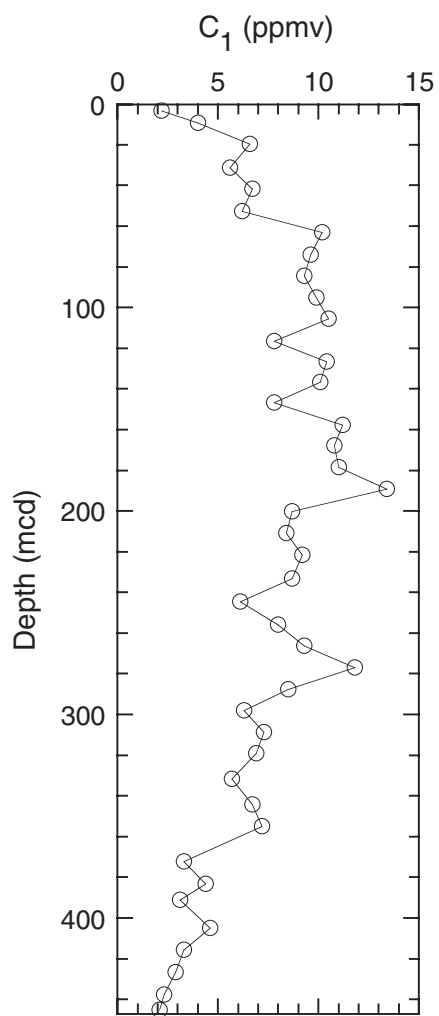


Figure F30. Interstitial water geochemical data for Site 1241. Open squares = calcium concentrations. Horizontal dashed lines indicate lithologic subunit boundaries (see “[Description of Lithologic Unit](#),” p. 6, in “[Lithostratigraphy](#)”). Values below the detection limit (0.2 μM for phosphate) are plotted at zero. Note that blank corrections for manganese (0.2 μM), iron (0.2 μM), and barium (1.6 μM) were significant compared to many of the measured concentrations, so these profiles should be interpreted with caution.

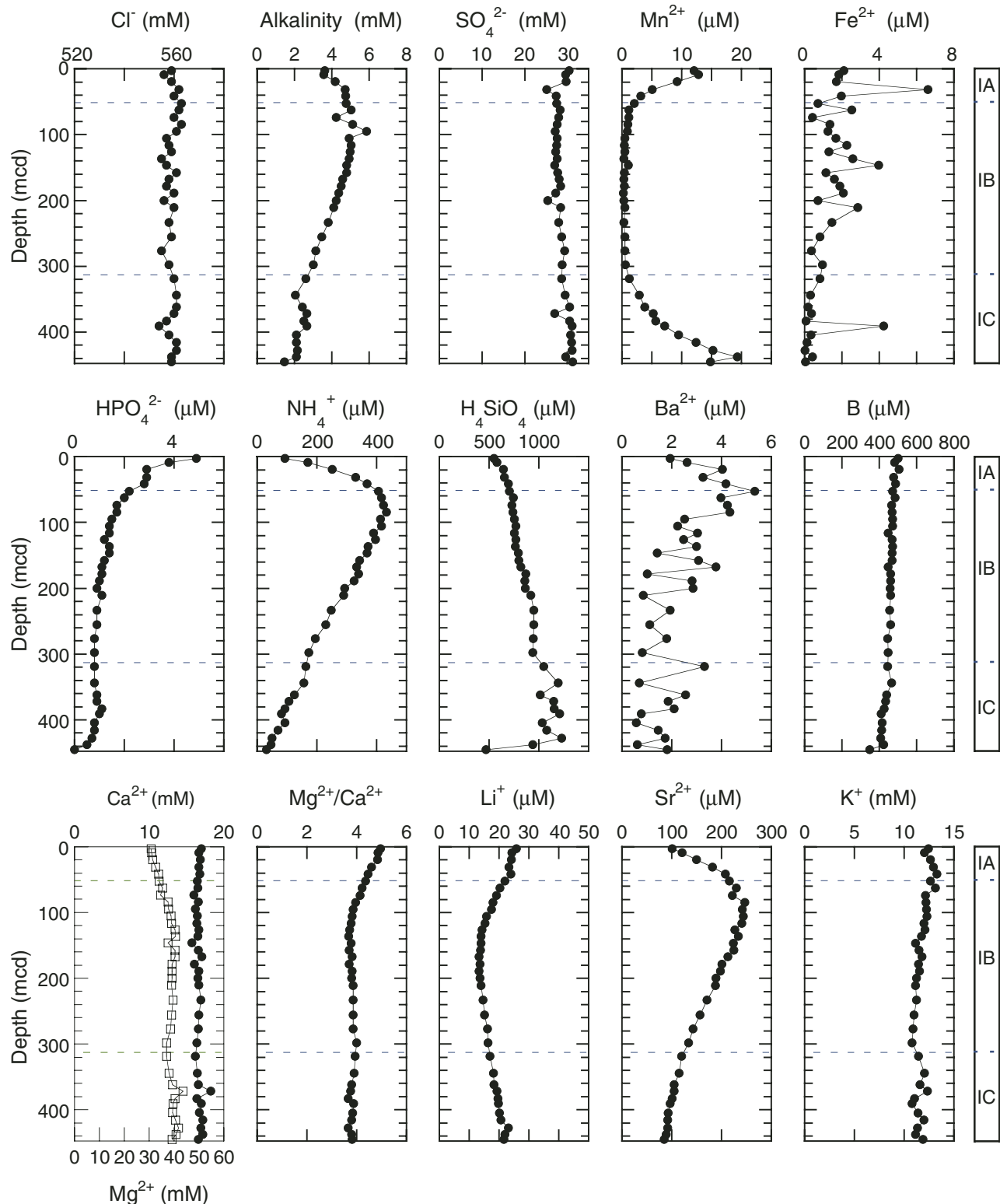


Figure F31. Calcium carbonate (CaCO_3), total organic carbon (TOC), TOC on a carbonate-free basis (TOC CFB), and total nitrogen (TN) concentrations, and TOC/TN ratios vs. depth in sediments from Hole 1241A.

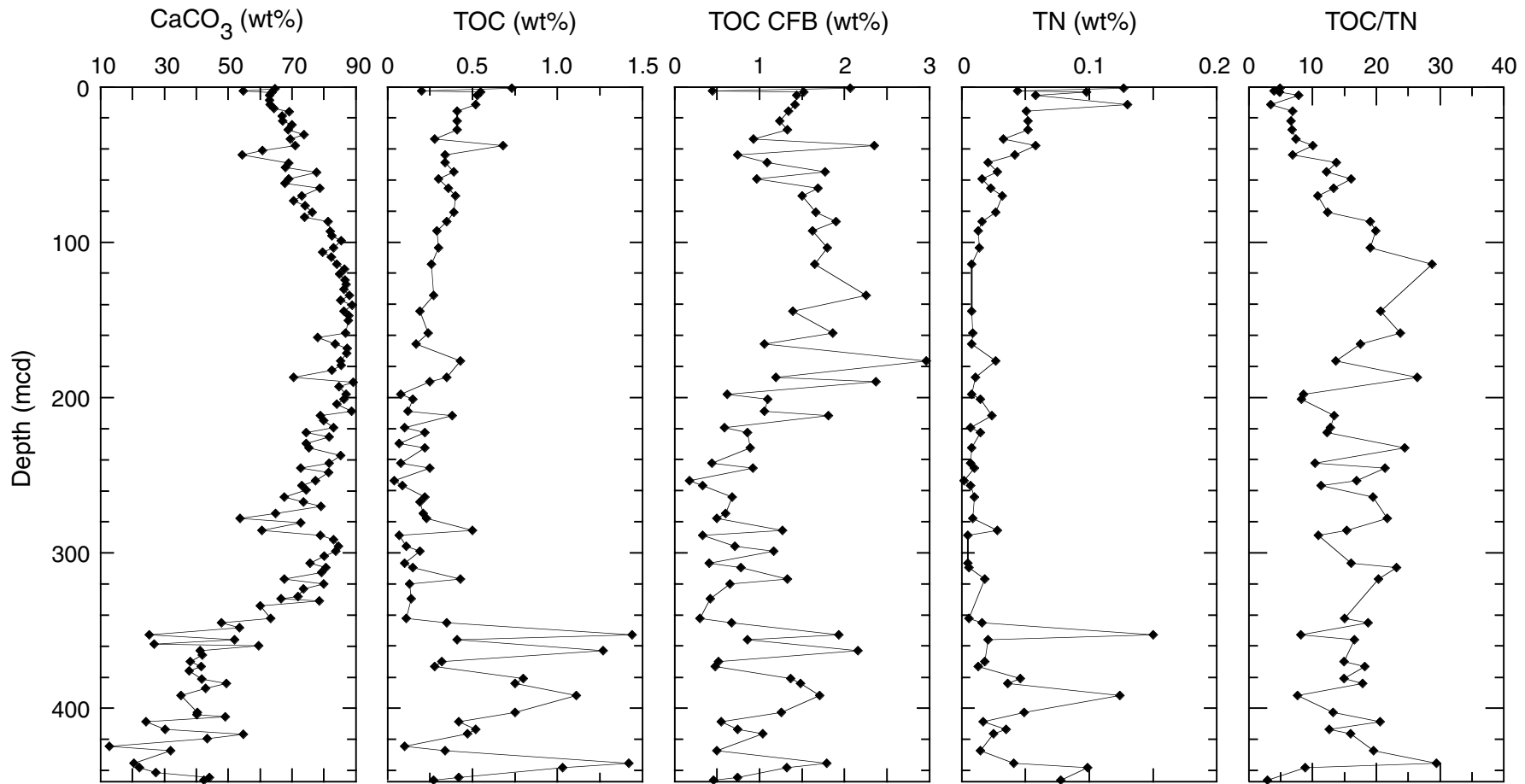


Figure F32. Details of the logging tool string deployments in Hole 1241A. Gray rectangles = drill pipe tools, black rectangles = logging tools. triple combo = triple combination tool string, MGT = Multi-Sensor Spectral Gamma Ray Tool, FMS = Formation MicroScanner-sonic tool string.

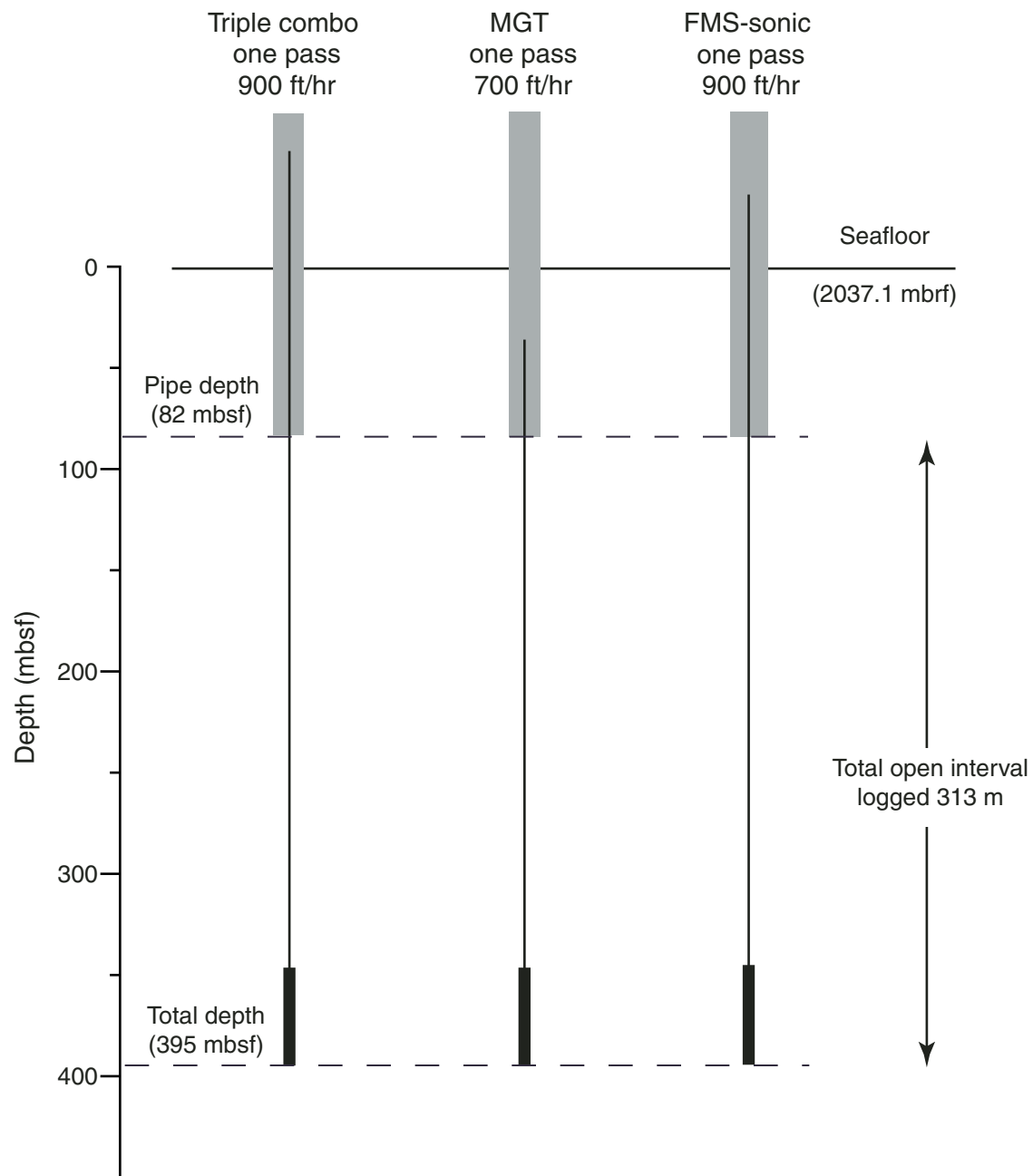


Figure F33. Caliper, deviation from vertical, high-resolution gamma ray, and gamma ray records for Site 1241.

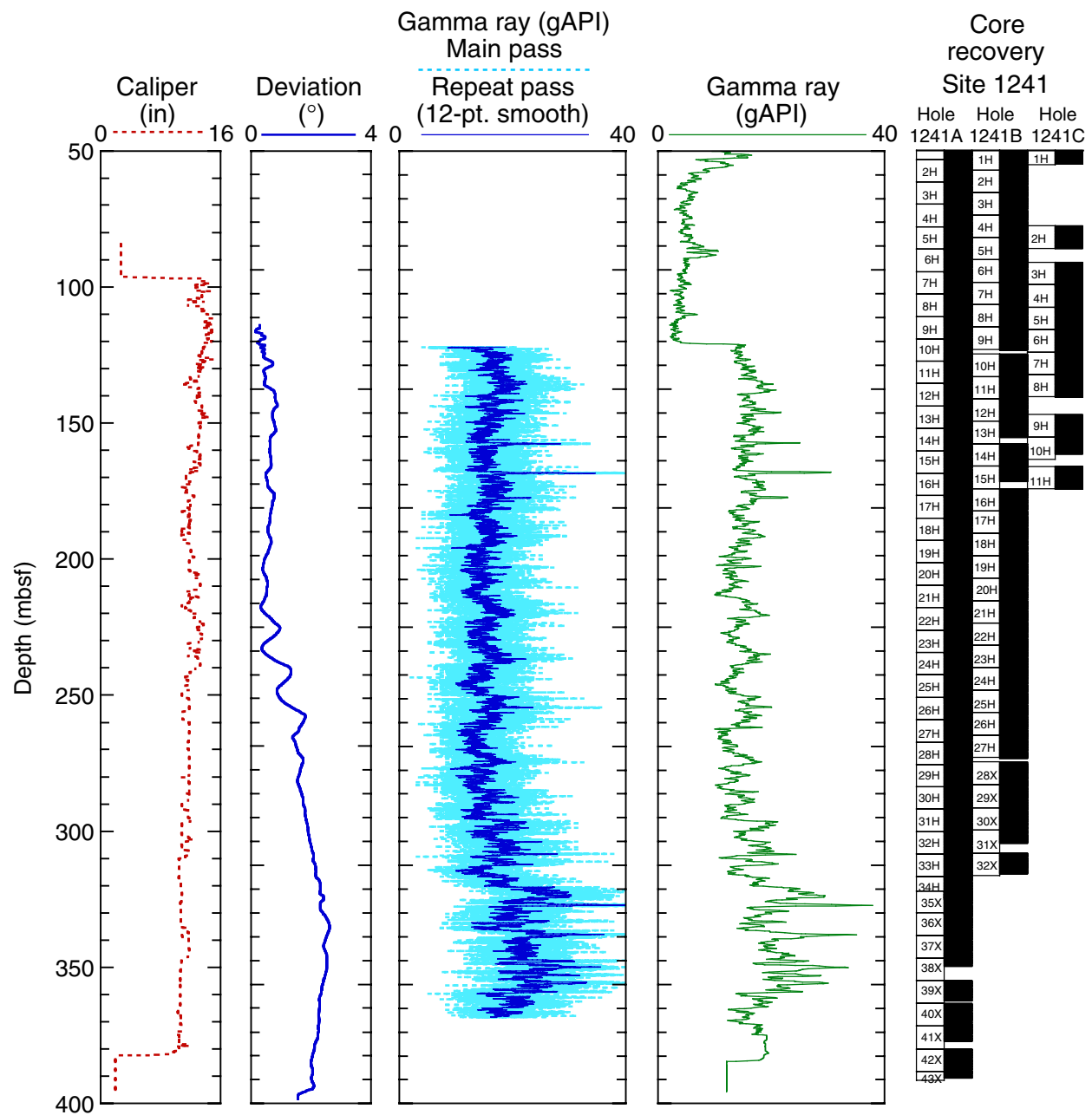


Figure F34. Sonic velocity, resistivity, density, and porosity data for Hole 1241A.

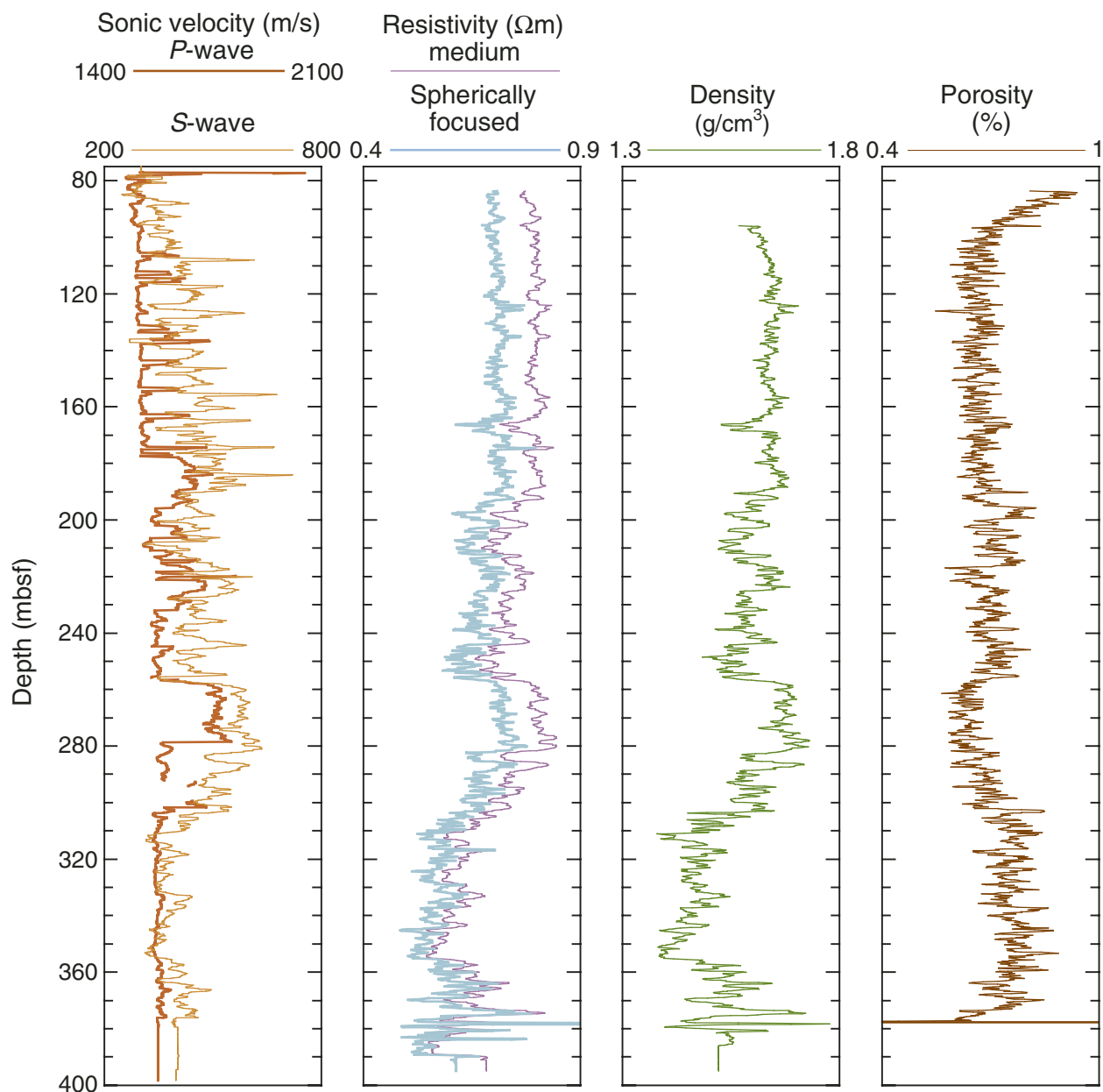


Figure F35. Downhole density plotted with core density. GRA = gamma ray attenuation.

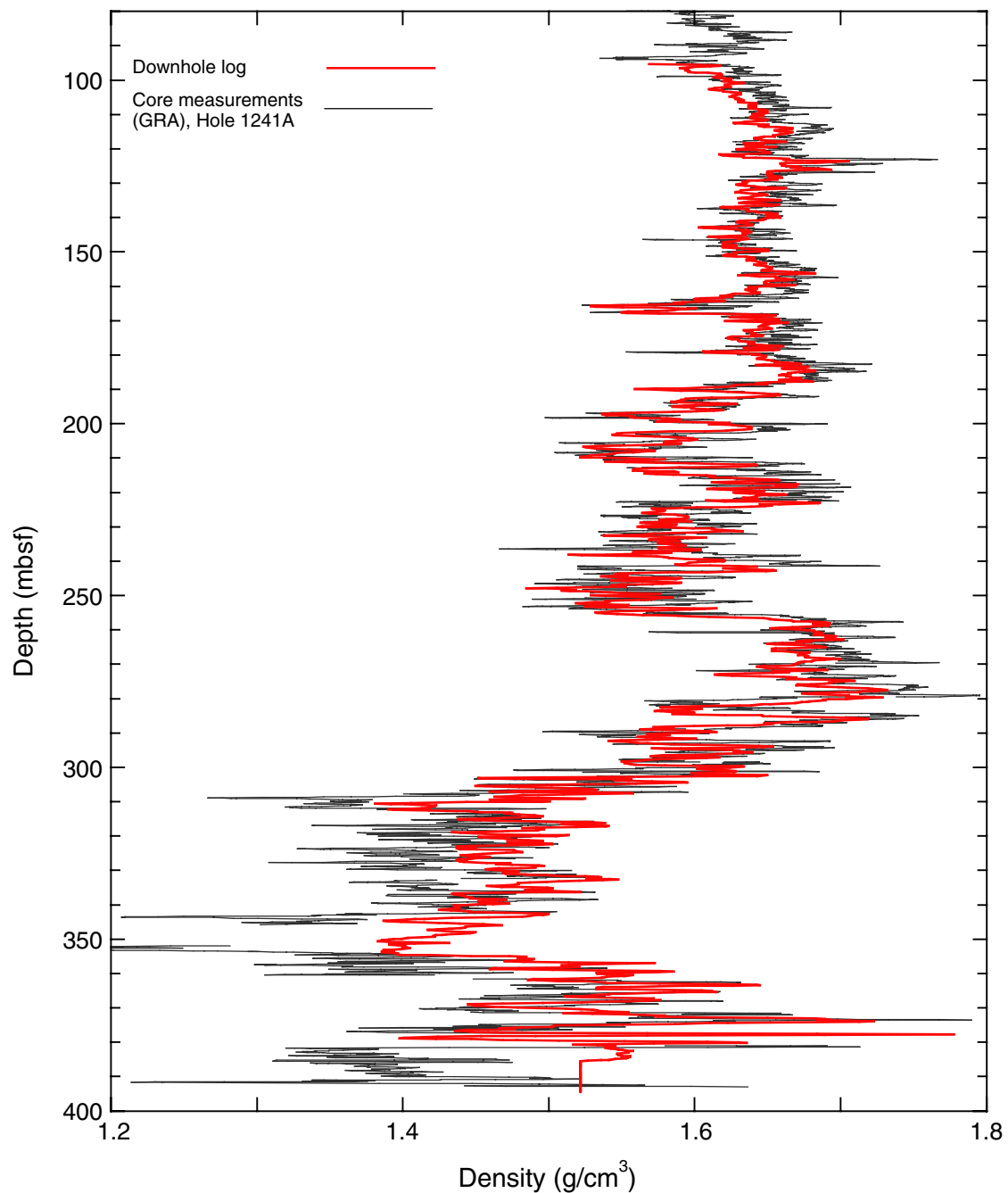


Figure F36. Total gamma ray and spectral gamma ray records for Hole 1241A. HCGR = computed gamma ray, HSGR = total spectral gamma ray.

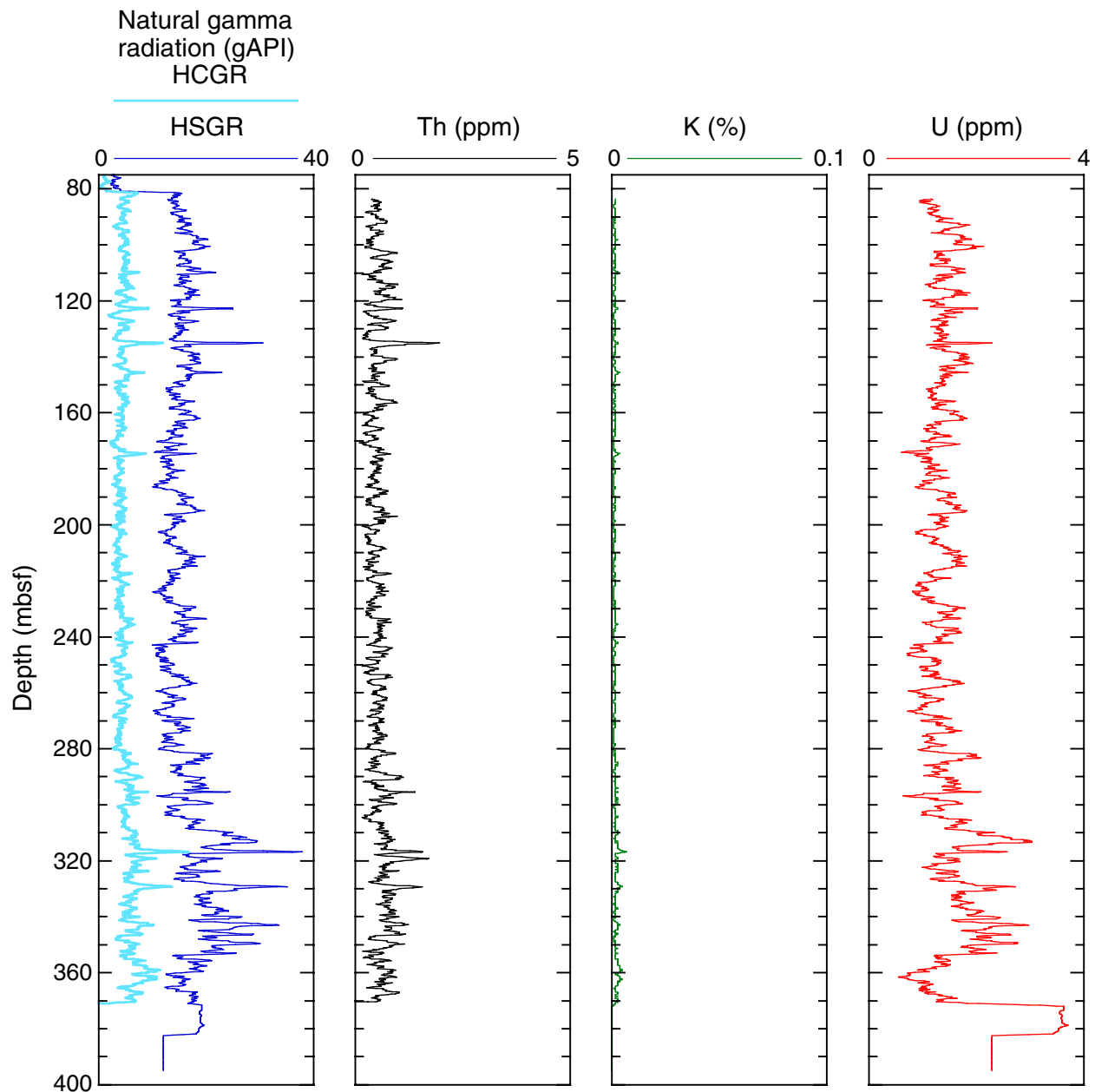


Figure F37. A. Downhole density (blue) and resistivity (black) logs vs. depth over the length of the sequence logged with both tools in Hole 1241B. B. Scatterplot of density vs. resistivity over the sequence represented in A, showing the strongly linear relationship between the two logs.

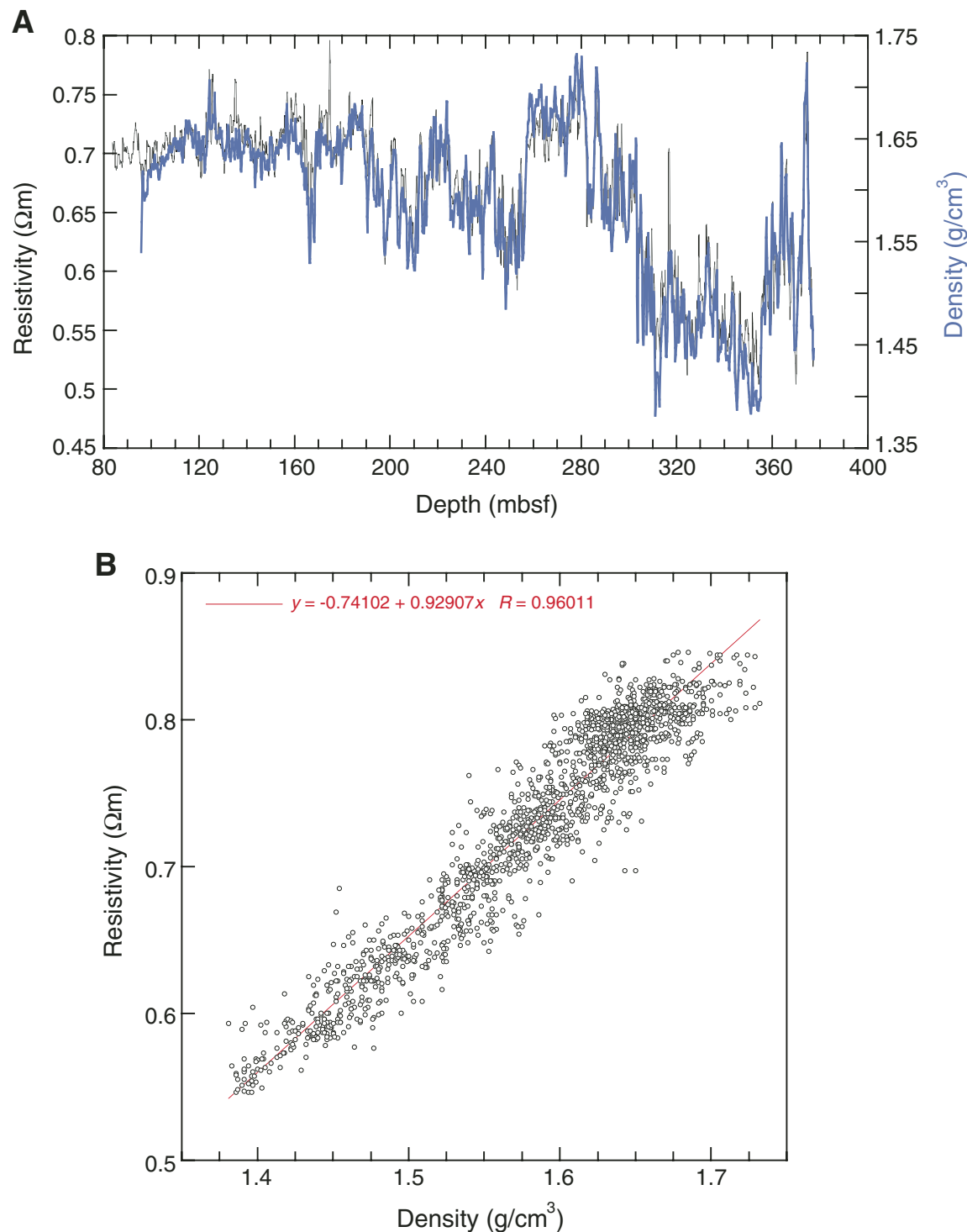


Figure F38. Dynamically normalized Formation MicroScanner (FMS) image of the borehole illustrating the meter-scale banding related to opal to carbonate oscillations. Shown to the left is the average of the 64 microconductivity sensors used to generate the image (red line) and the core gamma ray attenuation (GRA) density record (blue line).

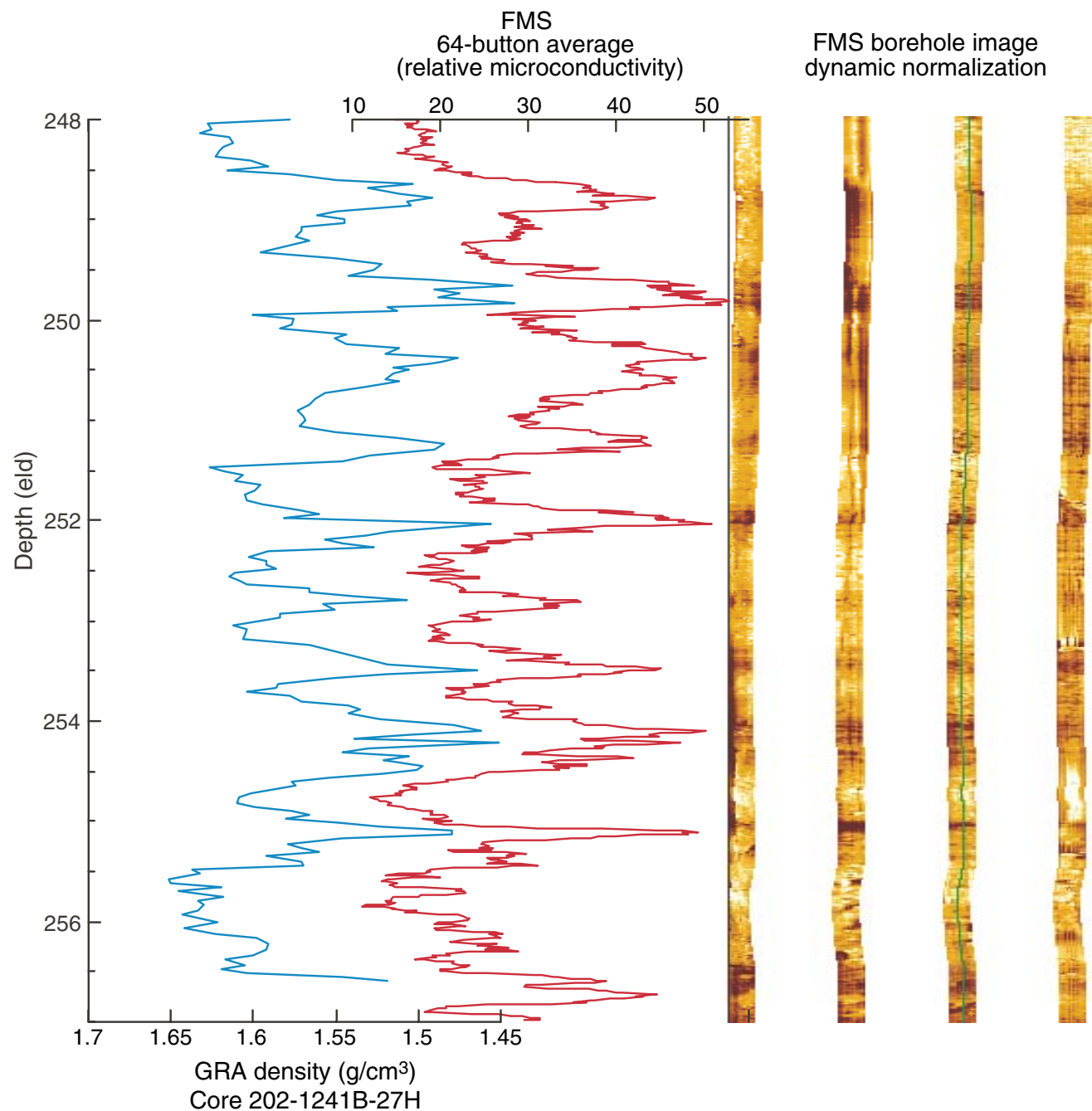


Figure F39. The spherically focused resistivity log from the Dual Induction Tool (blue line) plotted with the conductivity record derived from the average of the 64 buttons on the Formation MicroScanner (FMS) (red line).

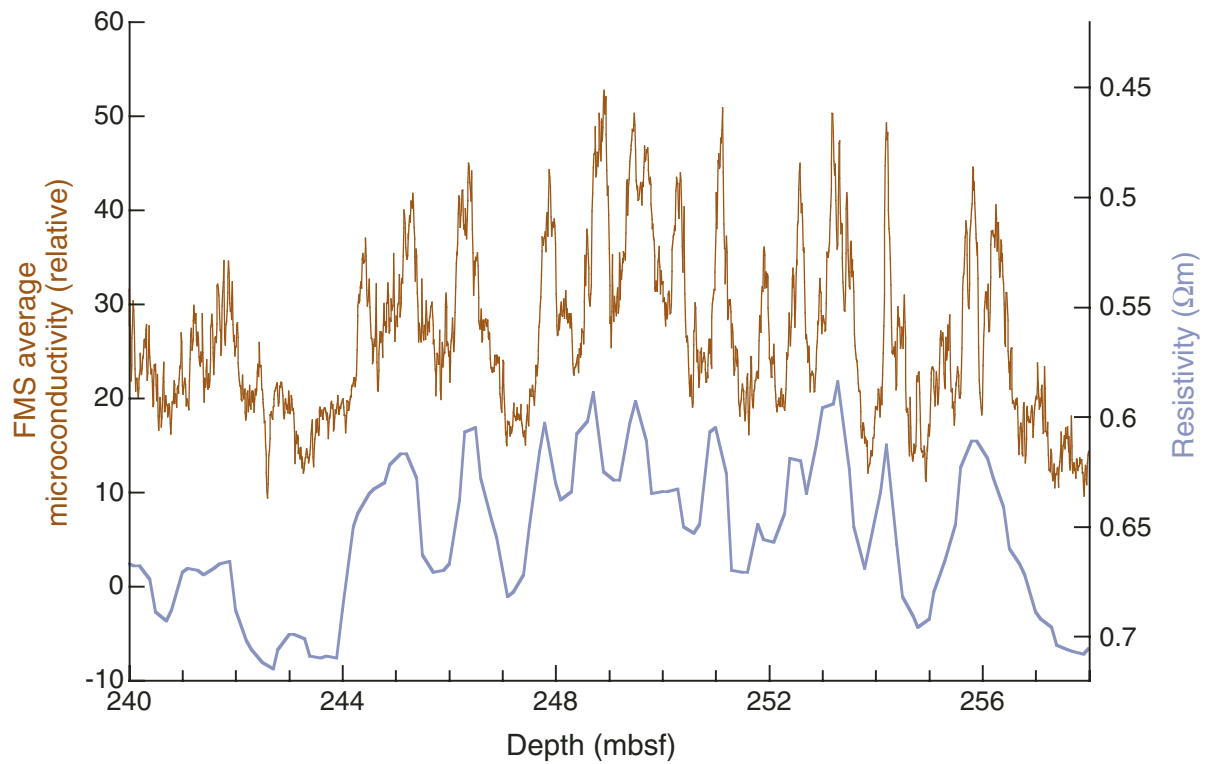
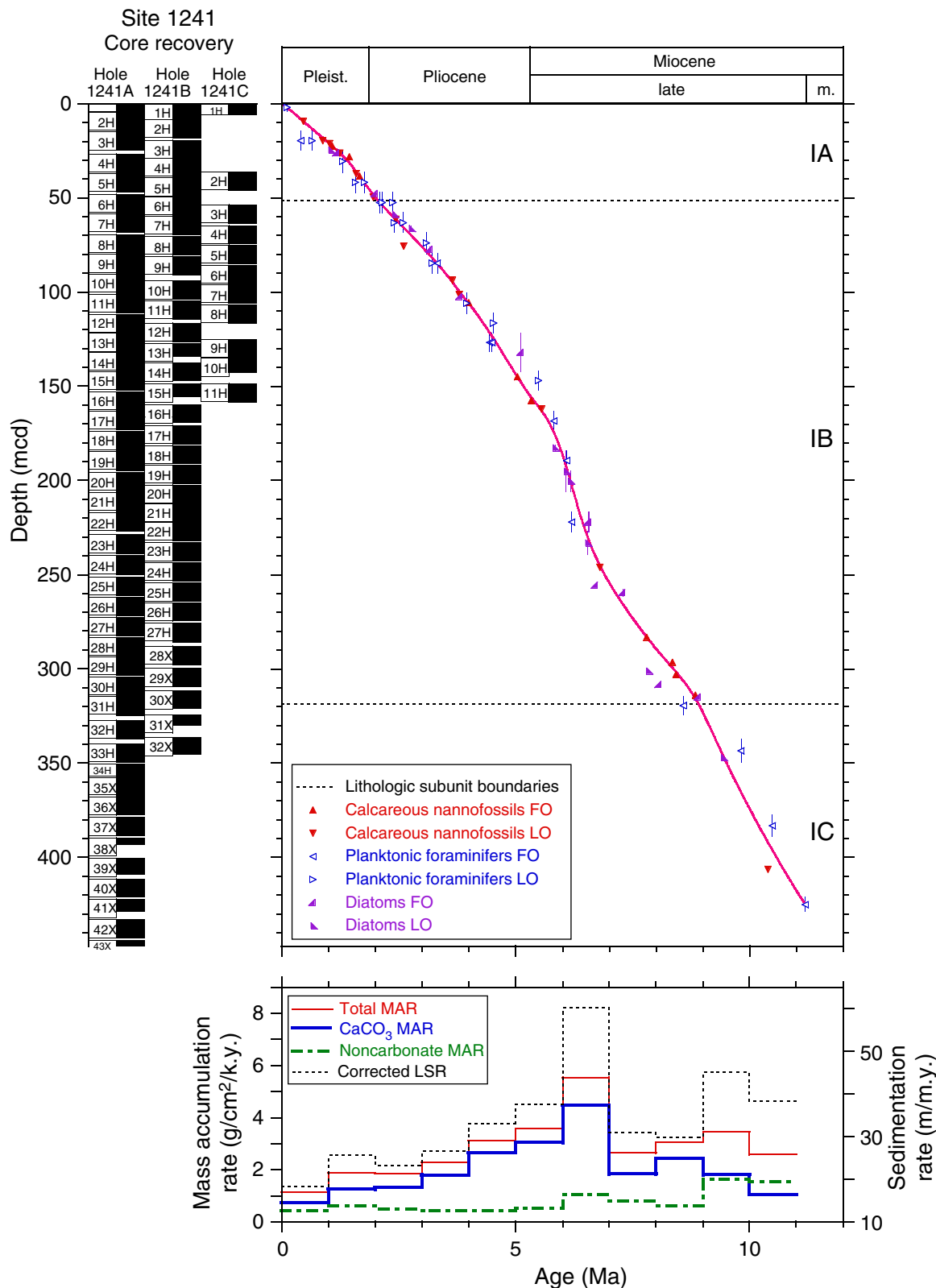


Figure F40. A. Shipboard biostratigraphic and magnetostratigraphic datums and age-depth model. B. Corrected linear sedimentation rates (LSRs), total mass accumulation rates (MARs), and carbonate mass accumulation rates calculated from the smooth age model, average dry density, and calcium carbonate concentrations at 1-m.y. intervals. FO = first occurrence, LO = last occurrence.



SHIPBOARD SCIENTIFIC PARTY
CHAPTER 12, SITE 1241

74

Table T1. Operations summary, Site 1241. (See table notes. Continued on next page.)

Core	Date (May 2002)	Local time (hr)	Depth (mbsf)		Length (m)		Recovery (%)	APCT	Orientation	NMCB
			Top	Bottom	Cored	Recovered				
202-1241A-										
1H	20	2135	0.0	3.9	3.9	3.93	100.8			
2H	20	2215	3.9	13.4	9.5	9.89	104.1		X	
3H	20	2250	13.4	22.9	9.5	9.90	104.2			
4H	20	2355	22.9	32.4	9.5	9.83	103.5	X	Tensor	X
5H	21	0030	32.4	41.9	9.5	9.98	105.1		Tensor	
6H	21	0135	41.9	51.4	9.5	10.07	106.0	X	Tensor	X
7H	21	0220	51.4	60.9	9.5	9.88	104.0		Tensor	
8H	21	0320	60.9	70.4	9.5	10.09	106.2	X	Tensor	X
9H	21	0405	70.4	79.9	9.5	10.06	105.9		Tensor	
10H	21	0500	79.9	89.4	9.5	10.10	106.3	X	Tensor	X
11H	21	0545	89.4	98.9	9.5	9.94	104.6		Tensor	
12H	21	0650	98.9	108.4	9.5	9.82	103.4	X	Tensor	X
13H	21	0730	108.4	117.9	9.5	9.67	101.8		Tensor	
14H	21	0810	117.9	127.4	9.5	9.92	104.4		Tensor	X
15H	21	0850	127.4	136.9	9.5	9.93	104.5		Tensor	
16H	21	0950	136.9	146.4	9.5	10.16	107.0	X	Tensor	X
17H	21	1030	146.4	155.9	9.5	10.12	106.5		Tensor	
18H	21	1110	155.9	165.4	9.5	9.92	104.4		Tensor	X
19H	21	1150	165.4	174.9	9.5	10.10	106.3		Tensor	
20H	21	1250	174.9	184.4	9.5	10.18	107.2	X	Tensor	X
21H	21	1335	184.4	193.9	9.5	10.14	106.7		Tensor	
22H	21	1430	193.9	203.4	9.5	10.00	105.3		Tensor	X
23H	21	1525	203.4	212.9	9.5	10.19	107.3		Tensor	
24H	21	1600	212.9	222.4	9.5	9.88	104.0		Tensor	
25H	21	1650	222.4	231.9	9.5	10.08	106.1		Tensor	
26H	21	1740	231.9	241.4	9.5	9.99	105.2		Tensor	
27H	21	1859	241.4	250.9	9.5	10.11	106.4		Tensor	
28H	21	2015	250.9	260.4	9.5	10.05	105.8		Tensor	
29H	21	2245	260.4	269.9	9.5	9.76	102.7		Tensor	
30H	22	0145	269.9	279.4	9.5	10.07	106.0		Tensor*	
31H	22	0310	279.4	288.9	9.5	9.93	104.5		Tensor*	
32H	22	0430	288.9	298.4	9.5	9.97	105.0		Tensor*	
33H	22	0615	298.4	307.9	9.5	9.82	103.4		Tensor*	
34H	22	0915	307.9	314.2	6.3	9.88	156.8		Tensor	
35X	22	1030	314.2	323.2	9.0	9.83	109.2			
36X	22	1115	323.2	332.9	9.7	9.78	100.8			
37X	22	1205	332.9	342.5	9.6	9.87	102.8			
38X	22	1250	342.5	352.0	9.5	3.68	38.7			
39X	22	1340	352.0	361.7	9.7	8.90	91.8			
40X	22	1430	361.7	371.3	9.6	9.82	102.3			
41X	22	1525	371.3	381.0	9.7	6.74	69.5			
42X	22	1610	381.0	390.6	9.6	9.80	102.1			
43X	22	1745	390.6	394.4	3.8	3.08	81.1			
			Cored totals:		394.4	404.86	102.7			
202-1241B-										
1H	22	2125	0.0	8.4	8.4	8.42	100.2	X		X
2H	22	2200	8.4	17.9	9.5	9.98	105.1			
3H	22	2235	17.9	27.4	9.5	9.92	104.4		X	
4H	22	2305	27.4	36.9	9.5	10.03	105.6			
5H	22	2345	36.9	46.4	9.5	9.97	105.0		X	
6H	23	0015	46.4	55.9	9.5	9.95	104.7			
7H	23	0050	55.9	65.4	9.5	9.95	104.7		X	
8H	23	0125	65.4	74.9	9.5	10.01	105.4			
9H	23	0200	74.9	84.4	9.5	9.98	105.1		X	
10H	23	0240	86.4	95.9	9.5	9.96	104.8			
11H	23	0310	95.9	105.4	9.5	9.92	104.4		X	
12H	23	0345	105.4	114.9	9.5	9.95	104.7			
13H	23	0415	114.9	124.4	9.5	7.07	74.4		X	
14H	23	0450	124.4	133.9	9.5	9.42	99.2			
15H	23	0530	133.9	143.4	9.5	6.78	71.4		X	
16H	23	0605	143.4	152.9	9.5	9.29	97.8			
17H	23	0640	152.9	162.4	9.5	10.00	105.3		X	
18H	23	0720	162.4	171.9	9.5	9.73	102.4			
19H	23	0755	171.9	181.4	9.5	9.95	104.7		X	
20H	23	0835	181.4	190.9	9.5	9.33	98.2			
21H	23	0923	190.9	200.4	9.5	9.71	102.2		X	

Table T1 (continued).

Core	Date (May 2002)	Local time (hr)	Depth (mbsf)		Length (m)		Recovery (%)	APCT	Orientation	NMCB
			Top	Bottom	Cored	Recovered				
22H	23	1005	200.4	209.9	9.5	9.83	103.5			
23H	23	1055	209.9	219.4	9.5	9.75	102.6			
24H	23	1145	219.4	228.9	9.5	9.77	102.8			
25H	23	1235	228.9	238.4	9.5	9.96	104.8			
26H	23	1335	238.4	247.9	9.5	9.73	102.4			
27H	23	1500	247.9	257.4	9.5	10.07	106.0			
28X	23	1550	259.4	269.0	9.6	9.89	103.0			
29X	23	1630	269.0	278.7	9.7	9.67	99.7			
30X	23	1710	278.7	288.3	9.6	9.55	99.5			
31X	23	1800	288.3	298.0	9.7	5.75	59.3			
32X	23	1855	298.0	307.6	9.6	8.94	93.1			
			Cored totals:		303.6	302.23	99.5			
202-1241C-										
1H	24	1620	0.0	6.0	6.0	6.02	100.3			
2H	24	1740	32.0	41.5	9.5	9.80	103.2	X		
3H	24	1845	47.5	57.0	9.5	10.11	106.4			
4H	24	1920	57.0	66.5	9.5	9.97	105.0	X		
5H	24	2000	66.5	76.0	9.5	9.95	104.7			
6H	24	2040	76.0	85.5	9.5	9.92	104.4	X		
7H	24	2120	85.5	95.0	9.5	10.04	105.7			
8H	24	2200	95.0	104.5	9.5	9.92	104.4	X		
9H	24	2300	112.0	121.5	9.5	9.88	104.0			
10H	24	2335	121.5	131.0	9.5	7.57	79.7	X		
11H	25	0055	134.0	143.5	9.5	9.87	103.9			
			Cored totals:		101.0	103.05	102.0			
			Site Totals:		799.0	810.14	101.4			

Notes: APCT = advanced piston corer temperature tool (stainless-steel housing is cutting shoe). NMCB = nonmagnetic core barrel, including cutting shoe (made from monel). X = APCT or NMCB was used. Tensor = brand name for core-barrel orientation tool. * = Tensor measurement attempted but problem occurred, resulting in bad or no data.

Table T2. Composite depth scale, Site 1241. (See table notes. Continued on next page.)

Core	Depth of core top		Depth offset		Translation to cmcd	
	Drillers (mbsf)	Composite (mcd)	Cumulative (m)	Differential (m)	Growth factor*	Depth (cmcd)†
202-1241A-						
1H	0.0	0.30	0.30	0.30	1.13	0.27
2H	3.9	4.85	0.95	0.65	1.13	4.29
3H	13.4	15.15	1.75	0.80	1.13	13.41
4H	22.9	26.84	3.94	2.19	1.13	23.75
5H	32.4	37.12	4.72	0.78	1.13	32.85
6H	41.9	48.07	6.17	1.45	1.13	42.54
7H	51.4	58.43	7.03	0.86	1.13	51.71
8H	60.9	69.59	8.69	1.66	1.13	61.58
9H	70.4	80.04	9.64	0.95	1.13	70.83
10H	79.9	90.62	10.72	1.08	1.13	80.19
11H	89.4	101.20	11.80	1.08	1.13	89.56
12H	98.9	112.10	13.20	1.40	1.13	99.20
13H	108.4	121.99	13.59	0.39	1.13	107.96
14H	117.9	132.07	14.17	0.58	1.13	116.88
15H	127.4	142.12	14.72	0.55	1.13	125.77
16H	136.9	153.15	16.25	1.53	1.13	135.53
17H	146.4	163.24	16.84	0.59	1.13	144.46
18H	155.9	174.14	18.24	1.40	1.13	154.11
19H	165.4	184.68	19.28	1.04	1.13	163.43
20H	174.9	195.78	20.88	1.60	1.13	173.26
21H	184.4	206.53	22.13	1.25	1.13	182.77
22H	193.9	217.19	23.29	1.16	1.13	192.20
23H	203.4	228.80	25.40	2.11	1.13	202.48
24H	212.9	240.05	27.15	1.75	1.13	212.43
25H	222.4	251.24	28.84	1.69	1.13	222.34
26H	231.9	261.93	30.03	1.19	1.13	231.80
27H	241.4	272.45	31.05	1.02	1.13	241.11
28H	250.9	283.35	32.45	1.40	1.13	250.75
29H	260.4	293.59	33.19	0.74	1.13	259.81
30H	269.9	304.24	34.34	1.15	1.13	269.24
31H	279.4	314.68	35.28	0.94	1.13	278.48
32H	288.9	327.24	38.34	3.06	1.13	289.59
33H	298.4	337.19	41.39	3.05	1.13	298.40
34H	307.9	347.93	42.63	1.24	1.13	307.90
35X	314.2	355.05	43.45	0.82	1.13	314.20
36X	323.2	365.22	44.62	1.17	1.13	323.20
37X	332.9	376.18	45.88	1.26	1.13	332.90
38X	342.5	387.02	47.12	1.24	1.13	342.50
39X	352.0	397.76	48.36	1.24	1.13	352.00
40X	361.7	408.72	49.62	1.26	1.13	361.70
41X	371.3	419.57	50.87	1.25	1.13	371.30
42X	381.0	430.53	52.13	1.26	1.13	381.00
43X	390.6	441.38	53.38	1.25	1.13	390.60
202-1241B-						
1H	0.0	0.00	0.00	0.00	1.13	0.00
2H	8.4	8.45	0.05	0.05	1.13	7.48
3H	17.9	19.37	1.47	1.42	1.13	17.14
4H	27.4	28.87	1.47	0.00	1.13	25.55
5H	36.9	39.52	2.62	1.15	1.13	34.97
6H	46.4	49.48	3.08	0.46	1.13	43.79
7H	55.9	59.80	3.90	0.82	1.13	52.92
8H	65.4	70.65	5.25	1.35	1.13	62.52
9H	74.9	81.15	6.25	1.00	1.13	71.81
10H	86.4	94.12	7.72	1.47	1.13	83.29
11H	95.9	104.71	8.81	1.09	1.13	92.66
12H	105.4	116.50	11.10	2.29	1.13	103.10
13H	114.9	127.37	12.47	1.37	1.13	112.72
14H	124.4	137.77	13.37	0.90	1.13	121.92
15H	133.9	148.77	14.87	1.50	1.13	131.65
16H	143.4	159.90	16.50	1.63	1.13	141.50
17H	152.9	170.80	17.90	1.40	1.13	151.15
18H	162.4	181.39	18.99	1.09	1.13	160.52
19H	171.9	192.03	20.13	1.14	1.13	169.94
20H	181.4	202.48	21.08	0.95	1.13	179.19
21H	190.9	212.38	21.48	0.40	1.13	187.95

Table T2 (continued).

Core	Depth of core top		Depth offset		Translation to cmcd	
	Drillers (mbsf)	Composite (mcd)	Cumulative (m)	Differential (m)	Growth factor*	Depth (cmcd) [†]
22H	200.4	222.31	21.91	0.43	1.13	196.73
23H	209.9	233.05	23.15	1.24	1.13	206.24
24H	219.4	243.74	24.34	1.19	1.13	215.70
25H	228.9	254.33	25.43	1.09	1.13	225.07
26H	238.4	264.90	26.50	1.07	1.13	234.42
27H	247.9	275.65	27.75	1.25	1.13	243.94
28X	259.4	287.85	28.45	0.70	1.13	254.73
29X	269.0	299.74	30.74	2.29	1.13	265.26
30X	278.7	311.73	33.03	2.29	1.13	275.87
31X	288.3	324.24	35.94	2.91	1.13	286.94
32X	298.0	333.29	38.29	2.35	1.13	294.95
202-1241C-						
1H	0.0	0.05	0.05	0.05	1.13	0.04
2H	32.0	36.27	4.27	4.22	1.13	32.10
3H	47.5	53.69	6.19	1.92	1.13	47.51
4H	57.0	64.65	7.65	1.46	1.13	57.21
5H	66.5	75.05	8.55	0.90	1.13	66.42
6H	76.0	86.02	10.02	1.47	1.13	76.12
7H	85.5	96.32	10.82	0.80	1.13	85.24
8H	95.0	106.86	11.86	1.04	1.13	94.57
9H	112.0	125.22	13.22	1.36	1.13	110.81
10H	121.5	135.31	13.81	0.59	1.13	119.74
11H	134.0	148.57	14.57	0.76	1.13	131.48

Notes: * = calculated based on mbsf-mcd relationship for splice shown in Figure F13, p. 46. † = within the splice, the following equations apply: cmcd (mcd/growth factor); mcd = mbsf + cumulative depth offset; mcd = cmcd × growth factor; mbsf = cmcd × growth factor – cumulative offset. This table is also available in [ASCII](#).

Table T3. Splice tie points, Site 1241.

Hole, core, section, interval (cm)	Depth			Hole, core, section, interval (cm)	Depth		
	(mbsf)	(mcd)	(cmcd)		(mbsf)	(mcd)	(cmcd)
202-							
1241B-1H-5, 25	6.25	6.25	5.53	Tie to 1241A-2H-1, 140	5.30	6.25	5.53
1241A-2H-6, 60	12.00	12.95	11.46	Tie to 1241B-2H-3, 150	12.90	12.95	11.46
1241B-2H-6, 95	16.85	16.90	14.96	Tie to 1241A-3H-2, 25	15.15	16.90	14.96
1241A-3H-6, 100	21.90	23.65	20.93	Tie to 1241B-3H-3, 135	22.18	23.65	20.93
1241B-3H-6, 115	26.48	27.95	24.73	Tie to 1241A-4H-1, 109	24.01	27.95	24.73
1241A-4H-6, 70	31.12	35.06	31.03	Tie to 1241B-4H-5, 18.5	33.59	35.06	31.03
1241B-4H-6, 95	35.85	37.32	33.03	Tie to 1241C-2H-1, 105	33.05	37.32	33.03
1241C-2H-6, 75	40.25	44.52	39.40	Tie to 1241B-5H-4, 50	41.90	44.52	39.40
1241B-5H-6, 140	45.80	48.42	42.85	Tie to 1241A-6H-1, 35	42.25	48.42	42.85
1241A-6H-6, 40	49.82	55.99	49.55	Tie to 1241C-3H-2, 80	49.80	55.99	49.55
1241C-3H-6, 30	55.30	61.49	54.42	Tie to 1241A-7H-3, 3.5	54.46	61.49	54.42
1241A-7H-6, 45	59.38	66.41	58.77	Tie to 1241C-4H-2, 24	58.76	66.41	58.77
1241C-4H-6, 100	65.50	73.15	64.73	Tie to 1241B-8H-2, 100	67.90	73.15	64.73
1241B-8H-5, 125	72.65	77.90	68.94	Tie to 1241C-5H-2, 135	69.35	77.90	68.94
1241C-5H-6, 90	74.90	83.45	73.85	Tie to 1241A-9H-3, 40	73.81	83.45	73.85
1241A-9H-7, 15	79.58	89.22	78.96	Tie to 1241C-6H-3, 20	79.20	89.22	78.96
1241C-6H-5, 15	82.15	92.17	81.57	Tie to 1241A-10H-2, 5	81.45	92.17	81.57
1241A-10H-6, 65	88.05	98.77	87.41	Tie to 1241C-7H-2, 95	87.95	98.77	87.41
1241C-7H-7, 60	95.10	105.92	93.73	Tie to 1241A-11H-4, 18.5	94.12	105.92	93.73
1241A-11H-5, 115	96.59	108.39	95.92	Tie to 1241C-8H-2, 2	96.53	108.39	95.92
1241C-8H-6, 65	103.15	115.01	101.78	Tie to 1241A-12H-2, 140	101.81	115.01	101.78
1241A-12H-5, 115	106.05	119.25	105.53	Tie to 1241B-12H-2, 125	108.15	119.25	105.53
1241B-12H-6, 135	114.25	125.35	110.93	Tie to 1241A-13H-3, 34	111.76	125.35	110.93
1241A-13H-5, 110	115.53	129.12	114.27	Tie to 1241C-9H-3, 90	115.90	129.12	114.27
1241C-9H-5, 135	119.35	132.57	117.32	Tie to 1241A-14H-1, 50	118.40	132.57	117.32
1241A-14H-6, 70	126.10	140.27	124.13	Tie to 1241B-14H-2, 100	126.90	140.27	124.13
1241B-14H-5, 130	131.70	145.07	128.38	Tie to 1241A-15H-2, 143.5	130.35	145.07	128.38
1241A-15H-6, 125	136.20	150.92	133.56	Tie to 1241C-11H-2, 85	136.35	150.92	133.56
1241C-11H-7, 20	143.20	157.77	139.62	Tie to 1241A-16H-4, 7	141.52	157.77	139.62
1241A-16H-6, 95	145.41	161.66	143.06	Tie to 1241B-16H-2, 30	145.16	161.66	143.06
1241B-16H-6, 65	151.50	168.00	148.67	Tie to 1241A-17H-4, 24	151.16	168.00	148.67
1241A-17H-6, 145	155.35	172.19	152.38	Tie to 1241B-17H-1, 138.5	154.29	172.19	152.38
1241B-17H-4, 140	158.80	176.70	156.37	Tie to 1241A-18H-2, 104	158.46	176.70	156.37
1241A-18H-6, 100	164.44	182.68	161.66	Tie to 1241B-18H-1, 128.5	163.69	182.68	161.66
1241B-18H-5, 85	169.25	188.24	166.58	Tie to 1241A-19H-3, 53.5	168.96	188.24	166.58
1241A-19H-6, 140	174.30	193.58	171.31	Tie to 1241B-19H-2, 2.5	173.45	193.58	171.31
1241B-19H-4, 35	176.75	196.88	174.23	Tie to 1241A-20H-1, 110	176.00	196.88	174.23
1241A-20H-6, 120	183.65	204.53	181.00	Tie to 1241B-20H-2, 55	183.45	204.53	181.00
1241B-20H-4, 100	186.90	207.98	184.05	Tie to 1241A-21H-1, 145	185.85	207.98	184.05
1241A-21H-6, 10	192.05	214.18	189.54	Tie to 1241B-21H-2, 30	192.70	214.18	189.54
1241B-21H-5, 135	198.25	219.73	194.45	Tie to 1241A-22H-2, 105	196.44	219.73	194.45
1241A-22H-6, 105	202.47	225.76	199.79	Tie to 1241B-22H-3, 45	203.85	225.76	199.79
1241B-22H-6, 50	208.40	230.31	203.81	Tie to 1241A-23H-1, 150	204.91	230.31	203.81
1241A-23H-5, 140	210.84	236.24	209.06	Tie to 1241B-23H-3, 18.5	213.09	236.24	209.06
1241B-23H-6, 80	218.20	241.35	213.58	Tie to 1241A-24H-1, 130	214.20	241.35	213.58
1241A-24H-5, 105	219.99	247.14	218.71	Tie to 1241B-24H-3, 40	222.80	247.14	218.71
1241B-24H-6, 55	227.45	251.79	222.82	Tie to 1241A-25H-1, 55	222.95	251.79	222.82
1241A-25H-7, 35	231.83	260.67	230.68	Tie to 1241B-25H-5, 33.5	235.24	260.67	230.68
1241B-25H-6, 130	237.70	263.13	232.86	Tie to 1241A-26H-1, 120	233.10	263.13	232.86
1241A-26H-4, 110	237.50	267.53	236.75	Tie to 1241B-26H-2, 112	241.03	267.53	236.75
1241B-26H-6, 100	246.90	273.40	241.95	Tie to 1241A-27H-1, 95	242.35	273.40	241.95
1241A-27H-6, 70	249.60	280.65	248.36	Tie to 1241B-27H-4, 47.5	252.90	280.65	248.36
1241B-27H-7, 15	257.05	284.80	252.04	Tie to 1241A-28H-1, 145	252.35	284.80	252.04
1241A-28H-5, 105	257.95	290.40	256.99	Tie to 1241B-28X-2, 105	261.95	290.40	256.99
1241B-28X-5, 125	266.65	295.10	261.15	Tie to 1241A-29H-1, 150	261.91	295.10	261.15
1241A-29H-7, 45	269.87	303.06	268.19				

Note: This table is also available in [ASCII](#).

Table T4. OSUS-MS measurements, Hole 1241A.

Core, section, interval (cm)	Depth (mbsf)	Magnetic susceptibility (instrument units)	Run number	Depth from top of core (cm)
202-1241A-				
1H-1, 5	0.05	0.35	2202	5
1H-1, 10	0.10	0.40	2202	10
1H-1, 15	0.15	0.45	2202	15
1H-1, 20	0.20	0.50	2202	20
1H-1, 25	0.25	0.55	2202	25
1H-1, 30	0.30	0.60	2202	30
1H-1, 35	0.35	0.65	2202	35
1H-1, 40	0.40	0.70	2202	40
1H-1, 45	0.45	0.75	2202	45
1H-1, 50	0.50	0.80	2202	50
1H-1, 55	0.55	0.85	2202	55
1H-1, 60	0.60	0.90	2202	60
1H-1, 65	0.65	0.95	2202	65
1H-1, 70	0.70	1.00	2202	70
1H-1, 75	0.75	1.05	2202	75
1H-1, 80	0.80	1.10	2202	80
1H-1, 85	0.85	1.15	2202	85
1H-1, 90	0.90	1.20	2202	90
1H-1, 95	0.95	1.25	2202	95
1H-1, 100	1.00	1.30	2202	100
1H-1, 105	1.05	1.35	2202	105
1H-1, 110	1.10	1.40	2202	110
1H-1, 115	1.15	1.45	2202	115
1H-1, 120	1.20	1.50	2202	120
1H-1, 125	1.25	1.55	2202	125
1H-1, 130	1.30	1.60	2202	130
1H-1, 135	1.35	1.65	2202	135
1H-1, 140	1.40	1.70	2202	140
1H-1, 145	1.45	1.75	2202	145
1H-2, 5	1.55	1.85	2203	154
1H-2, 10	1.60	1.90	2203	159
1H-2, 15	1.65	1.95	2203	164
1H-2, 20	1.70	2.00	2203	169
1H-2, 25	1.75	2.05	2203	174
1H-2, 30	1.80	2.10	2203	179
1H-2, 35	1.85	2.15	2203	184
1H-2, 40	1.90	2.20	2203	189
1H-2, 45	1.95	2.25	2203	194
1H-2, 50	2.00	2.30	2203	199
1H-2, 55	2.05	2.35	2203	204
1H-2, 60	2.10	2.40	2203	209
1H-2, 65	2.15	2.45	2203	214
1H-2, 70	2.20	2.50	2203	219
1H-2, 75	2.25	2.55	2203	224
1H-2, 80	2.30	2.60	2203	229
1H-2, 85	2.35	2.65	2203	234
1H-2, 90	2.40	2.70	2203	239
1H-2, 95	2.45	2.75	2203	244
1H-2, 100	2.50	2.80	2203	249
1H-2, 105	2.55	2.85	2203	254
1H-2, 110	2.60	2.90	2203	259
1H-2, 115	2.65	2.95	2203	264
1H-2, 120	2.70	3.00	2203	269
1H-2, 125	2.75	3.05	2203	274
1H-2, 130	2.80	3.10	2203	279
1H-2, 135	2.85	3.15	2203	284
1H-2, 140	2.90	3.20	2203	289
1H-3, 5	3.05	3.35	2204	303
1H-3, 10	3.10	3.40	2204	308
1H-3, 15	3.15	3.45	2204	313
1H-3, 20	3.20	3.50	2204	318
1H-3, 25	3.25	3.55	2204	323
1H-3, 30	3.30	3.60	2204	328

Note: Only a portion of this table appears here. The complete table is available in [ASCII](#).

Table T5. OSUS-MS measurements, Hole 1241B.

Core, section, interval (cm)	Depth (mbsf)	Magnetic susceptibility (instrument units)	Run number	Depth from top of core (cm)
202-1241B-				
1H-1, 5	0.05	0.05	12.8	2375
1H-1, 10	0.10	0.10	15.9	2375
1H-1, 15	0.15	0.15	16.7	2375
1H-1, 20	0.20	0.20	17.5	2375
1H-1, 25	0.25	0.25	18.3	2375
1H-1, 30	0.30	0.30	14.4	2375
1H-1, 35	0.35	0.35	11.9	2375
1H-1, 40	0.40	0.40	7.1	2375
1H-1, 45	0.45	0.45	4.3	2375
1H-1, 50	0.50	0.50	5.5	2375
1H-1, 55	0.55	0.55	5.5	2375
1H-1, 60	0.60	0.60	5.6	2375
1H-1, 65	0.65	0.65	5.1	2375
1H-1, 70	0.70	0.70	5.0	2375
1H-1, 75	0.75	0.75	5.2	2375
1H-1, 80	0.80	0.80	6.0	2375
1H-1, 85	0.85	0.85	7.6	2375
1H-1, 90	0.90	0.90	7.8	2375
1H-1, 95	0.95	0.95	8.1	2375
1H-1, 100	1.00	1.00	7.0	2375
1H-1, 105	1.05	1.05	6.0	2375
1H-1, 110	1.10	1.10	5.5	2375
1H-1, 115	1.15	1.15	5.5	2375
1H-1, 120	1.20	1.20	5.4	2375
1H-1, 125	1.25	1.25	6.2	2375
1H-1, 130	1.30	1.30	8.8	2375
1H-1, 135	1.35	1.35	10.2	2375
1H-1, 140	1.40	1.40	10.1	2375
1H-1, 145	1.45	1.45	9.4	2375
1H-2, 5	1.55	1.55	11.6	2376
1H-2, 10	1.60	1.60	12.6	2376
1H-2, 15	1.65	1.65	12.8	2376
1H-2, 20	1.70	1.70	12.3	2376
1H-2, 25	1.75	1.75	13.1	2376
1H-2, 30	1.80	1.80	18.6	2376
1H-2, 35	1.85	1.85	13.1	2376
1H-2, 40	1.90	1.90	12.1	2376
1H-2, 45	1.95	1.95	12.6	2376
1H-2, 50	2.00	2.00	12.1	2376
1H-2, 55	2.05	2.05	11.4	2376
1H-2, 60	2.10	2.10	11.0	2376
1H-2, 65	2.15	2.15	12.1	2376
1H-2, 70	2.20	2.20	13.8	2376
1H-2, 75	2.25	2.25	16.1	2376
1H-2, 80	2.30	2.30	16.7	2376
1H-2, 85	2.35	2.35	17.3	2376
1H-2, 90	2.40	2.40	18.8	2376
1H-2, 95	2.45	2.45	20.9	2376
1H-2, 100	2.50	2.50	24.2	2376
1H-2, 105	2.55	2.55	26.9	2376
1H-2, 110	2.60	2.60	21.3	2376
1H-2, 115	2.65	2.65	18.3	2376
1H-2, 120	2.70	2.70	10.9	2376
1H-2, 125	2.75	2.75	6.2	2376
1H-2, 130	2.80	2.80	5.1	2376
1H-2, 135	2.85	2.85	5.7	2376
1H-2, 140	2.90	2.90	5.8	2376
1H-2, 145	2.95	2.95	5.6	2376
1H-3, 5	3.05	3.05	8.4	2377
1H-3, 10	3.10	3.10	9.3	2377
1H-3, 15	3.15	3.15	10.9	2377
1H-3, 20	3.20	3.20	11.5	2377
1H-3, 25	3.25	3.25	13.9	2377

Note: Only a portion of this table appears here. The complete table is available in [ASCII](#).

Table T6. OSUS-MS measurements, Hole 1241C.

Core, section, interval (cm)	Depth (mbsf)	Magnetic susceptibility (instrument units)	Run number	Depth from top of core (cm)
202-1241C-				
1H-1, 5	0.05	0.10	2583	5
1H-1, 10	0.10	0.15	2583	10
1H-1, 15	0.15	0.20	2583	15
1H-1, 20	0.20	0.25	2583	20
1H-1, 25	0.25	0.30	2583	25
1H-1, 30	0.30	0.35	2583	30
1H-1, 35	0.35	0.40	2583	35
1H-1, 40	0.40	0.45	2583	40
1H-1, 45	0.45	0.50	2583	45
1H-1, 50	0.50	0.55	2583	50
1H-1, 55	0.55	0.60	2583	55
1H-1, 60	0.60	0.65	2583	60
1H-1, 65	0.65	0.70	2583	65
1H-1, 70	0.70	0.75	2583	70
1H-1, 75	0.75	0.80	2583	75
1H-1, 80	0.80	0.85	2583	80
1H-1, 85	0.85	0.90	2583	85
1H-1, 90	0.90	0.95	2583	90
1H-1, 95	0.95	1.00	2583	95
1H-1, 100	1.00	1.05	2583	100
1H-1, 105	1.05	1.10	2583	105
1H-1, 110	1.10	1.15	2583	110
1H-1, 115	1.15	1.20	2583	115
1H-1, 120	1.20	1.25	2583	120
1H-1, 125	1.25	1.30	2583	125
1H-1, 130	1.30	1.35	2583	130
1H-1, 135	1.35	1.40	2583	135
1H-1, 140	1.40	1.45	2583	140
1H-1, 145	1.45	1.50	2583	145
1H-2, 5	1.55	1.60	2584	155
1H-2, 10	1.60	1.65	2584	160
1H-2, 15	1.65	1.70	2584	165
1H-2, 20	1.70	1.75	2584	170
1H-2, 25	1.75	1.80	2584	175
1H-2, 30	1.80	1.85	2584	180
1H-2, 35	1.85	1.90	2584	185
1H-2, 40	1.90	1.95	2584	190
1H-2, 45	1.95	2.00	2584	195
1H-2, 50	2.00	2.05	2584	200
1H-2, 55	2.05	2.10	2584	205
1H-2, 60	2.10	2.15	2584	210
1H-2, 65	2.15	2.20	2584	215
1H-2, 70	2.20	2.25	2584	220
1H-2, 75	2.25	2.30	2584	225
1H-2, 80	2.30	2.35	2584	230
1H-2, 85	2.35	2.40	2584	235
1H-2, 90	2.40	2.45	2584	240
1H-2, 95	2.45	2.50	2584	245
1H-2, 100	2.50	2.55	2584	250
1H-2, 105	2.55	2.60	2584	255
1H-2, 110	2.60	2.65	2584	260
1H-2, 115	2.65	2.70	2584	265
1H-2, 120	2.70	2.75	2584	270
1H-2, 125	2.75	2.80	2584	275
1H-2, 130	2.80	2.85	2584	280
1H-2, 135	2.85	2.90	2584	285
1H-2, 140	2.90	2.95	2584	290
1H-2, 145	2.95	3.00	2584	295
1H-3, 5	3.06	3.11	2585	305
1H-3, 10	3.11	3.16	2585	310
1H-3, 15	3.16	3.21	2585	315
1H-3, 20	3.21	3.26	2585	320
1H-3, 25	3.26	3.31	2585	325

Note: Only a portion of this table appears here. The complete table is available in [ASCII](#).

Table T7. Lithologic Unit I, Site 1241.

Unit/ Subunit	Top			Base			Description	Interpretation
	Hole, core, section, interval (cm)	Depth (mbsf)	(mcd)	Hole, core, section, interval (cm)	Depth (mbsf)	(mcd)		
IA	202-			202-			Clayey foraminifer-nannofossil ooze, cyclic variability in physical properties	Pelagic sedimentation, comparatively high terrigenous contribution, orbital cyclicity
	1241A-1H-1, 0	0.00	0.30	1241A-6H-3, 47	45.38	51.55		
	1241B-1H-1, 0	0.00	0.00	1241B-6H-2, 57	48.48	51.55		
IB	1241C-1H-1, 0	0.00	0.05	1241C-2H-CC, 20	41.87	46.14	Nannofossil ooze, very homogeneous	Pelagic sedimentation, moderate biogenic production
	1241A-6H-3, 47	45.38	51.55	1241A-31H-3, 74	283.16	318.44		
	1241B-6H-2, 57	48.48	51.55	1241B-30X-5, 70	285.41	318.44		
IC	1241C-3H-1, 0	47.50	53.69	1241C-11H-CC, 23	143.89	158.46	Clay diatom-bearing nannofossil ooze, laminated diatom ooze near the base	Pelagic sedimentation, high biogenic production
	1241A-31H-3, 74	283.16	318.44	1241A-43X-CC, 39	393.68	447.06		
	1241B-30X-5, 70	285.41	318.44	1241B-32X-CC, 31	306.97	345.26		

Table T8. Ash layers, Site 1241. (See table notes. Continued on next page.)

Number	Core, section, interval (cm)	Depth (mcd)		Core, section, interval (cm)	Depth (mcd)		Core, section, interval (cm)	Depth (mcd)		Glass color
		Top	Bottom		Top	Bottom		Top	Bottom	
202-1241A-										
1	1H-2, 9–15	1.89	1.95	1H-2, 22–34	1.72	1.84	1H-2, 24–30	1.79	1.85	Clear >> brown
2	Core gap			1H-5, 65–79	6.66	6.80	ND			Clear >> brown
3	2H-6, 124–135	13.59	13.70	2H-4, 64–76	13.62	13.74	ND			Clear
4	3H-3, 87–90	19.03	19.06	Core gap			ND			Clear > brown
5	3H-4, 27–36	19.93	20.02	3H-1, 54–55	19.91	19.92	ND			Clear
6	Core gap			3H-6, 82–83	27.66	27.67	ND			Brown
7	4H-3, 120–125	31.05	31.10	4H-2, 44–52	30.82	30.90	ND			Pumice (lapilli size) patch
8	4H-4, 11–14	31.46	31.49	4H-2, 88–97	31.26	31.35	ND			Clear >> brown
9	5H-4, 123–133	42.88	42.98	5H-3, 35–40	42.88	42.93	ND			Pumice (lapilli size) layer
10	5H-5, 13–18	43.29	43.34	5H-3, 71–75	43.24	43.28	ND			Pumice (lapilli size) layer
11	5H-5, 97–117	44.13	44.33	5H-4, 6–21	44.10	44.25	2H-6, 32–48	44.09	44.25	Clear
12	5H-6, 137–148	46.05	46.16	5H-5, 35–42	45.89	45.96	2H-CC, 12–20	45.99	46.07	Clear
13	5H-7, 23–33	46.41	46.51	5H-5, 68–73	46.22	46.27	ND			Clear
14	Core gap			5H-6, 94–101	47.99	48.06	ND			Clear
15	6H-1, 1–6	48.08	48.13	5H-6, 111–114	48.16	48.19	ND			Clear >> brown
16	6H-1, 53–55	48.60	48.62	5H-7, 10–14	48.65	48.69	ND			Pumice (lapilli size) layer
17	6H-1, 71–79	48.78	48.86	5H-7, 30–39	48.85	48.94	ND			Clear >> brown
18	NF			6H-1, 7–9	49.55	49.57	ND			Andesite (3 cm)
19	6H-3, 45–47	51.53	51.55	6H-2, 57–60	51.56	51.59	ND			Clear
20	6H-3, 130–138	52.38	52.46	6H-2, 144–149	52.43	52.48	ND			Clear >> brown
21	8H-5/6, (5)147–(6)1	77.10	77.14	8H-5, 41–43	77.08	77.10	5H-2, 44–50	76.99	77.05	Clear
22	11H-1, 12–14	101.32	101.34	NF			ND			Clear
23	NF			NF			10H-1, 39–40	135.69	135.71	Clear
24	15H-5, 87–92	149.03	149.08	15H-1, 28–31	149.05	149.08	11H-1, 47–49	149.04	149.06	Clear
25	NF			NF			11H-2, 20–23	150.27	150.3	Clear >> brown
26	19H-4, 52–57	189.73	189.78	18H-6, 81–86	189.74	189.79	ND			Brown
27	19H-7, 20–28	193.94	194.02	19H-2, 36–44	193.89	193.97	ND			Clear
28	NF			20H-7, 100	211.41	ND				Pumice (1 cm)
29	22H-1, 15–21	217.34	217.40	21H-4, 25–33	217.16	217.24	ND			Brown > clear
30	23H-5, 70–80	235.54	235.64	23H-2, 97–103	235.52	235.58	ND			Brown > clear
31	NF			23H-5, 64	239.69	ND				Scoria (3 mm)
32	NF			24H-1, 138	245.12	ND				Scoria (3 mm)
33	25H-7, 58–65	260.90	260.97	25H-5, 52–57	260.89	260.94	ND			Clear >> brown
34	26H-2, 0–6	263.44	263.50	25H-7, 7–15	263.45	263.53	ND			Scoria (sand size)
35	26H-2/3, (2)146–(3)3	264.90	264.98	26H-1, 0–5	264.90	264.95	ND			Brown
36	Core gap			28X-4, 61–62	292.99	293.00	ND			?
37	30H-1, 45–46	304.69	304.70	29X-4, 20–22	304.44	304.46	ND			Brown
38	30H-2, 64–68	306.38	306.42	29X-5, 52–67	306.26	306.41	ND			Clear > brown
39	30H-6, 69–71	312.47	312.49	NF			ND			Clear >> brown
40	30H-6, 76–77	312.54	312.55	NF			ND			Clear > brown
41	31H-3, 41	318.11	ND	NF			ND			Scoria (4 mm)
42	31H-3, 73–74	318.43	318.44	30X-5, 68–70	318.41	318.43	ND			Brown
43	31H-3, 82–83	318.52	318.53	NF			ND			Brown
44	31H-4, 34	319.55	ND	NF			ND			Scoria (4 mm)
45	31H-4, 43–45	319.64	319.66	30X-6, 33–41	319.56	319.64	ND			Clear
46	31H-5, 29–32	321.01	321.04	30X-7, 24–26	320.77	320.79	ND			Clear
47	31H-5, 99	321.71	ND	NF			ND			Scoria (7 mm)
48	32H-6, 123–125	335.97	335.99	Core gap			ND			Brown
49	32H-6, 135–136	336.09	336.10	Core gap			ND			Brown
50	32H-7, 53–54	336.77	336.78	32X-1, 45–54	336.74	336.83	ND			Brown
51	33H-2, 133–141	342.62	342.70	32X-5, 31–40	342.60	342.69	ND			Brown
52	34H-3, 128–130	354.81	354.83	ND			ND			Brown > clear
53	34H-6, 47–52	358.50	358.55	ND			ND			Clear >> brown
54	35X-6, 64–67	365.79	365.82	ND			ND			Clear >> brown
55	36X-3, 12–15	370.94	370.97	ND			ND			Brown
56	36X-3, 32–50	371.14	371.32	ND			ND			Brown > clear
57	36X-3, 84–88	371.66	371.70	ND			ND			?
58	36X-4, 35–37	372.67	372.69	ND			ND			?
59	38X-1, 44–45	390.06	390.07	ND			ND			Brown
60	38X-1, 54–55	390.16	390.17	ND			ND			?
61	38X-3, 25–27	392.67	392.69	ND			ND			Brown
62	39X-2, 105–107	402.91	402.93	ND			ND			Brown > clear
63	40X-6, 146–147	420.28	420.29	ND			ND			Clear
64	41X-1, 30–58	422.47	422.75	ND			ND			Brown
65	41X-1, 71–92	422.88	423.09	ND			ND			Brown
66	41X-1, 125–137	423.42	423.54	ND			ND			Brown
67	41X-2, 47–93	424.14	424.60	ND			ND			Brown

Table T8 (continued).

Number	Core, section, interval (cm)	Depth (mcd)		Core, section, interval (cm)	Depth (mcd)		Core, section, interval (cm)	Depth (mcd)		Glass color
		Top	Bottom		Top	Bottom		Top	Bottom	
68	41X-3, 130–140	426.47	426.57	ND			ND			?
69	41X-4, 28–33	426.95	427.00	ND			ND			?
70	41X-5, 22–26	428.39	428.43	ND			ND			Brown
71	42X-1, 13–26	433.26	433.39	ND			ND			Brown > clear

Notes: Ash layers that could be correlated between holes are located in the same row and printed in bold type. ND = not drilled, NF = not found. ? = unknown.

Table T9. Distribution of calcareous nannofossils, Holes 1241A and 1241C. ([See table notes](#). Continued on next page.)

Table T9 (continued).

Core, section, interval (cm)	Depth (mbsf)	Depth (mcd)	Preservation	Abundance	<i>Anaurolithus primus/delictus</i>	<i>Caleidiscus macintyrei</i>	<i>Ceratolithus armatus</i>	<i>Ceratolithus cristatus</i>	<i>Coccolithus micopelagicus</i>	<i>Discoaster bellus</i>	<i>Discoaster brouweri</i>	<i>Discoaster loeblichii</i>	<i>Discoaster neorectus</i>	<i>Discoaster pentaradiatus</i>	<i>Discoaster quinqueramus/berggrenii</i>	<i>Discoaster surculus</i>	<i>Discoaster tamalis</i>	<i>Discoaster variabilis</i> gr.	<i>Emiliania huxleyi</i>	<i>Gephyrocapsa</i> spp. (large)	<i>Gephyrocapsa</i> spp. (medium)	<i>Gephyrocapsa</i> spp. (small)	<i>Helicosphaera sellii</i>	<i>Pseudococcolithus lacunosa</i>	<i>Reticulofenestra asanoi</i>	<i>Reticulofenestra pseudoumbilicus</i> >7 µm
13H-CC, 13	118.07	131.66	M A	R						F	R	R	R	R		R								C	A	C
14H-CC, 18	127.84	142.01	M A	R R																				C C	A A	R C
15H-1, 75	128.15	142.87	M A	R R																				C C	A A	C C
15H-2, 75	129.66	144.38	M A	R R																				C C	A A	C C
15H-3, 75	131.17	145.89	M A	R						C	F	F	F	R									R A	F C	R A	
15H-CC, 9	137.35	152.07	G A	R						C	F	F	F	R									R A	C C	R A	
16H-3, 75	140.68	156.93	G A	R						C	F	F	F	R									R A	C C	R A	
16H-4, 75	142.19	158.44	G A	R						C	F	F	F	R									R A	C C	R A	
16H-5, 75	143.70	159.95	G A	R						C	F	F	F	R									R A	C C	R A	
16H-6, 75	145.21	161.46	G A	R						C	F	F	F	R									R A	C C	R A	
16H-7, 40	146.36	162.61	G A	R						C	F	F	F	R									R A	C C	R A	
16H-CC, 36	147.07	163.32	G A	R						C	F	F	F	R									R A	C C	R A	
17H-CC, 20	156.52	173.36	M A	R						F	F	F	F	R									R A	C C	R A	
18H-CC, 21	165.83	184.07	M A	R						F	F	F	F	R									R A	C C	R A	
19H-CC, 21	175.52	194.80	G A	R						F	F	F	F	R									R A	C C	R A	
20H-CC, 35	185.09	205.97	G A	R						F	F	F	F	R									R A	C C	R A	
21H-CC, 26	194.56	216.69	G A	R						C	F	F	F	R									R A	C C	R A	
22H-CC, 29	203.91	227.20	G A	R						F	F	F	F	R									R A	C C	R A	
23H-CC, 33	213.60	239.00	G A	R						C	F	F	F	R									R C	A F	R R	
24H-4, 75	218.18	245.33	G A							C	F	F	F	R									R C	C F	C F	
24H-5, 75	219.69	246.84	G A							C	F	F	F	R									R C	C F	C F	
24H-6, 75	221.19	248.34	G A							C	F	F	F	R									R C	C F	C F	
24H-CC, 8	222.78	249.93	G A							C	F	F	F	R									R C	A F	R R	
25H-CC, 22	232.53	261.37	M A							C	F	F	F	R									R C	A F	R C	
26H-CC, 20	241.90	271.93	M A							F	F	F	F	R									R C	A F	R C	
27H-CC, 1	251.31	282.36	M A							F	F	F	F	R									R C	A A	R A	
28H-1, 75	251.65	284.10	M A							F	F	R	R	R									R C	C C	R C	
28H-3, 75	254.65	287.10	M A							F	F	R	R	R									R C	C C	R C	
28H-5, 75	257.65	290.10	M A							F	F	R	R	R									R C	C C	R C	
28H-CC, 30	260.90	293.35	M A							F	F	R	R	R									R C	C C	R C	
29H-2, 75	262.66	295.85	M A							F	F	R	R	R									R C	C C	R C	
29H-3, 75	264.16	297.35	M A							F	F	R	R	R									R C	C C	R C	
29H-4, 75	265.67	298.86	M A							F	F	R	R	R									R C	C C	R C	
29H-5, 75	267.17	300.36	M A							F	F	R	R	R									R C	C C	R C	
29H-6, 75	268.67	301.86	M A							F	F	R	R	R									R C	C C	R C	
29H-7, 40	269.82	303.01	M A							F	F	R	R	R									R C	C C	R C	
29H-CC, 1	269.96	303.15	M A							F	F	R	R	R									R C	A A	R C	
30H-4, 75	275.17	309.51	M A							F	F	R	R	R									R C	A A	R C	
30H-6, 75	278.19	312.53	M A							F	F	R	R	R									R C	A A	R C	
30H-7, 40	279.35	313.69	M A							F	F	R	R	R									R C	A A	R C	
30H-CC, 24	279.99	314.33	M A							F	F	R	R	R									R R	A C	R R	
31H-1, 75	280.15	315.43	M A							F	F	R	R	R									C C	C C	C C	
31H-CC, 24	289.34	324.62	M A							C	F	R	R	R									C C	C C	C C	
32H-CC, 22	298.82	337.16	M A							F	F	R	R	R									C C	C C	C C	
33H-CC, 23	308.17	349.56	M A							F	F	R	R	R									C C	C C	C C	
34H-CC, 21	317.73	360.36	M A							F	F	R	R	R									C C	C C	C C	
35X-CC, 40	323.98	367.43	M A							F	F	R	R	R									C C	C F	C R	
36X-CC, 29	332.93	377.55	M A							F	F	R	R	R									C C	A C	C C	
37X-CC, 40	342.72	388.60	P A							F	F	R	R	R									C C	C C	C C	
38X-CC, 19	346.13	393.25	P A							R	F	R	R	R									C C	C C	C C	
39X-4, 75	357.25	405.61	M A							F	F	R	R	R									C C	C C	C C	
39X-5, 75	358.75	407.11	M A							R	F	R	R	R									C C	C C	C C	
39X-6, 75	360.25	408.61	M A							R	F	R	R	R									C C	C C	C C	
39X-CC, 16	360.85	409.21	P A							R	F	R	R	R									C C	F	C C	
40X-CC, 30	371.47	421.09	M A							F	F	R	R	R									A F	C F	A F	
41X-CC, 26	377.99	428.86	M A							R	F	R	R	R									C F	C F	A F	
42X-CC, 1	390.50	442.63	M A							F	F	R	R	R									A F	C F	A F	
43X-CC, 0	393.29	446.67	M A							F	F	R	R	R									C F	C F	C F	

Notes: Preservation: G = good, M = moderate, P = poor. Abundance: A = abundant, C = common, F = few, R = rare.

Table T10. Age-depth control points, Hole 1241A. (See table notes. Continued on next page.)

Datum	Source	Age (Ma)		Top sample (FO presence/LO absence)		Bottom sample (LO presence/FO absence)		Age (Ma)		Depth		
		Minimum	Maximum	Core, section, interval (cm)	Depth (mbsf)	Core, section, interval (cm)	Depth (mbsf)	Average	Uncertainty (±)	Average (mbsf)	Average (mcd)	Uncertainty (±m)
LO <i>Globigerinoides ruber</i> pink	PF	0.12	0.12	202-1241A-		202-1241A-				1.90	2.05	1.90
FO <i>Globigerinoides ruber</i> pink	PF	0.40	0.40	2H-CC, 1	13.53	3H-CC, 1	23.01	0.40	0.00	18.27	19.62	4.74
FO <i>Globorotalia flexuosa</i>	PF	0.40	0.40	2H-CC, 1	13.53	3H-CC, 1	23.01	0.40	0.00	18.27	19.62	4.74
LO <i>Pseudoemiliania lacunosa</i>	CN	0.46	0.46	2H-3, 75	7.65	2H-4, 75	9.15	0.46	0.00	8.40	9.35	0.75
LO <i>Stilostomella</i> spp.	PF	0.65	0.65	2H-CC, 1	13.53	3H-CC, 1	23.01	0.65	0.00	18.27	19.62	4.74
LO <i>Reticulofenestra asanoi</i>	CN	0.88	0.88	3H-3, 75	17.16	3H-4, 75	18.66	0.88	0.00	17.91	19.66	0.75
Reentry medium <i>Gephyrocapsa</i>	CN	1.02	1.02	3H-4, 75	18.66	3H-5, 75	20.16	1.02	0.00	19.41	21.16	0.75
LO <i>Rhizosolenia matuyamai</i>	D	1.05	1.05	3H-7, 40	22.83	3H-CC, 1	23.01	1.05	0.00	22.92	24.67	0.09
FO <i>Reticulofenestra asanoi</i>	CN	1.08	1.08	3H-5, 75	20.16	3H-6, 75	21.66	1.08	0.00	20.91	22.67	0.75
FO <i>Rhizosolenia matuyamai</i>	D	1.18	1.18	3H-CC, 1	23.01	4H-1, 75	23.65	1.18	0.00	23.33	26.18	0.32
LO <i>Gephyrocapsa</i> (large)	CN	1.24	1.24	3H-CC, 1	23.01	4H-1, 75	23.65	1.24	0.00	23.33	26.18	0.32
LO <i>Globigerinoides obliquus</i>	PF	1.30	1.30	3H-CC, 1	23.01	4H-CC, 1	32.57	1.30	0.00	27.79	30.64	4.78
FO <i>Gephyrocapsa</i> (large)	CN	1.45	1.45	4H-1, 75	23.65	4H-2, 75	25.15	1.45	0.00	24.40	28.34	0.75
LO <i>Neogloboquadrina acostaensis</i>	PF	1.58	1.58	4H-CC, 1	32.57	5H-CC, 1	42.22	1.58	0.00	37.40	41.73	4.83
LO <i>Calcidiscus macintyrei</i>	CN	1.59	1.59	4H-CC, 1	32.57	5H-1, 75	33.15	1.59	0.00	32.86	37.19	0.29
FO <i>Gephyrocapsa</i> (medium)	CN	1.67	1.67	5H-1, 75	33.15	5H-2, 75	34.67	1.67	0.00	33.91	38.63	0.76
LO <i>Globigerinoides fistulosus</i>	PF	1.77	1.77	4H-CC, 1	32.57	5H-CC, 1	42.22	1.77	0.00	37.40	41.73	4.83
LO <i>Globigerinoides extremus</i>	PF	1.77	1.77	4H-CC, 1	32.57	5H-CC, 1	42.22	1.77	0.00	37.40	41.73	4.83
FO <i>Fragilariopsis doliolus</i>	D	2.00	2.00	5H-CC, 1	42.22	6H-1, 10	42.00	1.89	0.11	42.11	47.56	-0.11
LO <i>Discoaster brouweri</i>	CN	1.96	1.96	6H-1, 75	42.65	6H-2, 75	44.16	1.96	0.00	43.41	49.58	0.76
FO <i>Globorotalia inflata</i>	PF	2.09	2.09	5H-CC, 1	42.22	6H-CC, 23	51.85	2.09	0.00	47.04	52.48	4.82
LO <i>Globorotalia exilis</i>	PF	2.15	2.15	5H-CC, 1	42.22	6H-CC, 23	51.85	2.15	0.00	47.04	52.48	4.82
LO <i>Globorotalia limbata</i>	PF	2.38	2.38	5H-CC, 1	42.22	6H-CC, 23	51.85	2.38	0.00	47.04	52.48	4.82
LO <i>Globorotalia puncticulata</i>	PF	2.40	2.40	6H-CC, 23	51.85	7H-CC, 10	61.28	2.40	0.00	56.57	63.17	4.72
LO <i>Thalassiosira convexa</i> s.l.	D	2.41	2.41	6H-CC, 1	51.95	7H-1, 130	52.70	2.41	0.00	52.33	58.77	0.38
LO <i>Discoaster pentaradiatus</i>	CN	2.44	2.44	7H-2, 75	53.66	7H-3, 75	55.17	2.44	0.00	54.42	61.45	0.76
LO <i>Globorotalia pertenuis</i>	PF	2.60	2.60	6H-CC, 23	51.85	7H-CC, 10	61.28	2.60	0.00	56.57	63.17	4.72
LO <i>Discoaster surculus</i>	CN	2.61	2.61	8H-4, 75	66.18	8H-5, 75	67.69	2.61	0.00	66.94	75.63	0.75
LO <i>Nitzschia jouseae</i>	D	2.77	2.77	7H-5, 77	58.19	7H-7, 27	60.70	2.77	0.00	59.45	66.48	1.26
LO <i>Dentoglobigerina altispira</i>	PF	3.09	3.09	7H-CC, 10	61.28	8H-CC, 32	71.00	3.09	0.00	66.14	74.00	4.86
LO <i>Sphaeroidinellopsis seminulina</i>	PF	3.09	3.09	7H-CC, 10	61.28	8H-CC, 32	71.00	3.09	0.00	66.14	74.00	4.86
FO <i>Rhizosolenia praebergonii</i> s.l.	D	3.17	3.17	8H-5, 48	67.42	8H-6, 133	69.77	3.17	0.00	68.60	77.29	1.18
LO <i>Globoquadrina baroemoenensis</i>	PF	3.22	3.22	8H-CC, 32	71.00	9H-CC, 1	80.22	3.22	0.00	75.61	84.78	4.61
FO <i>Globigerinoides fistulosus</i>	PF	3.33	3.33	8H-CC, 32	71.00	9H-CC, 1	80.22	3.33	0.00	75.61	84.78	4.61
LO <i>Sphenolithus</i> spp.	CN	3.65	3.65	10H-2, 75	82.15	10H-3, 75	83.65	3.65	0.00	82.90	93.62	0.75
LO <i>Reticulofenestra pseudoumbilicus</i>	CN	3.80	3.80	10H-CC, 35	89.96	11H-1, 75	90.15	3.80	0.00	90.06	101.32	0.10
FO <i>Thalassiosira convexa</i> v. <i>convexa</i>	D	3.81	3.81	11H-1, 30	89.70	11H-2, 30	91.21	3.81	0.00	90.46	102.26	0.75
LO <i>Globorotalia margaritae</i> common	PF	3.96	3.96	10H-CC, 35	89.96	11H-CC, 13	99.37	3.96	0.00	94.67	105.93	4.71
FO <i>Pseudoemiliania lacunosa</i>	CN	4.00	4.00	11H-3, 75	93.17	11H-4, 75	94.68	4.00	0.00	93.93	105.73	0.76
FO <i>Globorotalia exilis</i>	PF	4.45	4.45	12H-CC, 14	108.74	13H-CC, 13	118.07	4.45	0.00	113.41	126.80	4.67
FO <i>Globorotalia puncticulata</i>	PF	4.5	4.5	12H-CC, 14	108.74	13H-CC, 13	118.07	4.50	0.00	113.41	126.80	4.67
LO <i>Sphaeroidinellopsis kochi</i>	PF	4.53	4.53	11H-CC, 13	99.37	12H-CC, 14	108.74	4.53	0.00	104.06	116.56	4.69
FO <i>Ceratolithus cristatus</i>	CN	5.04	5.04	15H-2, 75	129.66	15H-3, 75	131.17	5.04	0.00	130.42	145.14	0.75
FO <i>Nitzschia jouseae</i>	D	5.12	5.12	12H-CC, 14	108.74	14H-CC, 13	127.84	5.12	0.00	118.29	131.95	9.55
FO <i>Ceratolithus armatus</i>	CN	5.34	5.34	16H-3, 75	140.68	16H-4, 75	142.19	5.34	0.00	141.44	157.69	0.75
LO <i>Globoquadrina dehisces</i>	PF	5.49	5.49	14H-CC, 18	127.84	15H-CC, 9	137.35	5.49	0.00	132.60	147.04	4.76

Table T10 (continued).

Datum	Source	Age (Ma)		Top sample (FO presence/LO absence)		Bottom sample (LO presence/FO absence)		Age (Ma)		Depth		
		Minimum	Maximum	Core, section, interval (cm)	Depth (mbsf)	Core, section, interval (cm)	Depth (mbsf)	Average	Uncertainty (±)	Average (mbsf)	Average (mcd)	Uncertainty (±m)
LO <i>Discoaster quinqueramus</i>	CN	5.56	5.56	16H-6, 75	145.21	16H-7, 40	146.36	5.56	0.00	145.79	162.04	0.58
FO <i>Globorotalia tumida</i>	PF	5.82	5.82	16H-CC, 36	147.07	17H-CC, 20	156.52	5.82	0.00	151.80	168.34	4.73
LO <i>Thalassiosira miocenica</i>	D	5.84	5.84	18H-5, 107	163.00	18H-CC, 21	165.83	5.84	0.00	164.42	182.66	1.42
LO <i>Nitzschia miocenica</i> s.s.	D	6.08	6.08	18H-CC, 21	165.83	20H-CC, 35	185.09	6.08	0.00	175.46	195.02	9.63
FO <i>Globorotalia margaritae</i>	PF	6.09	6.09	18H-CC, 21	165.83	19H-CC, 21	175.52	6.09	0.00	170.68	189.44	4.85
LO <i>Thalassiosira praecurvata</i>	D	6.18	6.18	19H-CC, 21	175.52	20H-CC, 35	185.09	6.18	0.00	180.31	200.39	4.79
FO <i>Globigerinoides conglobatus</i>	PF	6.2	6.2	21H-CC, 26	194.56	22H-CC, 29	203.91	6.20	0.00	199.24	221.95	4.68
LO <i>Rosselia praepaleasea</i>	D	6.54	6.54	22H-CC, 29	203.91	23H-CC, 33	213.60	6.54	0.00	208.76	233.10	4.85
FO <i>Thalassiosira miocenica</i>	D	6.55	6.55	21H-CC, 26	194.56	22H-CC, 29	203.91	6.55	0.00	199.24	221.95	4.68
FO <i>Thalassiosira convexa v. aspinosa</i>	D	6.57	6.57	21H-CC, 26	194.56	22H-CC, 33	203.91	6.57	0.00	199.24	221.97	4.68
FO <i>Thalassiosira praecurvata</i>	D	6.71	6.71	25H-3, 40	225.83	25H-4, 40	227.34	6.71	0.00	226.59	255.43	0.75
LO <i>Nitzschia miocenica</i> s.l.	D	7.30	7.30	25H-5, 40	228.85	25H-CC, 22	232.53	7.30	0.00	230.69	259.53	1.84
LO Absence interval <i>Reticulofenestra pseudoumbilicus</i> >7 µm	CN	6.80	6.80	24H-4, 75	218.18	24H-5, 75	219.69	6.80	0.00	218.94	246.09	0.75
FO <i>Discoaster surculus</i>	CN	7.80	7.80	27H-CC, 1	251.31	28H-1, 75	251.65	7.80	0.00	251.48	283.23	0.17
LO <i>Thalassiosira burckiana</i>	D	7.85	7.85	29H-5, 75	267.17	29H-6, 75	268.67	7.85	0.00	267.92	301.11	0.75
FO <i>Nitzschia cylindrica</i>	D	8.07	8.07	30H-3, 40	273.31	30H-4, 40	274.82	8.07	0.00	274.07	308.41	0.75
FO <i>Discoaster berggrenii</i>	CN	8.35	8.35	29H-2, 75	262.66	29H-3, 75	264.16	8.35	0.00	263.41	296.60	0.75
FO <i>Discoaster loeblichii</i>	CN	8.43	8.43	29H-7, 40	269.82	29H-CC, 1	269.96	8.43	0.00	269.89	303.08	0.07
FO <i>Globorotalia plesiotaumida</i>	PF	8.58	8.58	30H-CC, 24	279.99	31H-CC, 1	289.34	8.58	0.00	284.67	319.36	4.67
FO Absence interval <i>Reticulofenestra pseudoumbilicus</i> >7 µm	CN	8.85	8.85	30H-7, 40	279.35	30H-CC, 24	279.99	8.85	0.00	279.67	314.01	0.32
FO <i>Thalassiosira burckiana</i>	D	8.91	8.91	30H-CC, 28	280.03	31H-1, 40	279.80	8.91	0.00	279.92	314.73	-0.12
LO <i>Denticulopsis simonsenii</i>	D	9.45	9.45	33H-5, 82	305.22	33H-6, 43	306.33	9.45	0.00	305.78	347.17	0.55
FO <i>Neogloboquadrina acostaensis</i>	PF	9.82	9.82	32H-CC, 22	298.82	33H-CC, 23	308.17	9.82	0.00	303.50	343.36	4.68
FO <i>Globorotalia limbata</i>	PF	10.49	10.49	36X-CC, 29	332.93	37X-CC, 40	342.72	10.49	0.00	337.83	383.08	4.90
LO <i>Coccilithus miopelagicus</i>	CN	10.40	10.40	39X-4, 75	357.25	39X-5, 75	358.75	10.40	0.00	358.00	406.36	0.75
FO <i>Globoturborotalita nepenthes</i>	PF	11.19	11.19	40X-CC, 30	371.47	41X-CC, 26	377.99	11.19	0.00	374.73	424.98	3.26

Notes: FO = first occurrence, LO = last occurrence. CN = calcareous nannofossils, PF = planktonic foraminifers, D = diatoms.

Table T11. Distribution of major species of planktonic foraminifers, Hole 1241A. (See table notes. Continued on next three pages.)

Table T11 (continued).

Core, section, interval (cm)	Depth (mbsf)	Depth (mcd)	Preparation	Preservation	Abundance	Benthic/planktonic foraminifers (%)	Remarks	<i>Globoturborotalita decora</i> <i>Globoturborotalita nepenthes</i> <i>Neoglobotrivalva acostaensis</i> <i>Neogloboquadrina dutertrei</i> <i>Orbulina universa</i>	<i>Pulleytina obliquiloculata</i> <i>Pulleytina primalis</i> <i>Sphaeroidinella dehiscens</i> <i>Sphaerooidinellopsis kochii</i> <i>Sphaerooidinellopsis seminudina</i> <i>Stilostomella</i> spp.
202-1241A-Mudline	0.00	0.00	S P	A	1/99	Radiolarians: A		C F F C R F F F	
1H-CC, 1	3.80	4.10	S P/M	A	1/99	Radiolarians: R		F F F F R F F F	
2H-CC, 1	13.53	14.48	S M/G	A	1/99	Radiolarians: R		C C F R F F F F	
3H-CC, 1	23.01	24.76	S M	A	1/99	Radiolarians: R		F F C C F F F F	
4H-CC, 1	32.57	36.51	S M/G	A	1/99	Radiolarians: R		R C C F F F F F	
5H-CC, 1	42.22	46.94	S M/G	A	1/99	Radiolarians: R		F C C F F F F F	
6H-CC, 23	51.85	58.02	S M/G	A	1/99	Radiolarians: R		F C C F F F F F	
7H-CC, 10	61.28	68.31	S M/G	A	1/99	Radiolarians: F		F C C F F F F F	
8H-CC, 32	71.00	79.69	S M	A	1/99	Radiolarians: R		F C C F F F F F	
9H-CC, 1	80.22	89.86	S M	A	1/99	Radiolarians: F		F C C F F F F F	
10H-CC, 35	89.96	100.68	S M	A	1/99	Radiolarians: R		F C C F F F F F	
11H-CC, 13	99.37	111.17	S M	A	1/99	Radiolarians: F		F C C F F F F F	
12H-CC, 14	108.74	121.94	S M	A	1/99	Radiolarians: R		F F F F F F F F	
13H-CC, 13	118.07	131.66	S M/G	A	1/99	Radiolarians: R		R F F F F F F F	
14H-CC, 18	127.84	142.01	S M	A	1/99	Radiolarians: R		F F F R F F F F	
15H-CC, 9	137.35	152.07	S M	A	1/99	Radiolarians: R		R F F F F F F F	
16H-CC, 36	147.07	163.32	S M/G	A	1/99	Radiolarians: F		R F F F F F F F	
17H-CC, 20	156.52	173.36	S M	C	1/99	Radiolarians: F		F F F R F F F F	
18H-CC, 21	165.83	184.07	S M	C	1/99	Radiolarians: F		R F F F F F F F	
19H-CC, 21	175.52	194.80	S M	C	1/99	Radiolarians: C		F F F F F F F F	
20H-CC, 35	185.09	205.97	S M	C	5/95	Radiolarians: C		F F F F F F F F	
21H-CC, 26	194.56	216.69	S M	C	1/99	Radiolarians: A		R F F F F F F F	
22H-CC, 29	203.91	227.20	S M	F/C	15/85	Radiolarians: A		F F F F F F F F	
23H-CC, 33	213.60	239.00	S M	F/C	12/88	Radiolarians: A		F R R F F F F F	
24H-CC, 8	222.78	249.93	S M	F/C	10/90	Radiolarians: A		F R R F F F F F	
25H-CC, 22	232.53	261.37	S P/M	F/C	20/80	Radiolarians: A		R R R F F F F F	
26H-CC, 20	241.90	271.93	S M	F/C	20/80	Radiolarians: A		R R R F F F F F	
27H-CC, 1	251.31	282.36	S P/M	F/C	10/90	Radiolarians: A		F F F F F F F F	
28H-CC, 30	260.90	293.35	S M	F/C	10/90	Radiolarians: A		F F F F F F F F	
29H-CC, 1	269.96	303.15	S M	F/C	10/90	Radiolarians: A		F F F F F F F F	
30H-CC, 24	279.99	314.33	S M	F/C	10/90	Radiolarians: A		R F F F F F F F	
31H-CC, 24	289.34	324.62	S M	F	50/50	Radiolarians: A; Glauconite: R		R F F F F F F F	
32H-CC, 22	298.82	337.16	S M	F	95/5	Radiolarians: Ash: A; Glauconite: F		R R R F F F F F	
33H-CC, 23	308.17	349.56	C P/M	F	99/1	Radiolarians: A; Glauconite: C		R R R R F F F F	
34H-CC, 21	317.73	360.36	C P/M	R	99/1	Radiolarians: R; Ash: A; Glauconite F		R R R R R R R R	
35X-CC, 40	323.98	367.43	C P	R	99/1	Radiolarians: C; Ash: C; Glauconite: C	F		R R
36X-CC, 29	332.93	377.55	C M	F	99/1	Radiolarians: C; Ash: C; Glauconite: C	F R		R R
37X-CC, 40	342.72	388.60	C P/M	R	50/50	Radiolarians: C; Ash: R; Glauconite: R	F		R R
38X-CC, 19	346.13	393.25	C P	R	99/1	Radiolarians: C; Ash: F; Glauconite: C	F		R

Table T11 (continued).

Core, section, interval (cm)	Depth (mbsf)	Depth (mcd)	Preparation			Abundance	Benthic/planktonic foraminifers (%)	Remarks																								
			C	P	Preservation				Dentoglobigerina altispina	Globigerinella aequilateris	Globigerinoides conglobatus	Globigerinoides extremus	Globigerinoides fistulosus	Globigerinoides obliquus	Globigerinoides ruber	Globigerinoides ruber pink	Globigerinoides sacculifer	Globigerinoides trilobus	Globiquadrina barremensis	Globiquadrina dehisca	Globorotalia conoidea	Globorotalia crossula	Globorotalia exilis	Globorotalia flexuosa	Globorotalia inflata	Globorotalia juanai	Globorotalia limbata	Globorotalia margaritae	Globorotalia menardii	Globorotalia pertenuis	Globorotalia plesiotumida	Globorotalia pseudomicenica
39X-CC, 16	360.85	409.21	C	P	R	99/1																										
40X-CC, 30	371.47	421.09	C	P	R	25/75																										
41X-CC, 26	377.99	428.86	C	P	T/R																											
42X-CC, 1	390.50	442.63	C	P/M	F	50/50																										
43X-CC, 0	393.29	446.67	C	P	R	90/10																										

Notes: Preparation: S = smear slide, C = Calgon. Preservation: G = good, M = moderate, P = poor. Abundance: A = abundant, C = common, F = few, R = rare.

Table T11 (continued).

Core, section, interval (cm)	Depth (mbsf)	Depth (mcd)	Preparation				Remarks	Benthic/planktonic foraminifers (%)	
			Preservation	Abundance					
39X-CC, 16	360.85	409.21	C	P	R	99/1	<i>Globoturborotalita decora</i> <i>Globoturborotalita nepenthes</i> <i>Neoglobotrivalva acostaensis</i> <i>Neoglobotrivalva dutertrei</i> <i>Orbulina universa</i>		
40X-CC, 30	371.47	421.09	C	P	R	25/75			
41X-CC, 26	377.99	428.86	C	P	T/R				
42X-CC, 1	390.50	442.63	C	P/M	F	50/50	<i>Pulleniatina obliquiloculata</i> <i>Pulleniatina primalis</i> <i>Sphaeroidinella dehisca</i>		
43X-CC, 0	393.29	446.67	C	P	R	90/10	<i>Sphaerooidinellopsis kochii</i> <i>Sphaerooidinellopsis seminulina</i> <i>Stilostomella</i> spp.		

Table T12. Distribution of diatoms, Hole 1241A. (See table notes. Continued on next three pages.)

Table T12 (continued).

Core, section, interval (cm)	Depth (mbsf)	Depth (mcd)	Identification	Abundance	Preservation	Thalassiothrix spp.	Remarks							
202-1241A-														
Mudline	0.00	0.00	PAL	S F-C	P	F-C								
1H-CC, 1	3.79	4.10	PAL	S R	P-M	T								Ethmodiscus fragments
2H-CC, 1	13.52	14.48	PAL	S F	M	F								Presence of Grammatophora
3H-CC, 1	23.00	24.76	PAL	S F	M			R-F						Ethmodiscus fragments
4H-CC, 1	32.56	36.51	PAL	S F	P	R-F			F	R				Ethmodiscus fragments
5H-CC, 1	42.21	46.94	PAL	S F	P	F			F	F				Ethmodiscus fragments
6H-CC, 33	51.95	58.12	PAL	S F	P	R			F	F				Ethmodiscus fragments
7H-CC, 10	61.28	68.31	PAL	S F	P	F			F	F				Ethmodiscus fragments/Plagiogramma
8H-CC, 32	71.00	79.69	PAL	S C	P-M	F	T	F-C						
9H-CC, 0	80.21	89.85	PAL	S F	P-M					F				Ethmodiscus fragments
10H-CC, 35	89.96	100.68	PAL	S F	P-M				F	R-F				Ethmodiscus fragments
11H-CC, 13	99.37	111.17	PAL	S F	P				F	F				Ethmodiscus fragments
12H-CC, 14	108.74	121.94	PAL	S R-F	P									Ethmodiscus fragments
13H-CC, 13	118.07	131.66	PAL	S R	P				R	R				Ethmodiscus fragments
14H-CC, 18	127.84	142.01	PAL	S F	P-M				R	R-F				Ethmodiscus fragments
15H-CC, 9	137.35	152.07	PAL	S R-F	P				R	R-F				Ethmodiscus fragments
16H-CC, 36	147.07	163.32	PAL	S F	M		T		T	F				Ethmodiscus fragments
17H-CC, 20	156.52	173.36	PAL	S F	M			R-F	F-C					Presence of Grammatophora
18H-CC, 21	165.83	184.07	PAL	S F	M					F				Ethmodiscus fragments
19H-CC, 21	175.52	194.80	PAL	S C	M				C-A					
20H-CC, 35	185.09	205.97	PAL	S F	P				F					Presence of Pinnularia
21H-CC, 26	194.56	216.69	PAL	S C-A	M		T		C-A					Presence of Diploaneis
22H-CC, 29	203.91	227.20	PAL	S C-A	M		T		C					Presence of Diploaneis
23H-CC, 33	213.60	239.00	PAL	S C	M					F				
24H-CC, 8	222.78	249.93	PAL	S C	M		T		T	F-C				
25H-CC, 22	232.53	261.37	PAL	S C-A	M			R	C					Ethmodiscus fragments
26H-CC, 20	241.90	271.93	PAL	S F-C	M					T				
27H-CC, 1	251.30	282.36	PAL	S A	P-M			F	C-A					
28H-CC, 30	260.90	293.35	PAL	S F	P				F					Presence of Cocconeis, Paralia sulcata, and Grammatophora
29H-CC, 1	269.95	303.15	PAL	S F	P			R	F					
30H-CC, 24	279.99	314.33	PAL	S F	P			R-F	F					Presence of Plagiogramma
31H-CC, 24	289.34	324.62	PAL	S F-C	M		T	R	F-C					Presence of Cocconeis
32H-CC, 22	298.82	337.16	PAL	S C	M		R	F	C					
33H-CC, 23	308.17	349.56	PAL	S F-C	M			F	C					Thrix-Thema fragments dominated/Ethmodiscus fragments
34H-CC, 21	317.73	360.36	PAL	S C	M			F	R	F				Thrix-Thema fragments dominated/Ethmodiscus fragments
35X-CC, 40	323.98	367.43	PAL	S F-C	M			T	F	C				Thrix-Thema fragments dominated
36X-CC, 29	332.93	377.55	PAL	S F-C	M			T	R-F	F				Thrix-Thema fragments dominated

Table T12 (continued).

Core, section, interval (cm)	Depth (mbsf)	Depth (mcd)	Identification		Method	Abundance	Preservation	<i>Actinocyclus ellipticus</i>	<i>Actinocyclus ellipticus v. lanceolata</i>	<i>Actinocyclus moronensis</i>	<i>Actinocyclus spp.</i>	<i>Actiroptychus senarius</i>	<i>Asteromphalus</i> spp.	<i>Azpatia nodulifera</i>	<i>Chaetoceros</i> spp. (resting spores)	<i>Coscinodiscus</i> spp.	<i>Denticulopsis simonsenii</i> s.l.	<i>Fragilariopsis doliolus</i>	<i>Hemidiscus cuneiformis</i>	<i>Nitzschia cylindrica</i>	<i>Nitzschia fossilis</i>	<i>Nitzschia joueae</i>	<i>Nitzschia marina</i>	<i>Nitzschia miocenica</i>	<i>Nitzschia porteri</i>	<i>Nitzschia reinholdii</i>	<i>Rhizosolenia matuyamai</i>	<i>Rhizosolenia praebergonii</i> s.s.	<i>Rhizosolenia</i> spp.	<i>Rossiella praeapaleacea</i> s.l.	<i>Rossiella paleacea</i> s.l.	<i>Stephanopyxis</i> spp.	<i>Thalassionema</i> spp.	<i>Thalassiosira burkliana</i>	<i>Thalassiosira convexa</i>	<i>Thalassiosira convexa v. aspinosa</i>	<i>Thalassiosira miocenica</i>
			S	C-A	M	P	F-C	P-M	A	P-M	T	R	F	R	F	R	F	C	F	R	T	R	F	R	F	R	F	R	C	F	F-C	F-C	R				
37X-CC, 40	342.72	388.60	PAL	S	C-A	M		R				R	R	R				T																			
38X-CC, 19	346.13	393.25	PAL	S	F-C	P																															
39X-CC, 16	360.85	409.21	PAL	S	F-C	P-M																															
40X-CC, 30	371.47	421.09	PAL	S	A	P-M		T			R																										
41X-CC, 26	377.99	428.86	PAL	S	C	P-M																															
42X-CC, 1	390.49	442.63	PAL	S	F	P																															
43X-CC, 0	393.29	446.67	PAL	S	T	P																															

Notes: PAL = paleontology sample. S = smear slide. Abundance: A = abundant, C = common, F = few, R = rare, T = trace. Preservation: M = moderate, P = poor.

Table T12 (continued).

Core, section, interval (cm)	Depth (mbsf)	Depth (mcd)	ID	Method	Abundance	Preservation	Remarks		
							<i>Thalassocidiosa</i> spp.	<i>Thalassocidiosa</i> spp.	<i>Thalassocidiosa</i> spp.
37X-CC, 40	342.72	388.60	PAL	S	C-A	M	R	T	C
38X-CC, 19	346.13	393.25	PAL	S	F-C	P	R		F
39X-CC, 16	360.85	409.21	PAL	S	F-C	P-M	R	R	T
40X-CC, 30	371.47	421.09	PAL	S	A	P-M	R	T	
41X-CC, 26	377.99	428.86	PAL	S	C	P-M	R	T	F
42X-CC, 1	390.49	442.63	PAL	S	F	P	R		R
43X-CC, 0	393.29	446.67	PAL	S	T	P		T	T

Table T13. Headspace gas concentration, Hole 1241A.

Core, section, interval (cm)	Depth (mbsf)	Depth (mcd)	C ₁ (ppmv)
202-1241A-			
1H-3, 0-5	3.00	3.30	2.2
2H-4, 0-5	8.40	9.35	4.0
3H-4, 0-5	17.91	19.66	6.6
4H-4, 0-5	27.41	31.35	5.6
5H-4, 0-5	36.93	41.65	6.7
6H-4, 0-5	46.41	52.58	6.2
7H-4, 0-5	55.91	62.94	10.2
8H-4, 0-5	65.43	74.12	9.6
9H-4, 0-5	74.91	84.55	9.3
10H-4, 0-5	84.40	95.12	9.9
11H-4, 0-5	93.93	105.73	10.5
12H-4, 0-5	103.43	116.63	7.8
13H-4, 0-5	112.93	126.52	10.4
14H-4, 0-5	122.43	136.60	10.1
15H-4, 0-5	131.93	146.65	7.8
16H-4, 0-5	141.44	157.69	11.2
17H-4, 0-5	150.92	167.76	10.8
18H-4, 0-5	160.42	178.66	11.0
19H-4, 0-5	169.93	189.21	13.4
20H-4, 0-5	179.43	200.31	8.7
21H-4, 0-5	188.93	211.06	8.4
22H-4, 0-5	198.41	221.70	9.2
23H-4, 0-5	207.93	233.33	8.7
24H-4, 0-5	217.43	244.58	6.1
25H-4, 0-5	226.94	255.78	8.0
26H-4, 0-5	236.43	266.46	9.3
27H-4, 0-5	245.92	276.97	11.8
28H-4, 0-5	255.40	287.85	8.5
29H-4, 0-5	264.92	298.11	6.3
30H-4, 0-5	274.42	308.76	7.3
31H-4, 0-5	283.93	319.21	6.9
32H-4, 0-5	293.40	331.74	5.7
33H-4, 0-5	302.90	344.29	6.7
34H-4, 0-5	312.40	355.03	7.2
36X-4, 0-5	327.70	372.32	3.3
37X-4, 0-5	337.40	383.28	4.4
38X-2, 0-5	344.00	391.12	3.1
39X-4, 0-5	356.50	404.86	4.6
40X-4, 0-5	366.20	415.82	3.3
41X-4, 0-5	375.80	426.67	2.9
42X-4, 0-5	385.50	437.63	2.3
43X-2, 0-5	392.08	445.46	2.1

Table T14. Interstitial water geochemical data, Hole 1241A.

Core, section, interval (cm)	Depth		pH	Alkalinity (mM)	Salinity	Cl ⁻ (mM)	Na ⁺ (mM)	SO ₄ ²⁻ (mM)	HPO ₄ ²⁻ (μM)	NH ₄ ⁺ (μM)	H ₄ SiO ₄ (μM)	Mn ²⁺ (μM)	Fe ²⁺ (μM)	Ca ²⁺ (mM)	Mg ²⁺ (mM)	B (μM)	Sr ²⁺ (μM)	Ba ²⁺ (μM)	Li ⁺ (μM)	K ⁺ (mM)
	(mbsf)	(mcd)																		
202-1241A-																				
1H-2, 145-150	2.95	3.25	7.56	3.62	35.0	559	489	30.4	4.9	93	551	12.1	2.1	10.3	51.0	502	101	1.9	26	12.4
2H-3, 145-150	8.35	9.30	7.24	3.57	35.0	556	486	29.7	3.8	170	580	12.9	1.8	10.3	50.1	481	121	2.6	24	12.0
3H-3, 145-150	17.86	19.61	7.64	4.18	35.0	559	488	29.7	2.9	252	646	9.2	1.7	10.5	50.6	507	150	4.0	24	12.7
4H-3, 145-150	27.36	31.30	7.21	4.71	35.0	562	482	25.2	2.9	330	656	5.1	6.6	10.9	50.0	478	182	3.3	23	12.9
5H-3, 145-150	36.88	41.60	7.22	4.75	35.0	560	483	27.4	2.8	368	693	3.1	2.0	11.3	50.5	487	208	4.2	24	13.3
6H-3, 145-150	46.36	52.53	7.73	4.77	35.0	563	489	27.5	2.2	406	706	2.1	0.7	11.3	49.3	473	215	5.3	22	12.7
7H-3, 145-150	55.87	62.90	7.30	5.03	35.0	562	488	28.3	2.0	417	743	1.2	2.5	11.8	49.7	485	230	4.0	20	13.2
8H-3, 145-150	65.37	74.06	7.21	4.24	34.0	560	489	28.0	1.7	423	727	1.2	0.4	11.6	48.0	465	222	4.2	19	12.2
9H-3, 145-150	74.86	84.50	7.08	5.12	35.0	563	487	27.6	1.7	433	737	1.0	1.4	12.6	49.7	469	247	4.3	18	12.2
10H-3, 145-150	84.35	95.07	7.32	5.88	35.0	561	487	27.2	1.5	413	753	0.9	1.2	12.6	48.6	471	242	2.5	18	12.3
11H-3, 145-150	93.87	105.67	7.45	4.94	35.0	557	480	27.6	1.4	417	770	0.5	1.7	12.9	49.3	471	244	2.2	16	12.3
12H-3, 145-150	103.37	116.57	7.16	5.04	35.0	558	482	27.5	1.4	390	753	0.4	2.3	13.0	49.2	449	241	3.0	15	12.0
13H-3, 145-150	112.87	126.46	7.20	4.98	35.0	559	479	27.3	1.2	397	770	0.5	1.3	13.5	50.1	468	227	2.5	14	12.1
14H-3, 145-150	122.37	136.54	7.32	4.92	35.0	555	477	27.7	1.4	371	766	0.4	2.6	13.5	49.6	471	233	3.0	14	11.7
15H-3, 145-150	131.87	146.59	7.08	4.80	35.0	557	485	27.0	1.4	368	793	1.0	4.0	12.5	47.3	469	224	1.4	14	11.1
16H-3, 145-150	141.38	157.63	7.19	4.80	35.0	561	483	27.7	1.2	343	797	0.4	1.1	13.5	49.8	470	225	3.1	14	11.5
17H-3, 145-150	150.86	167.70	7.16	4.58	35.0	558	478	28.1	1.1	334	821	0.4	1.6	13.4	51.3	447	212	3.8	13	11.8
18H-3, 145-150	160.36	178.60	7.30	4.51	35.0	557	485	28.5	1.1	340	869	0.4	1.9	13.0	48.2	462	201	1.0	14	11.4
19H-3, 145-150	169.87	189.15	7.64	4.37	35.0	560	481	27.3	1.0	324	857	0.3	2.1	13.1	50.0	462	198	2.8	13	11.6
20H-3, 145-150	179.37	200.25	7.17	4.25	35.0	556	474	25.4	0.9	293	863	0.3	0.7	13.1	49.6	458	189	2.8	14	11.3
21H-3, 145-150	188.87	211.00	7.18	4.11	35.0	560	484	28.5	1.1	290	921	0.5	2.9	13.0	50.0	460	188	0.9	14	11.1
23H-3, 145-150	207.87	233.27	7.38	3.82	35.0	558	478	28.0	0.9	248	949	0.3	1.5	13.2	50.9	455	171	1.9	15	11.3
25H-3, 145-150	226.88	255.72	7.54	3.48	35.0	559	483	28.7	0.9	230	947	0.5	0.8	13.0	50.1	461	157	1.1	15	11.0
27H-3, 145-150	245.87	276.92	7.37	3.13	35.0	555	481	29.4	0.8	194	943	0.5	0.4	12.9	49.7	445	143	1.8	16	10.9
29H-3, 145-150	264.86	298.05	7.41	3.02	35.0	558	485	28.8	0.8	174	939	0.6	0.9	12.3	49.2	447	134	0.8	16	10.8
31H-3, 145-150	283.87	319.15	7.43	2.62	35.0	560	486	28.7	0.8	164	1051	1.2	0.8	12.4	48.7	446	120	3.3	17	11.4
33H-3, 145-150	302.85	344.24	7.73	2.06	35.0	561	486	29.6	0.8	156	1193	2.9	0.3	12.7	49.4	467	115	0.7	18	12.0
35X-3, 140-150	318.80	362.05	7.49	2.42	35.0	561	487	30.6	0.9	125	1015	3.9	0.2	13.1	49.8	439	105	2.6	18	11.6
36X-3, 140-150	327.60	372.22	7.35	2.66	35.0	560	466	27.1	0.9	107	1150	5.3	0.4	14.6	54.9	433	105	1.9	19	12.3
37X-3, 140-150	337.30	383.18	7.40	2.50	35.0	557	484	30.5	1.1	94	1152	5.6	0.1	13.5	49.2	425	101	2.1	20	11.0
38X-1, 140-150	343.90	391.02	7.47	2.66	35.0	554	480	31.1	1.0	81	1207	7.1	4.2	13.2	51.0	411	97	0.8	20	10.8
39X-3, 140-150	356.40	404.76	7.43	2.10	35.0	558	483	30.8	0.8	94	1032	9.5	0.3	13.1	50.3	415	93	0.6	20	11.4
40X-3, 140-150	366.10	415.72	7.47	2.10	35.0	561	483	31.0	0.8	70	1077	12.4	0.1	13.6	51.6	412	92	1.5	21	12.0
41X-4, 140-150	377.20	428.07	7.58	2.16	35.0	561	484	31.1	0.7	50	1230	15.2	0.0	13.9	50.9	407	91	1.7	23	11.3
42X-3, 140-150	385.40	437.53	7.47	2.11	35.0	559	479	29.7	0.5	46	941	19.3	0.4	13.6	51.7	424	89	0.6	22	11.2
43X-1, 138-148	391.98	445.36	8.09	1.45	35.0	559	485	31.3	BDL	31	469	14.8	0.1	13.1	49.9	349	85	1.8	22	11.9

Note: BDL = below detection limit (HPO₄²⁻ = 0.2 μM).

Table T15. Inorganic carbon, calcium carbonate, total carbon, total organic carbon, total organic carbon on a carbonate-free basis, and total nitrogen concentrations, and TOC/TN ratio, Hole 1241A. ([See table note](#). Continued on next page.)

Core, section, interval (cm)	Depth (mbsf) (mcd)		IC (wt%)	CaCO ₃ (wt%)	TC (wt%)	TOC (wt%)	TOC CFB (wt%)	TN (wt%)	TOC/TN (atomic)
202-1241A-									
1H-1, 74-75	0.74	1.04	7.76	64.7	8.49	0.73	2.07	0.127	4.93
1H-2, 74-75	2.24	2.54	6.58	54.8	6.78	0.20	0.45	0.044	3.99
1H-3, 20-21	3.20	3.50	7.65	63.7	8.20	0.55	1.52	0.098	4.85
2H-1, 74-75	4.64	5.59	7.55	62.9	8.08	0.53	1.44	0.058	7.86
2H-3, 74-75	7.64	8.59	7.57	63.0					
2H-5, 74-75	10.64	11.59	7.58	63.2	8.10	0.52	1.42	0.130	3.45
2H-7, 20-21	13.10	14.05	7.72	64.3					
3H-1, 74-75	14.14	15.89	8.31	69.3	8.72	0.41	1.34	0.051	6.90
3H-3, 74-75	17.15	18.90	8.03	66.9					
3H-5, 74-75	20.15	21.90	8.06	67.2	8.47	0.41	1.24	0.052	6.69
3H-7, 20-21	22.63	24.38	8.41	70.0					
4H-1, 74-75	23.64	27.58	8.25	68.8	8.66	0.41	1.33	0.052	6.81
4H-3, 74-75	26.65	30.59	8.87	73.9					
4H-5, 74-75	29.65	33.59	8.34	69.5	8.62	0.28	0.93	0.033	7.47
5H-1, 74-75	33.14	37.86	8.52	71.0	9.20	0.68	2.35	0.058	10.10
5H-3, 74-75	36.17	40.89	7.29	60.8					
5H-5, 74-75	39.18	43.90	6.53	54.4	6.87	0.34	0.74	0.042	6.92
6H-1, 8485	42.74	48.91	8.29	69.1	8.63	0.34	1.09	0.021	13.76
6H-3, 74-75	45.65	51.82	8.16	68.0					
6H-5, 74-75	48.65	54.82	9.34	77.8	9.73	0.39	1.77	0.028	12.18
7H-1, 74-75	52.14	59.17	8.29	69.0	8.59	0.30	0.97	0.016	16.12
7H-3, 74-75	55.16	62.19	8.14	67.8					
7H-5, 74-75	58.16	65.19	9.46	78.8	9.82	0.36	1.69	0.023	13.30
8H-1, 74-75	61.64	70.33	8.79	73.2	9.19	0.40	1.50	0.032	10.83
8H-3, 74-75	64.66	73.35	8.47	70.6					
8H-5, 74-75	67.68	76.37	8.89	74.1					
9H-1, 74-75	71.14	80.78	9.16	76.3	9.55	0.39	1.66	0.027	12.37
9H-3, 74-75	74.15	83.79	8.87	73.9					
9H-5, 74-75	77.15	86.79	9.76	81.3	10.11	0.35	1.90	0.016	19.05
10H-2, 74-75	82.14	92.86	9.85	82.0	10.14	0.29	1.62	0.013	19.91
10H-4, 74-75	85.14	95.86	9.92	82.6					
10H-6, 74-75	88.14	98.86	10.26	85.5					
11H-2, 74-75	91.65	103.45	9.98	83.1	10.28	0.30	1.80	0.014	19.05
11H-4, 74-75	94.67	106.47	9.56	79.6					
11H-6, 74-75	97.70	109.50	9.88	82.3					
12H-2, 74-75	101.15	114.35	10.09	84.0	10.35	0.26	1.65	0.008	28.76
12H-4, 74-75	104.17	117.37	10.40	86.6					
12H-6, 74-75	107.19	120.39	10.19	84.9					
13H-2, 74-75	110.65	124.24	10.41	86.7					
13H-4, 74-75	113.67	127.26	10.45	87.0					
13H-6, 74-75	116.68	130.27	10.37	86.4					
14H-2, 74-75	120.15	134.32	10.57	88.0	10.84	0.27	2.25		
14H-4, 74-75	123.17	137.34	10.24	85.3					
14H-6, 74-75	126.19	140.36	10.68	89.0					
15H-2, 74-75	129.65	144.37	10.37	86.4	10.56	0.19	1.39	0.008	20.71
15H-4, 74-75	132.67	147.39	10.54	87.8					
15H-6, 74-75	135.69	150.41	10.53	87.7					
16H-4, 74-75	142.18	158.43	10.43	86.9	10.67	0.24	1.86	0.009	23.83
16H-6, 74-75	145.20	161.45	9.37	78.1					
17H-2, 74-75	148.65	165.49	10.04	83.6	10.21	0.17	1.06	0.008	17.56
17H-4, 74-75	151.66	168.50	10.48	87.3					
17H-6, 74-75	154.67	171.51	10.46	87.1					
18H-2, 74-75	158.14	176.38	10.25	85.4	10.68	0.43	2.96	0.027	13.63
18H-4, 74-75	161.16	179.40	10.27	85.5					
18H-6, 74-75	164.18	182.42	9.91	82.5					
19H-2, 74-75	167.65	186.93	8.47	70.6	8.82	0.35	1.19	0.011	26.48
19H-4, 74-75	170.67	189.95	10.71	89.3	10.97	0.25	2.37		
19H-6, 74-75	173.69	192.97	10.19	84.9					
20H-2, 74-75	177.15	198.03	10.45	87.1	10.53	0.08	0.62	0.008	8.63
20H-4, 74-75	180.17	201.05	10.37	86.4	10.52	0.15	1.10	0.015	8.31
20H-6, 74-75	183.19	204.07	10.09	84.0					
21H-2, 74-75	186.65	208.78	10.65	88.7	10.77	0.12	1.06		
21H-4, 74-75	189.67	211.80	9.48	79.0	9.86	0.38	1.81	0.024	13.46
21H-6, 74-75	192.69	214.82	9.59	79.9					

Table T15 (continued).

Core, section, interval (cm)	Depth (mbsf) (mcd)		IC (wt%)	CaCO ₃ (wt%)	TC (wt%)	TOC (wt%)	TOC CFB (wt%)	TN (wt%)	TOC/TN (atomic)
22H-2, 74-75	196.13	219.42	9.97	83.1	10.07	0.10	0.59	0.007	12.84
22H-4, 74-75	199.15	222.44	8.93	74.4	9.15	0.22	0.86	0.015	12.36
22H-6, 74-75	202.16	225.45	9.80	81.7					
23H-1, 74-75	204.14	229.54	8.93	74.4	9.00	0.07			
23H-3, 74-75	207.16	232.56	9.05	75.4	9.27	0.22	0.89	0.008	24.49
23H-6, 74-75	211.69	237.09	10.24	85.3					
24H-2, 74-75	215.15	242.30	9.81	81.7	9.89	0.08	0.44	0.007	10.39
24H-4, 74-75	218.17	245.32	8.75	72.9	9.00	0.25	0.92	0.010	21.36
24H-6, 74-75	221.18	248.33	9.78	81.5					
25H-2, 74-75	224.65	253.49	9.29	77.4	9.33	0.04	0.18	0.002	16.97
25H-4, 74-75	227.68	256.52	8.78	73.1	8.87	0.09	0.33	0.007	11.40
25H-6, 74-75	230.71	259.55	8.94	74.5					
26H-2, 74-75	234.15	264.18	8.12	67.6	8.34	0.22	0.68	0.010	19.54
26H-4, 74-75	237.17	267.20	8.84	73.7	9.03	0.19			
26H-6, 74-75	240.18	270.21	9.50	79.2					
27H-2, 74-75	243.65	274.70	7.80	65.0	8.01	0.21	0.60		
27H-4, 74-75	246.66	277.71	6.45	53.8	6.68	0.23	0.50	0.009	21.78
27H-6, 74-75	249.67	280.72	8.74	72.8					
28H-2, 74-75	253.14	285.59	7.27	60.6	7.77	0.50	1.27	0.028	15.43
28H-4, 74-75	256.14	288.59	9.49	79.1	9.56	0.07	0.33	0.005	10.94
28H-6, 74-75	259.14	291.59	9.98	83.2					
29H-2, 74-75	262.65	295.84	10.16	84.6	10.27	0.11	0.71		
29H-4, 74-75	265.66	298.85	10.06	83.8	10.25	0.19	1.17		
29H-6, 74-75	268.66	301.85	9.64	80.3					
30H-2, 74-75	272.14	306.48	9.08	75.6	9.18	0.10	0.41	0.005	16.11
30H-4, 74-75	275.16	309.50	9.68	80.7	9.83	0.15	0.78	0.006	23.16
30H-6, 74-75	278.18	312.52	9.53	79.4					
31H-2, 74-75	281.65	316.93	8.12	67.6	8.55	0.43	1.33	0.018	20.40
31H-4, 74-75	284.67	319.95	9.59	79.9	9.72	0.13	0.65		
31H-6, 74-75	287.69	322.97	8.85	73.7					
32H-1, 74-75	289.64	327.98	8.63	71.9					
32H-2, 74-75	291.14	329.48	8.00	66.7	8.14	0.14	0.42		
32H-3, 74-75	292.64	330.98	9.43	78.6					
32H-5, 74-75	295.64	333.98	7.20	60.0					
33H-2, 74-75	300.64	342.03	7.62	63.4	7.73	0.11	0.30	0.006	15.06
33H-4, 74-75	303.64	345.03	5.75	47.9	6.10	0.35	0.67	0.016	18.75
33H-6, 74-75	306.64	348.03	6.42	53.5					
34H-2, 74-75	310.14	352.77	3.04	25.3	4.48	1.44	1.93	0.150	8.23
34H-4, 74-75	313.14	355.77	6.25	52.1	6.66	0.41	0.86	0.021	16.62
34H-6, 74-75	316.14	358.77	3.22	26.8					
35X-2, 74-75	316.44	359.89	7.16	59.7					
35X-4, 74-75	319.44	362.89	4.95	41.3	6.22	1.27	2.16		
35X-6, 74-75	322.44	365.89	5.03	41.9					
36X-2, 74-75	325.44	370.06	4.57	38.1	4.89	0.32	0.52	0.018	14.99
36X-4, 74-75	328.44	373.06	4.98	41.5	5.26	0.28	0.48	0.013	18.21
36X-6, 74-75	331.44	376.06	4.54	37.8					
37X-2, 74-75	335.14	381.02	5.01	41.7	5.81	0.80	1.37	0.046	14.92
37X-4, 74-75	338.14	384.02	5.94	49.5	6.69	0.75	1.48	0.036	17.90
37X-6, 74-75	341.14	387.02	5.15	42.9					
38X-2, 74-75	344.74	391.86	4.24	35.3	5.35	1.11	1.71	0.124	7.68
39X-2, 74-75	354.24	402.60	4.85	40.4	5.60	0.75	1.26	0.049	13.28
39X-3, 74-75	355.74	404.10	4.83	40.2					
39X-4, 74-75	357.24	405.60	5.91	49.2					
39X-6, 74-75	360.24	408.60	2.91	24.3	3.33	0.42	0.55	0.017	20.65
40X-2, 74-75	363.94	413.56	3.64	30.3	4.16	0.52	0.74	0.035	12.62
40X-4, 74-75	366.94	416.56	6.59	54.9	7.06	0.47	1.04	0.025	15.99
40X-6, 74-75	369.94	419.56	5.22	43.5					
41X-2, 74-75	373.54	424.41	1.53	12.8	1.63	0.10			
41X-4, 74-75	376.54	427.41	3.84	32.0	4.18	0.34	0.50	0.015	19.60
42X-2, 74-75	383.24	435.37	2.45	20.4	3.87	1.42	1.79	0.041	29.45
42X-4, 74-75	386.24	438.37	2.66	22.2	3.69	1.03	1.32	0.099	8.88
42X-6, 74-75	389.24	441.37	3.29	27.4					
43X-1, 74-75	391.34	444.72	5.29	44.1	5.71	0.42	0.74		
43X-2, 74-75	392.82	446.20	5.10	42.5	5.37	0.27	0.46	0.078	2.92

Note: IC = inorganic carbon, TC = total carbon, TOC = total organic carbon, CFB = carbon-ate-free basis, TN = total nitrogen.

Table T16. Age-depth model, linear sedimentation rates, and mass accumulation rates, Site 1241.

Age (Ma)	Depth (mcd)	LSR (mcd/m.y.)	mcd growth factor	Corrected LSR (m/m.y.)	Dry density (g/cm ³)	CaCO ₃ average concentration (wt%)	TOC average concentration (wt%)	Total MAR (g/cm ² /k.y.)	CaCO ₃ MAR (g/cm ² /k.y.)	TOC MAR (g/cm ² /k.y.)	Noncarbonate MAR (g/cm ² /k.y.)
0.0	0.0										
1.0	20.7	21	1.13	18	0.63	63.6	0.33	1.2	0.7	0.004	0.4
2.0	49.7	29	1.13	26	0.73	67.2	0.27	1.9	1.3	0.005	0.6
3.0	76.0	26	1.13	23	0.80	72.2	0.21	1.9	1.3	0.004	0.5
4.0	106.1	30	1.13	27	0.85	79.9	0.17	2.3	1.8	0.004	0.5
5.0	143.5	37	1.13	33	0.94	85.5	0.05	3.1	2.7	0.002	0.5
6.0	186.0	43	1.13	38	0.95	85.3	0.09	3.6	3.1	0.003	0.5
7.0	254.2	68	1.13	60	0.92	80.9	0.12	5.5	4.5	0.007	1.1
8.0	289.2	35	1.13	31	0.86	69.9	0.15	2.7	1.9	0.004	0.8
9.0	322.9	34	1.13	30	1.03	79.4	0.12	3.1	2.4	0.004	0.6
10.0	374.0	51	1.13	45	0.77	52.6	0.27	3.5	1.8	0.009	1.6
11.0	417.5	43	1.13	38	0.68	40.6	0.44	2.6	1.1	0.011	1.5

Notes: LSR = linear sedimentation rate, MAR = mass accumulation rate. TOC = total organic carbon. This table is also available in [ASCII](#).